Mechanistic Studies of Atypical Reactions and Uncommon Substrates Native to Bacterial Cytochrome P450 Enzymes $OleT_{JE}$ and NikQ

by

Courtney Elizabeth Wise

Bachelor of Science
University of South Carolina, 2014

Submitted in Partial Fulfillment of the Requirements

For the Degree of Doctor of Philosophy in

Chemistry

College of Arts and Sciences

University of South Carolina

2019

Accepted by:

Thomas M. Makris, Major Professor

Caryn E. Outten, Committee Member

Aaron K. Vannucci, Committee Member

Alan W. Decho, Committee Member

Cheryl L. Addy, Vice Provost and Dean of the Graduate School

DEDICATION

This work is dedicated to my family. My completion of a doctoral degree would not have been possible without the perfect love and support of my mother, Patricia F. Wise, father, B. Jay Wise, brother, Matthew J. Wise, or significant other, Matthew R. Blahut.

I would also like to dedicate this achievement to the memory of my loved ones who are now only here in spirit. To my grandmothers, Ruby Twitty Faile (*Maw*) and Mary Panter Wise (*Grandma*), your resilience, moral character, and wisdom is a constant source of inspiration and strength. I aspire to live up to the example you set during your lives. To my maternal grandfather, Manley Boyce Faile, I genuinely wish I could have known you. Despite your untimely passing 22 years prior to my birth, your legacy of hardwork and honesty was impressed upon my mother during her childhood, attributes she worked to instill in my brother and I. To my paternal grandfather, James Bunyan Wise Jr. (*Pop*), I still remember your positivity and incredible wit 29 years after losing you. Your unselfish love for your grandchildren was apparent as you sought to entertain and amuse us even through your illness. I wish we could have had more time together. To my beloved Uncle Jim (James Bunyan Wise III), you always strived to help me see my own value and worth, even as a child. You were truly gone too soon, and I miss you so much.

Last but not least, to my precious Hank, my perfect companion of 14 years, you were my sunshine on the darkest of days and my sole source of joy at times. I truly could not have completed this degree without your unconditional love. I hope I can be the person you always thought that I was. I love you forever, my beautiful boy.

ACKNOWLEDGEMENTS

I would like to express my sincerest gratitude to my advisor, Dr. Thomas Makris. You took me under your wing as an undergraduate, encouraged me to pursue graduate studies, and have single-handedly guided my development into an independent scientist. In additional to scientific knowledge, you have also ensured that I have retained an appreciation for the greatest musical decade (which is well-established to be the 1990s), fostered my growth as an ice hockey fan, and greatly decreased the deficit in my geographical aptitude to a point where I may be able to correctly label 37 of the 50 U.S. states on a map. Thank you for taking a sincere interest in my academic and career goals, and for the time and effort you have put into helping me to achieve them. I could not have asked for a better mentor.

I would also like to thank my labmates from the past 5 years. Job(logan) Grant, José Amaya, and Steven Ratigan – you guys are like a second family. I feel so blessed to have been able to work with three of my best friends for so much of my Ph.D. Since you have each graduated and moved on to postdoctoral positions, your continued communication never fails to brighten my day and bring a smile to my face. I value each of you greatly, and I genuinely hope we will always remain close. Jason Hsieh – I am grateful for your friendship and support, as well as your contributions to the OleT project, which were invaluable. Suman Das, though we have not had as much time together, I am so thankful for your friendship and support over the past year. Your shining personality, positive attitude, tenacity, kindness, and fantastic sense of humor has been contagious and an

inspiration to your labmates. Olivia Manley – thank you so much for the sweet blanket with my perfect Hank on it – this gift still touches my heart and brings tears to my eyes. Thank you for helping me to remember my best friend in such a beautiful way. To all of my undergraduate researchers – Caleb Padgett, Himabindu Vinnakota, Gabriel D'Agostino, Nathan Poplin, and Alexis Holwerda – thank you for all of the time and work you contributed to our research. I have valued your friendship, as well as everything you have taught me by allowing me to be your mentor.

I am grateful to Dr. Caryn Outten, Dr. Aaron Vannucci, and Dr. Alan Decho for serving on my doctoral committee, and for the time, effort, and guidance invested in my development as a scientist. Your advice and discussion have been invaluable to me. Also, I would like to thank Dr. John Dawson for all of his insight and encouragement during the Makris lab group meetings.

I cannot find words adequate to express my gratitude to my family. Momma, Daddy, and Bubby – I could not have completed this without your love and support. I am so incredibly blessed to have y'all as my parents and brother and love you more than I could ever convey. I am also thankful for the love and support of my better half, Matt Blahut, who has put up with so, so much throughout this process, seen me at my absolute worst, and somehow still chooses to journey through life with me. Thank you for holding my hand through all of the ups and downs, Honeybear, I love you very much and am looking forward to our next adventure together. I want to acknowledge the joy my precious feline babies have brought to my life. My precious Hanker-Pan loved me through the first four years of graduate school, but sadly was unable to see the final product. I love you and miss you, my beautiful boy, thank you for being the best part of my day every day for 14

years. Our current kittens, Adama and Oliver, have dutifully taken over this role in our lives and are a constant source of happiness – I love you, my fluffy little buffalos

Thank you to Charity Brooks, Swanandi Pote, Julia Bian, Megan Mitchell, Amanda Wagner, Christian Brown, and anyone who I may have inadvertently omitted for your friendship and fellowship over the past five years. Thank you for being there when I needed to cry, vent, and celebrate, and when I just needed a good cup of coffee. I sincerely hope we will stay in touch and remain close friends as I venture across the country for the next stage of my career.

ABSTRACT

Cytochrome P450 (CYP) enzymes typically perform hydroxylation chemistry on small molecule substrates using atmospheric oxygen and electrons from redox partner proteins. This reactivity is dependent on a thiolate-ligated heme cofactor that also allows for spectroscopic detection of ligation, oxidation, and environmental changes to the iron metal. The onset of the genomics era has resulted in the discovery of CYPs that deviate from this paradigm in terms of reaction performed, cosubstrate requirements, and substrate-scope. This work focuses on two of these unusual P450s – OleT and NikQ. OleT performs an unconventional H_2O_2-dependent decarboxylation reaction on a standard small molecule fatty acid substrate to yield 1-olefins and CO_2. A desire to maximize the biosynthetic potential of this enzyme while addressing limitations imposed by the peroxide requirement has resulted in numerous reports that OleT may have the capacity to utilize biological redox donors and O_2 in a canonical P450 reaction mechanism. Chapter 2 centers on transient kinetics, cryoradiolysis, and turnover studies used to investigate the precise origins of OleT alkene production using surrogate redox systems and dioxygen. While results show that this enzyme is ultimately incapable of performing true O_2-driven catalysis, conclusions do illuminate several strategies for improving OleT for downstream biocatalytic applications. Chapters 3 and 4 focus on NikQ, which carries out classical P450 β-hydroxylation chemistry using O_2 and reducing equivalents from redox donors on a L-histidine substrate requisitely appended to NikP1, a ~75 kDa nonribosomal peptide synthetase protein. The first half of the CYP catalytic cycle is typically regulated at multiple steps by the binding

of substrate; however, this mechanistic gating in P450s acting on protein-tethered substrates is not well-elucidated. We use various spectroscopic techniques, transient kinetics, and spectroelectrochemical studies to investigate the influence of this complex substrate on early NikQ catalysis. Results indicate that NikP1-binding does not substantially regulate NikQ, which is highly atypical of P450s. Possible molecular determinants and functional significance of this mechanistic peculiarity will also be discussed.

TABLE OF CONTENTS

LIST OF TABLES

LIST OF FIGURES

CHAPTER 1

Atypical Reactions and Unusual Substrates of Cytochrome P450 Enzymes in Bacterial Biosynthetic Pathways

1.1 INTRODUCTION TO CYTOCHROME P450

The cytochrome P450 (CYP) enzyme superfamily is one of the largest and most diverse, carrying out critical metabolic reactions in organisms from all domains of life.[1, 2] As of 2017, an excess of 300,000 P450s have been sequenced, with that number expected to rise to at least 1,000,000 by 2020 due to global sequencing initiatives.[1] Of these, ~62,000 are from bacteria, with >3,000 having been assigned CYP nomenclature and divided into 602 prokaryotic CYP families.[1] The ubiquitous nature of these enzymes in bacterial species warrants in-depth study and characterization due to crucial involvement in natural product biosynthetic pathways, which could be exploited for a myriad of industrial and pharmaceutical applications.

All cytochrome P450s possess a heme-iron cofactor with a proximal, cysteine-derived thiolate ligand, as shown in Figure 1.1 A. This imparts a red chromophore to the protein that allows for convenient spectroscopic monitoring of changes in ligation and oxidation state during catalysis.[3-5] This spectroscopic sensitivity, with relatively large extinction coefficients for the wavelength of maximal absorbance (termed the *Soret* band),

is particularly useful for detailed mechanistic investigations.[6] The cofactor cycles between pentacoordinate and hexacoordinate ligation geometries through ligand-switching at the distal position, with the iron bound to a water molecule at this sixth site in the ferric resting state.[7] The phenomenon for which the name "P450" was bestowed derives from a specific instance of oxidation and ligation state alterations - upon reduction to the ferrous oxidation state and immediate ligation of supplemented gaseous carbon monoxide, a pigment with absorbance maximum at 450 nm is detected, as shown in Figure 1.1 B.[8] Though not part of the P450 catalytic cycle, the formation of this CO-adduct and confirmation of absorbance at ~450 nm can be used to confirm the integrity of the proximal thiolate ligand that sets cytochrome P450s apart from other histidine or methionine-ligated hemoproteins like myoglobin, hemoglobin, and cytochrome c.[6]

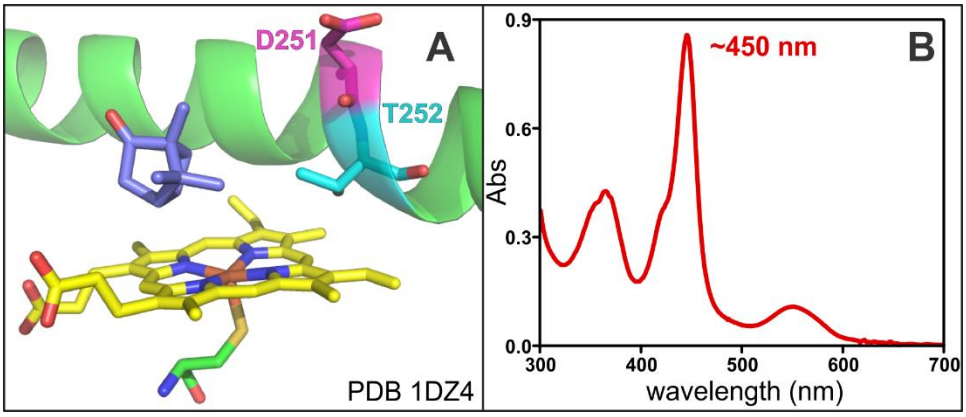

Figure 1.1. Cytochrome P450 enzymes possess a thiolate-ligated heme cofactor (A) which imparts to the protein a unique absorbance spectrum (B) when reduced in the presence of carbon monoxide with maxima at 450 nm, from which the enzyme superfamily derives its name. A also shows the camphor substrate in the CYP101 (PDB 1DZ4) active site,[9] along with two residues distal to the heme, D251 and T252, that have been shown to be critical for catalysis in O_2-dependent P450s. The wavelength of maximal absorbance in CYPs is termed the *Soret* peak, at ~450 nm in **B**, and is sensitive to changes in oxidation and ligation state, allowing for sensitive spectroscopic analysis of P450 catalytic intermediates.

Classically, CYP enzymes are thought of as monooxygenases, performing hydroxylation chemistry on small molecule substrates, as shown in the scheme of Figure 1.2.[2] This reactivity results from a catalytic cycle dependent upon binding of atmospheric oxygen, two proton transfers, and two reduction events from an electron source, typically a distinct iron-sulfur containing protein.[2] The most well-characterized of these is $P450_{Cam}$ (also referred to as "CYP101"), a camphor hydroxylase from *Pseudomonas putida* that first appears in the literature in 1968.[10-15] CYP101 is still under active investigation today, and is often thought of as a model for bacteria P450 reactivity. As such, this system in particular, will often be used as a point of reference throughout this chapter.

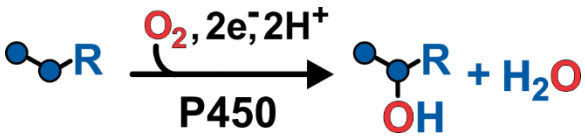

Figure 1.2. The overall hydroxylation reaction catalyzed by cytochrome P450 enzymes. CYP monoxygenation of unactivated C-H bonds is usually dependent on the transfer of two electrons from physiological redox partner proteins, binding of atmospheric oxygen, and two sequential protonation events.

CYP hydroxylation chemistry is initiated by the substrate-binding, which displaces a distal water ligand from the iron, decreasing the energy gap between the non-degenerate d-orbitals of the iron and promoting two previously paired electrons from the lower energy orbitals to the higher ones as the ligand geometry changes from hexacoordinate (species 1, in black, of Figure 1.3 below) to pentacoordinate (2, green, in Figure 1.3).[2] This shift from low-spin (S = 1/2) to high-spin (S = 5/2) is characterized by a change in Soret absorbance from the resting state at ~418 nm to ~395 nm. As this optical change is dependent upon

substrate concentration, it can be used for calculation of a binding constant for the substrate. Additionally, the spin shift is accompanied by a positive change in heme reduction potential, allowing for single electron transfer from a redox partner protein, 2Fe-2S-containing putidaredoxin (Pd) in the case of $P450_{Cam}$.[2, 13]

The alteration in enzyme reduction potential serves as a thermodynamic gate, with the protein that acts as the electron donor to the cytochrome typically possessing a potential poised between that of the substrate-free and substrate-bound P450, ensuring that only reduction of the substrate-bound enzyme is thermodynamically favorable.[13, 14] This prevents uncoupling through consumption of NAD(P)H by an enzyme that lacks substrate, and thus protects against generation of the reactive oxygen species (ROS) that result from unproductive consumption of the pyridine nucleotide. This redox partner acts as the electron donor for two distinct, non-consecutive one-electron reduction steps while also fulfilling secondary functions in effector roles, which are important for efficient catalysis through specific electrostatic interaction with the P450 surface proximal to the heme.[11] The first electron transfer yields the ferrous cytochrome, shown as intermediate 3, in blue, of Figure 1.3.

Dioxygen binding to the ferrous iron follows the first electron transfer,[2, 10] yielding an oxy-complex (4, violet, in Figure 1.3) which is then reduced by a second electron in the rate-limiting step of P450 catalysis to form a ferric-peroxo intermediate (species 5, red, in Figure 1.3).[16] Instability of the oxy-complex can lead to uncoupling through the release of superoxide and autoxidation of the substrate-bound enzyme back to the ferric high-spin state. This unproductive and energetically expensive ROS-generating pathway is minimized by stabilization of the oxy-complex in the presence of substrate due to both

steric and electronic effects from the substrate, as well as conformational changes that are induced by interactions with the redox partner proteins.[2, 11, 17] The next two catalytic steps rely on a critical pair of amino acids – termed the *acid-alcohol pair* and shown in Figure 1.1 A as Aspartate-251 and Threonine-252 for CYP101 - situated distal to the heme cofactor on the long I-helix that spans the length of the P450.[18-26] Mutation of the *acid*, which may be a glutamate or an aspartate, results in overall impairment of turnover through the perturbation of multiple catalytic steps. Second electron transfer is significantly hindered by several orders of magnitude in studies of the D251N mutant of CYP101.[18, 19, 23] Alteration of this acidic residue seemingly results in a separation of the proton-coupled electron-transfer steps normally linking the second reduction and and first protonation events of the cycle.[19] Correspondingly, the typically elusive ferric-peroxoanion intermediate is stabilized at low temperatures following reduction of the dioxygen adduct by ɣ-irradiation in CYP101-D251N, and can be detected using electron paramagnetic resonance (EPR) spectroscopy at liquid nitrogen temperatures. In contrast, only the ensuing hydroperoxo-intermediate is observable at 77 K in the wild-type (WT) enzyme.[19] This demonstrates a dependence upon this amino acid for efficient protonation of the ferric-peroxo species to yield the ferric-hydroperoxo intermediate (species 6, orange, in Figure 1.3), as well as an influence upon the catalytic steps immediate preceeding and following the first proton transfer.[19, 23] Mutation of the alcohol residue has been shown to result in severe uncoupling to H_2O_2, with no detectable turnover in some instances.[19-22, 25] Further, the T252A mutant of CYP101 showed enhanced stability of the ferric-hydroperoxo species via EPR and thermal annealing experiments, implying that uncoupling occurs from this state as the second protonation event is acutely impeded.[19]

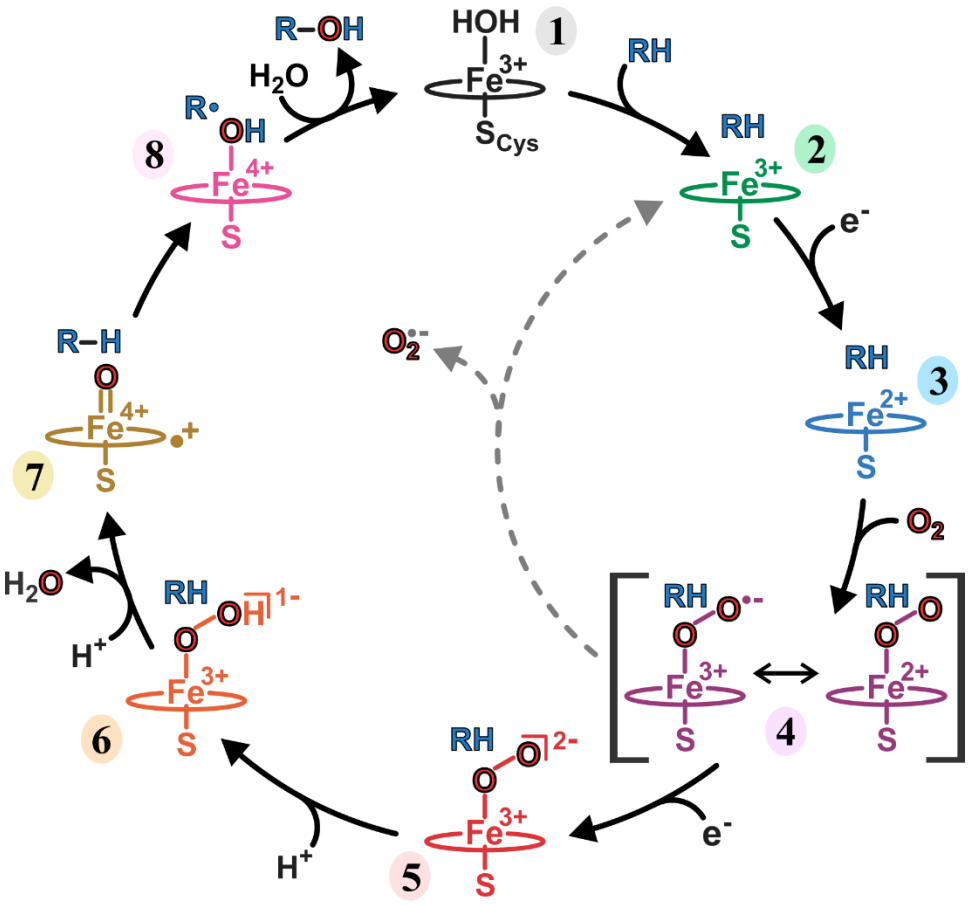

Figure 1.3. The P450 catalytic cycle. The aquo ligand is displaced from the low-spin ferric enzyme (**1**, in black) upon substrate-binding to yield the pentacoordinate high-spin state (**2**, in green). A corresponding increase in heme reduction potential allows for the first electron transfer to give the ferrous P450 (**3**, in blue), which subsequently ligates atmospheric oxygen to form the oxy-complex (**4**, in violet). The rate-limiting second reduction step to yield the ferric-peroxo intermediate (**5**, in red) competes kinetically with the autoxidation shunt (grey dotted pathway), an uncoupling of the ferric-superoxide intermediate back to the high-spin form via superoxide release. The initial proton transfer to the peroxo-P450 results in the hydroperoxo-ferric state (**6**, in orange), followed by a second protonation that instigates O-O bond heterolysis for release of H_2O and formation of reactive intermediate compound-I (**7**, in gold) – a Fe(IV)-oxo species with delocalized π-cation radical. Hydrogen atom abstraction from the substrate gives compound-II (**8**, in fuchsia), an Fe(IV)-hydroxo state, then OH-rebound yields the hydroxylated product and water re-binds at the distal position to re-form the low-spin ferric resting state.

The transfer of a second proton to the ferric-hydroperoxo intermediate initiates heterolysis of the end-on Fe-ligated O-O bond while releasing a water molecule to form compound-I, a reactive Fe(IV)-oxo intermediate with a delocalized π-cation radical (7, gold, in Figure 1.3).[27] Compound-I abstracts a hydrogen atom from the substrate to yield compound II, a Fe(IV)-hydroxo species (8, fuchsia, in Figure 1.3), which performs oxygen-rebound chemistry resulting in the hydroxylated product and a return to the ferric-aquo resting state upon the re-ligation of water to the heme-iron.[28]

1.2 OleT$_{JE}$: Unconventional Decarboxylation Chemistry using an Atypical Co-Substrate

Cytochrome P450 peroxygenases comprise a sub-group of the CYP superfamily that is capable of utilizing a H_2O_2 co-substrate through the aptly termed "peroxide shunt", in which peroxide binding to the high-spin protein yields compound-I, without the need for electron transfer from redox partners, O_2-binding, or proton transfer steps.[29] Members of the CYP152 family utilize peroxide in this manner for the chemical transformation of C_n fatty acids to C_n α- or β-hydroxy fatty acids or C_{n-1}-length terminal olefins and carbon dioxide.[30] These enzymes share similar structural characteristics that not only enable efficient utilization of a peroxide oxidant, but may also disfavor the forementioned O_2-dependent mechanism of product formation.[31, 32] Specifically, these P450s lack the acid-alcohol residues, instead possessing conserved distal arginine and proline amino acids on the I-helix. In CYP152 enzymes, this arginine establishes electrostatic contacts critical for substrate-positioning with the fatty acid during substrate-binding.[30, 33-35] Around position 85, CYP152 P450s also feature either a glutamine or a histidine residue that has been

hypothesized, by analogy to heme-dependent peroxidase enzymes, to play a role in peroxide activation.[36-39]

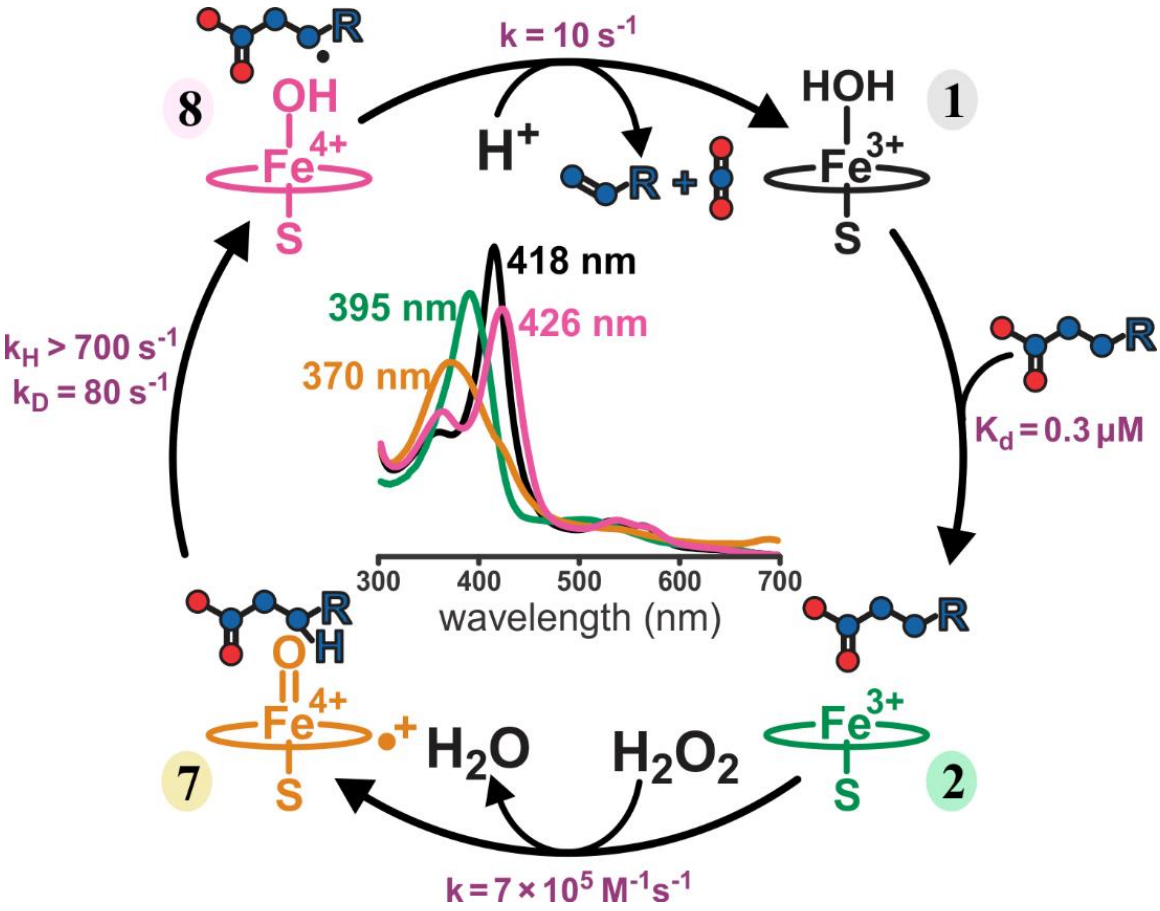

Figure 1.4. Peroxide-dependent decarboxylation of long-chain fatty acids to terminal alkenes and CO_2 by OleT$_{JE}$. *Please note that the numbering of intermediates from Figure 1.3 was retained for consistency, despite the lack of species 3 through 6 in the above mechanism.* Low-spin OleT (**1**, in black), with Soret at 418 nm, goes appreciably high-spin (species **2**, in green, with Soret at 395 nm) upon binding of eicosanoic acid, for which this P450 has a high affinity with a dissociation constant of ~300 nM.[40] H_2O_2-binding to the substrate-bound enzyme occurs rapidly to yield compound-I (**7**, in gold) with Soret maximum at ~370 nm and a second order rate constant with respect to peroxide of 7×10^5 $M^{-1}s^{-1}$.[41] The isotopically sensitive decay of compound-I gives rise to compound-II (species **8**, in fuchsia, with Soret at 426 nm) as a hydrogen atom is abstracted from the substrate leaving a substrate-centered radical.[41] Proton-coupled electron-transfer results in the production of 1-nonadecene and carbon dioxide and re-binding of a water molecule restores the ferric low-spin resting state.[40, 41]

One notable member of the CYP152 family, $OleT_{JE}$, was isolated from *Jeotgalicoccus sp.* found in Jeotgal Korean fish sauce and reported to catalyze the decarboxylation of long-chain fatty acids into carbon dioxide and terminal alkenes.[42] This reactivity inspired a flurry of research, with the hopes of utilizing this enzyme for the industrial scale production of biofuels.[31, 33, 43] Despite acting on a canonical small molecule substrate, the unusual decarboxylase activity and use of H_2O_2 co-substrate have presented an intriguing opportunity for mechanistic inquiry not previously described in cytochrome P450s. Through transient kinetic studies, our laboratory has mapped much of the reaction coordinate of OleT with peroxide, as summarized in Figure 1.4.[40, 41]

The goal of exploiting the reactivity of OleT as an alternative fuel source has led to investigations into the viability of biofuel production *in vivo* by this enzyme. However, the peroxide requirement presents significant complications within an organism due to the deleterious effects of ROS, as well as the efficient disproportionation of H_2O_2 by other intracellular enzymes like catalase. As a solution, recent work has sought to achieve $OleT_{JE}$ turnover using O_2 and reducing equivalents from redox partner proteins.[44-46] This method has demonstrated some success *in vitro*, which has been attributed to an ability of this enzyme to utilize the canonical O_2-driven P450 reactivity.[44-46] In light of the previously discussed distal architecture of OleT, particularly the lack of acid-alcohol pair, this raises multiple puzzling mechanistic questions.[30, 47] Additionally, as $OleT_{JE}$ lacks the redox partner binding site for several of the redox donor proteins (including Pd) reported to result in high alkene titers with this P450, efficient reduction of the cytochrome seems unlikely.[44-46] Chapter 2 of this thesis is focused on the investigation into the mechanistic origin of $OleT_{JE}$ reactivity with O_2 and electrons using rapid-mix kinetics experiments, single and

multiple turnover studies, and cryoradiolysis electron paramagnetic resonance methodologies.[48] Our findings indicate that multiple reaction pathways are occurring simultaneously, with H_2O_2-production being the commonality between the different routes to product formation.[48]

1.3 NikQ: Hydroxylation of a Protein-Tethered substrate

Nonribosomal peptide synthetases (NRPSs) are protein scaffolds that act as natural product assembly lines in many bacterial biosynthetic pathways.[49] Resulting amino acid (AA) polymers have amide bond linkages in common with ribosomally-produced counterparts, but also generally feature functional groups and bonding motifs not observed in peptides resulting from translational machinery.[49] These unique chemical moieties, typically installed on the maturing peptide by dedicated tailoring enzymes, often impart medically-relevant activities to the nonribosomal peptide (NRP) product, allowing for applications as anticancer therapeutics, immunosuppressants, and antimicrobial agents, examples of which are shown in Figure 1.5.[50-57] Tailoring enzymes have been reported to perform halogenation, hydroxylation, and oxidative crosslinking chemistries, among others.[53, 58-62] Of particular interest are tailoring enzymes that requisitely function on NRPS-tethered substrates, achieving the highly sought-after synthetic goal of mid-stage functionalization *in vivo*.[53, 58, 59] An in-depth understanding of the mechanisms underlying interactions between tailoring enzymes and cognate NRPS substrates could allow for the generation of libraries of novel potential pharmaceuticals, adding to the antimicrobial arsenal so rapidly dwindling due to increasing resistance in microorganisms. Despite this tremendous potential for natural product diversification and targeted synthesis, the

interplay between tailoring enzymes and NRPS proteins remains poorly elucidated, largely owing to numerous complexities inherent to the NRPS substrate.[50, 59]

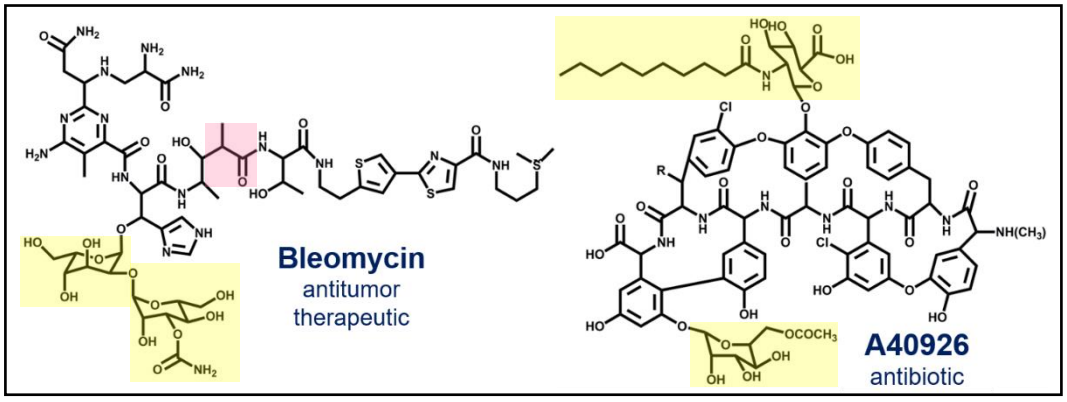

Figure 1.5. Examples of clinically significant nonribosomal peptides. Bleomycin is an antitumor therapeutic isolated from a polyketide synthase (PKS)-NRPS hybrid pathway out of *Streptomyces verticillus*.[54] Glycopeptide antibiotic A40926 is produced from a NRPS system out of *Nonomuraea sp*.[55] Light red boxes correspond to elements deriving from PKS-modules and yellow boxes represent sugar additions to the peptide along with non-NRPS modifications to the sugar; remaining unlabeled structures are incorporated using NRPS machinery.

An NRPS may consist of a single ~10 kDa thiolation (T-) domain, but are more frequently organized into larger modules comprised of catalytic domains alongside one or more T-domains, including adenylation (A-) domains, condensation (C-) domains, and thioesterase (TE-) domains, among others.[49, 50, 58, 59] Each T-domain can exist in an *apo*, unmodified form, or in up to three different possible post-translationally modified states.[49, 50] The *holo* T-domain features a phosphopantetheine (ppant) cofactor appended to a conserved serine residue.[63] In the *amino-acyl* (or *loaded*) form, the AA that will ultimately be incorporated into peptide chain is enzymatically attached to the end of the ppant arm of the holo T-domain by an upstream or freestanding A-domain.[49, 50, 63] Apo, holo, and loaded T-domains are shown in Figure 1.6 for clarity. Though not extensively discussed in the studies undertaken within this work, loaded T-domains that serve as substrates for tailoring

enzymes can formally exist in a product-bound, *tailored* state as well. Following loading or tailoring, C-domains instigate peptide bond formation between the cargo tethered to upstream and downstream T-domains, with TE-domains often carrying out chain termination for an NRPS module.[49, 50, 63] Multi-domain NRPS modules can extend into the megadalton range, presenting significant challenges in obtaining high yields of stable, soluble protein.[49, 50, 58, 64] Further, the presence of multiple T-domains within a given module complicates recognition studies of tailoring enzymes with NRPS substrates.[50] This is especially problematic in instances where a single tailoring enzyme acts on multiple T-domains within a module,[65] or where multiple T-domains within the NRPS target the same AA.[66] As an answer to these obstacles, a single T-domain is often excised from the native module, though this sometimes requires the use of specialized expression tags or refolding to obtain soluble protein, and excludes the possibility that adjacent domain surface sites may have a role in NRPS-tailoring enzyme interactions.[50, 59]

A high degree of catalytic specificity has been demonstrated to vary among tailoring enzymes acting on NRPS substrates, with regio- and stereospecific product formation, as well as turnover efficiency, often being dependent upon the identity of the aminoacyl-NRPS.[53, 66-69] The catalytic triggering of aliphatic halogenase SyrB2 has been shown to be significantly diminished when the target NRPS, SyrB1, is loaded with the incorrect amino acid, or when the correct amino acid is appended to a similar but non-native NRPS.[66] While some tailoring enzymes will only interact with a single AA-NRPS pairing, others have demonstrated the ability to catalyze reactions on different T-domain and amino acid combinations. One example of the latter is $P450_{Sky}$, a β-hydroxylase in the skyllamycin biosynthetic pathway, which natively hydroxylates three different T-domains

that each specifically tether three distinct AAs - phenylalanine, tyrosine, and leucine.[65, 70] Interestingly, $P450_{Sky}$ fails to hydroxylate another leucine-tethered T-domain within this pathway, implicating what is likely a substrate recognition mechanism dependent upon interactions of the tailoring enzyme with the T-domain surface.[65] Whether or not the surface sequence of adjacent domains have a role in this process is yet to be elucidated for this system. By contrast, halogenase tailoring enzyme CytC3 displays a strong preference for one NRPS, but can metabolize several different tethered amino acids.[71] Taken together, this information paints a complex and poorly understood image of the molecular determinants underlying tailoring enzyme-NRPS recognition.

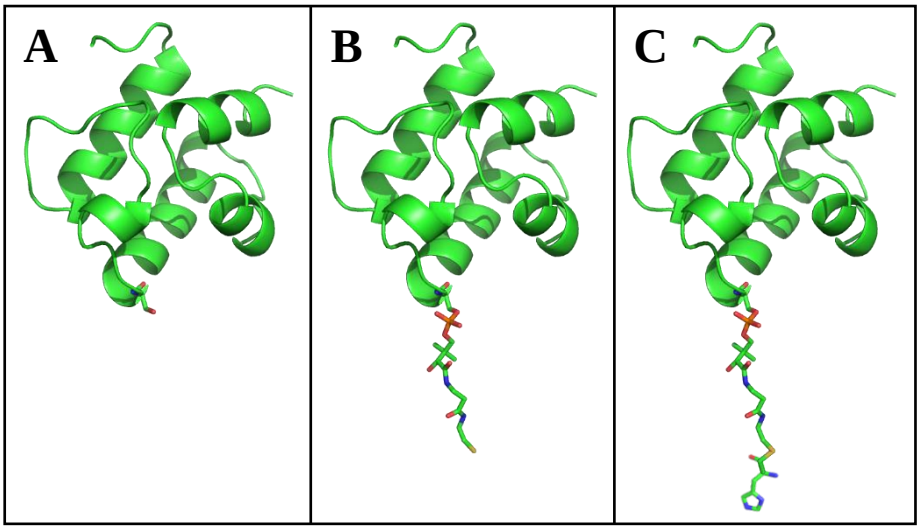

Figure 1.6. T-domain post-translational modification states. The *apo*-NRPS (A) is unmodified. In B, the *holo*-NRPS has a phosphopantetheine (ppant) group appended to a conserved serine on the T-domain. An *amino-acyl* NRPS is presented in C, with target amino acid bound via thioester linkage to the end of the ppant arm. (T-domain is from the $P450_{Sky}$•PCP7 crystallized co-complex;[67] PDB 4PWV)

Within the nikkomycin biosynthetic pathway of *Streptomyces tendae* Tü901, didomain NRPS NikP1 and hydroxylase NikQ[72] present an attractive potential model

system for gaining empirical insight into the molecular determinants underlying the recognition of NRPS-tethered substrates by tailoring enzymes. In this system, the NikP1 A-domain activates an L-histidine residue, covalently linking it to the ppant cofactor of the adjacent C-terminal T-domain, yielding L-His-NikP1.[72] As shown in Figure 1.7, cytochrome P450 NikQ β-hydroxylates the NikP1-bound AA to give the tailored product, β-OH-His-NikP1.[72] The β-hydroxyhistidine is released from the NRPS by freestanding TE-domain NikP2, and processed further to an imidazolone moiety that is ultimately incorporated into nikkomycin X, a clinically employed NRP antifungal.[72]

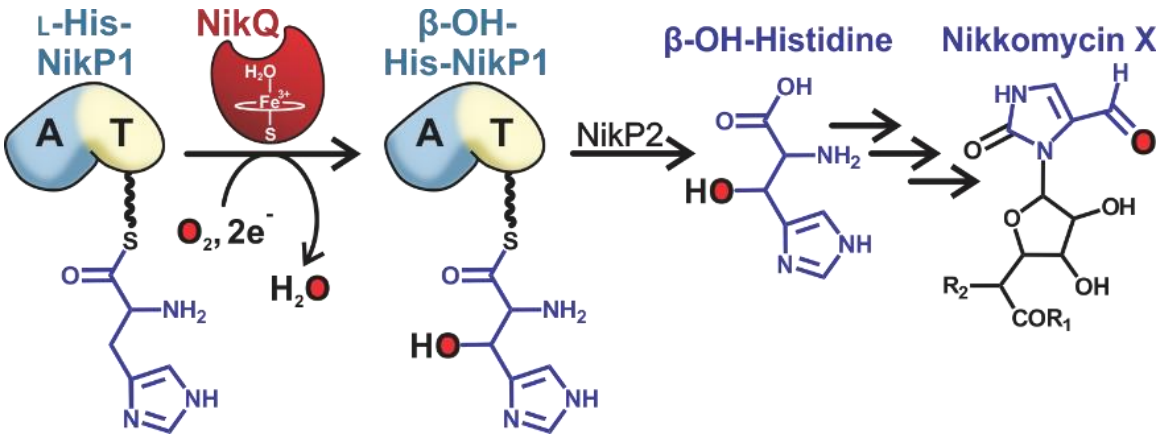

Figure 1.7. NikQ β-hydroxylates L-his-NikP1 in the biosynthesis of nikkomycin X antibiotics. Cytochrome P450 NikQ performs a β-hydroxylation reaction on an L-histidine residue that is requisitely tethered to 75 kDa NRPS didomain NikP1. The β-hydroxyhistidine is further processed to an imidazolone after NikQ tailoring and release from NikP1 by NikP2, and is then incorporated into nikkomycin X antibiotics in *Streptomyces tendae*.

NikQ and NikP1 proteins are both soluble, stable, and express in high yeilds yields.[72] For NikP1, this is likely due in part to the presence of an N-terminal MbtH-like region on the NikP1 A-domain, which is thought to promote proper folding and solubility of NRPS modules. The relatively simple NikP1 A-T-didomain is the fully intact NRPS module instead of a truncated form of the protein,[72] circumventing issues that arise when

part of the NRPS is excised and isolated from the full scaffold.[50] Further, the heme-iron cofactor of NikQ also allows for detailed analyses of ligand and oxidation changes via various spectroscopies that may be more difficult or not possible at all in non-heme tailoring enzymes.[6] Decades of literature describing CYP spectroscopy and the impact of small molecule substrates on P450 catalysis provide a scaffold for experimental design and data interpretation of NikQ with its protein-tethered substrate. P450 NikQ therefore enables a more thorough investigation of the impact of substrate upon tailoring enzyme catalysis than would be available in many other NRP-producing systems, especially when coupled to the comparatively uncomplicated nature of NikP1 versus other NRPS proteins.

Our work presented in chapter 3 of this thesis demonstrates stable complex formation between NikQ and L-His-NikP1 with a K_D of 22 μM, along with detailed mechanistic studies demonstrating an atypical mode of catalytic regulation in this P450 by the NRPS substrate.[73] To date, this is the only binding quantification of an NRPS-modifying tailoring enzyme with native intact substrate, as well as the first analysis into the impact of an NRPS substrate on the early steps of P450 tailoring enzyme catalysis beyond substrate binding.[73] The fourth chapter will examine the catalytic consequences of mutating two atypically bulky isoleucine residues to glycines at sites proximal to the NikQ heme-iron. Data presented in both chapters will illuminate the molecular determinants of NRPS interactions with P450 tailoring enzymes, and seek to better understand how proximal site sterics impact P450s reactivity and inhibition.

1.4 REFERENCES

1. Nelson, D. R., Cytochrome P450 diversity in the tree of life. *Biochim Biophys Acta Proteins Proteom* **2018,** *1866* (1), 141-154.
2. Denisov, I. G.; Makris, T. M.; Sligar, S. G.; Schlichting, I., Structure and chemistry of cytochrome P450. *Chem Rev* **2005,** *105* (6), 2253-2277.
3. Dawson, J. H.; Holm, R. H.; Trudell, J. R.; Barth, G.; Linder, R. E.; Bunnenberg, E.; Djerassi, C.; Tang, S. C., Letter: Oxidized cytochrome P-450. Magnetic circular dichroism evidence for thiolate ligation in the substrate-bound form. Implications for the catalytic mechanism. *J Am Chem Soc* **1976,** *98* (12), 3707-3708.
4. Sono, M.; Andersson, L. A.; Dawson, J. H., Sulfur donor ligand binding to ferric cytochrome P-450-CAM and myoglobin. Ultraviolet-visible absorption, magnetic circular dichroism, and electron paramagnetic resonance spectroscopic investigation of the complexes. *J Biol Chem* **1982,** *257* (14), 8308-8320.
5. Hahn, J. E.; Hodgson, K. O.; Andersson, L. A.; Dawson, J. H., Endogenous cysteine ligation in ferric and ferrous cytochrome P-450. Direct evidence from x-ray absorption spectroscopy. *J Biol Chem* **1982,** *257* (18), 10934-10941.
6. Luthra, A.; Denisov, I. G.; Sligar, S. G., Spectroscopic features of cytochrome P450 reaction intermediates. *Arch Biochem Biophys* **2011,** *507* (1), 26-35.
7. Dawson, J. H.; Andersson, L. A.; Sono, M., Spectroscopic investigations of ferric cytochrome P-450-CAM ligand complexes. Identification of the ligand trans to cysteinate in the native enzyme. *J Biol Chem* **1982,** *257* (7), 3606-3617.
8. Omura, T.; Sato, R., The Carbon Monoxide-Binding Pigment of Liver Microsomes. I. Evidence for Its Hemoprotein Nature. *J Biol Chem* **1964,** *239*, 2370-2378.

9. Schlichting, I.; Berendzen, J.; Chu, K.; Stock, A. M.; Maves, S. A.; Benson, D. E.; Sweet, R. M.; Ringe, D.; Petsko, G. A.; Sligar, S. G., The catalytic pathway of cytochrome p450cam at atomic resolution. *Science* **2000,** *287* (5458), 1615-1622.
10. Lipscomb, J. D.; Sligar, S. G.; Namtvedt, M. J.; Gunsalus, I. C., Autooxidation and Hydroxylation Reactions of Oxygenated Cytochrome P-450cam. *J Biol Chem* **1976,** *251* (4), 1116-1124.
11. Kuznetsov, V. Y.; Poulos, T. L.; Sevrioukova, I. F., Putidaredoxin-to-cytochrome P450cam electron transfer: differences between the two reductive steps required for catalysis. *Biochemistry* **2006,** *45* (39), 11934-11944.
12. Eisenstein, L.; Debey, P.; Douzou, P., P450cam: oxygenated complexes stabilized at low temperature. *Biochem Biophys Res Commun* **1977,** *77* (4), 1377-1383.
13. Sligar, S. G.; Gunsalus, I. C., A thermodynamic model of regulation: modulation of redox equilibria in camphor monoxygenase. *Proc Natl Acad Sci USA* **1976,** *73* (4), 1078-1082.
14. Gunsalus, I. C.; Sligar, S. G., Redox regulation of cytochrome P450cam mixed function oxidation by putidaredoxin and camphor ligation. *Biochimie* **1976,** *58* (1-2), 143-147.
15. Katagiri, M.; Ganguli, B. N.; Gunsalus, I. C., A soluble cytochrome P-450 functional in methylene hydroxylation. *J Biol Chem* **1968,** *243* (12), 3543-3546.
16. Imai, Y.; Sato, R.; Iyanagi, T., Rate-limiting step in the reconstituted microsomal drug hydroxylase system. *J Biochem* **1977,** *82* (5), 1237-1246.
17. Denisov, I. G.; Grinkova, Y. V.; Baas, B. J.; Sligar, S. G., The ferrous-dioxygen intermediate in human cytochrome P450 3A4 - Substrate dependence of formation and decay kinetics. *J Biol Chem* **2006,** *281* (33), 23313-23318.

18. Denisov, I. G.; Makris, T. M.; Sligar, S. G., Cryotrapped reaction intermediates of cytochrome p450 studied by radiolytic reduction with phosphorus-32. *J Biol Chem* **2001,** *276* (15), 11648-11652.
19. Davydov, R.; Makris, T. M.; Kofman, V.; Werst, D. E.; Sligar, S. G.; Hoffman, B. M., Hydroxylation of camphor by reduced oxy-cytochrome P450cam: mechanistic implications of EPR and ENDOR studies of catalytic intermediates in native and mutant enzymes. *J Am Chem Soc* **2001,** *123* (7), 1403-1415.
20. Okamoto, N.; Imai, Y.; Shoun, H.; Shiro, Y., Site-directed mutagenesis of the conserved threonine (Thr243) of the distal helix of fungal cytochrome P450nor. *Biochemistry* **1998,** *37* (25), 8839-8847.
21. Yeom, H.; Sligar, S. G.; Li, H.; Poulos, T. L.; Fulco, A. J., The role of Thr268 in oxygen activation of cytochrome P450BM-3. *Biochemistry* **1995,** *34* (45), 14733-14740.
22. Imai, M.; Shimada, H.; Watanabe, Y.; Matsushima-Hibiya, Y.; Makino, R.; Koga, H.; Horiuchi, T.; Ishimura, Y., Uncoupling of the cytochrome P-450cam monooxygenase reaction by a single mutation, threonine-252 to alanine or valine: possible role of the hydroxy amino acid in oxygen activation. *Proc Natl Acad Sci USA* **1989,** *86* (20), 7823-7827.
23. Sjodin, T.; Christian, J. F.; Macdonald, I. D.; Davydov, R.; Unno, M.; Sligar, S. G.; Hoffman, B. M.; Champion, P. M., Resonance Raman and EPR investigations of the D251N oxycytochrome P450cam/putidaredoxin complex. *Biochemistry* **2001,** *40* (23), 6852-6859.

24. Makris, T. M.; Davydov, R.; Denisov, I. G.; Hoffman, B. M.; Sligar, S. G., Mechanistic enzymology of oxygen activation by the cytochromes P450. *Drug Metab Rev* **2002,** *34* (4), 691-708.

25. Raag, R.; Martinis, S. A.; Sligar, S. G.; Poulos, T. L., Crystal structure of the cytochrome P-450CAM active site mutant Thr252Ala. *Biochemistry* **1991,** *30* (48), 11420-11429.

26. Gerber, N. C.; Sligar, S. G., A role for Asp-251 in cytochrome P-450cam oxygen activation. *J Biol Chem* **1994,** *269* (6), 4260-4266.

27. Rittle, J.; Green, M. T., Cytochrome P450 compound I: capture, characterization, and C-H bond activation kinetics. *Science* **2010,** *330* (6006), 933-937.

28. Newcomb, M.; Halgrimson, J. A.; Horner, J. H.; Wasinger, E. C.; Chen, L. X.; Sligar, S. G., X-ray absorption spectroscopic characterization of a cytochrome P450 compound II derivative. *Proc Natl Acad Sci USA* **2008,** *105* (24), 8179-8184.

29. Shoji, O.; Watanabe, Y., Peroxygenase reactions catalyzed by cytochromes P450. *J Biol Inorg Chem* **2014,** *19* (4-5), 529-539.

30. Munro, A. W.; McLean, K. J.; Grant, J. L.; Makris, T. M., Structure and function of the cytochrome P450 peroxygenase enzymes. *Biochem Soc Trans* **2018,** *46* (1), 183-196.

31. Rude, M. A.; Baron, T. S.; Brubaker, S.; Alibhai, M.; Del Cardayre, S. B.; Schirmer, A., Terminal Olefin (1-Alkene) Biosynthesis by a Novel P450 Fatty Acid Decarboxylase from Jeotgalicoccus Species. *Appl Environ Microb* **2011,** *77* (5), 1718-1727.

32. Amaya, J. A.; Rutland, C. D.; Makris, T. M., Mixed regiospecificity compromises alkene synthesis by a cytochrome P450 peroxygenase from Methylobacterium populi. *J Inorg Biochem* **2016,** *158*, 11-16.
33. Belcher, J.; McLean, K. J.; Matthews, S.; Woodward, L. S.; Fisher, K.; Rigby, S. E. J.; Nelson, D. R.; Potts, D.; Baynham, M. T.; Parker, D. A.; Leys, D.; Munro, A. W., Structure and Biochemical Properties of the Alkene Producing Cytochrome P450 OleTJE (CYP152L1) from the Jeotgalicoccus sp 8456 Bacterium. *J Biol Chem* **2014,** *289* (10), 6535-6550.
34. Matsunaga, I.; Yokotani, N.; Gotoh, O.; Kusunose, E.; Yamada, M.; Ichihara, K., Molecular cloning and expression of fatty acid alpha-hydroxylase from Sphingomonas paucimobilis. *J Biol Chem* **1997,** *272* (38), 23592-23596.
35. Matsunaga, I.; Ueda, A.; Fujiwara, N.; Sumimoto, T.; Ichihara, K., Characterization of the ybdT gene product of Bacillus subtilis: novel fatty acid beta-hydroxylating cytochrome P450. *Lipids* **1999,** *34* (8), 841-846.
36. Zhao, J.; de Serrano, V.; Dumarieh, R.; Thompson, M.; Ghiladi, R. A.; Franzen, S., The role of the distal histidine in H2O2 activation and heme protection in both peroxidase and globin functions. *J Phys Chem B* **2012,** *116* (40), 12065-12077.
37. Poulos, T. L.; Kraut, J., The stereochemistry of peroxidase catalysis. *J Biol Chem* **1980,** *255* (17), 8199-8205.
38. Poulos, T. L.; Freer, S. T.; Alden, R. A.; Edwards, S. L.; Skogland, U.; Takio, K.; Eriksson, B.; Xuong, N.; Yonetani, T.; Kraut, J., The crystal structure of cytochrome c peroxidase. *J Biol Chem* **1980,** *255* (2), 575-580.

39. Huang, X.; Groves, J. T., Oxygen Activation and Radical Transformations in Heme Proteins and Metalloporphyrins. *Chem Rev* **2018,** *118* (5), 2491-2553.
40. Grant, J. L.; Hsieh, C. H.; Makris, T. M., Decarboxylation of fatty acids to terminal alkenes by cytochrome P450 compound I. *J Am Chem Soc* **2015,** *137* (15), 4940-4943.
41. Grant, J. L.; Mitchell, M. E.; Makris, T. M., Catalytic strategy for carbon-carbon bond scission by the cytochrome P450 OleT. *Proc Natl Acad Sci USA* **2016,** *113* (36), 10049-10054.
42. Rude, M. A.; Baron, T. S.; Brubaker, S.; Alibhai, M.; Del Cardayre, S. B.; Schirmer, A., Terminal olefin (1-alkene) biosynthesis by a novel p450 fatty acid decarboxylase from Jeotgalicoccus species. *Appl Environ Microbiol* **2011,** *77* (5), 1718-1727.
43. Mitchell, M.; Grant, J.; Hsieh, C.; Makris, T., Fatty acid specificity of the P450 decarboxylase OleT(JE). *Faseb J* **2014,** *28* (1).
44. Liu, Y.; Wang, C.; Yan, J.; Zhang, W.; Guan, W.; Lu, X.; Li, S., Hydrogen peroxide-independent production of alpha-alkenes by OleTJE P450 fatty acid decarboxylase. *Biotechnol Biofuels* **2014,** *7* (1), 28.
45. Dennig, A.; Kuhn, M.; Tassoti, S.; Thiessenhusen, A.; Gilch, S.; Bulter, T.; Haas, T.; Hall, M.; Faber, K., Oxidative Decarboxylation of Short-Chain Fatty Acids to 1-Alkenes. *Angew Chem Int Ed Engl* **2015,** *54* (30), 8819-8822.
46. Fang, B.; Xu, H.; Liu, Y.; Qi, F.; Zhang, W.; Chen, H.; Wang, C.; Wang, Y.; Yang, W.; Li, S., Mutagenesis and redox partners analysis of the P450 fatty acid decarboxylase OleTJE. *Sci Rep* **2017,** *7*, 44258.

47. Belcher, J.; McLean, K. J.; Matthews, S.; Woodward, L. S.; Fisher, K.; Rigby, S. E.; Nelson, D. R.; Potts, D.; Baynham, M. T.; Parker, D. A.; Leys, D.; Munro, A. W., Structure and biochemical properties of the alkene producing cytochrome P450 OleTJE (CYP152L1) from the Jeotgalicoccus sp. 8456 bacterium. *J Biol Chem* **2014,** *289* (10), 6535-6550.

48. Wise, C. E.; Hsieh, C. H.; Poplin, N. L.; Makris, T. M., Dioxygen Activation by the Biofuel-Generating Cytochrome P450 OleT. *ACS Catal* **2018,** *8* (10), 9342-9352.

49. Finking, R.; Marahiel, M. A., Biosynthesis of nonribosomal peptides. *Annu Rev Microbiol* **2004,** *58*, 453-488.

50. Fischbach, M. A.; Walsh, C. T., Assembly-line enzymology for polyketide and nonribosomal Peptide antibiotics: logic, machinery, and mechanisms. *Chem Rev* **2006,** *106* (8), 3468-3496.

51. Frueh, D. P.; Arthanari, H.; Koglin, A.; Vosburg, D. A.; Bennett, A. E.; Walsh, C. T.; Wagner, G., Dynamic thiolation-thioesterase structure of a non-ribosomal peptide synthetase. *Nature* **2008,** *454* (7206), 903-906.

52. Dittmann, J.; Wenger, R. M.; Kleinkauf, H.; Lawen, A., Mechanism of cyclosporin A biosynthesis. Evidence for synthesis via a single linear undecapeptide precursor. *J Biol Chem* **1994,** *269* (4), 2841-2846.

53. Lin, S.; Huang, T.; Shen, B., Tailoring enzymes acting on carrier protein-tethered substrates in natural product biosynthesis. *Methods Enzymol* **2012,** *516*, 321-343.

54. Du, L.; Sanchez, C.; Chen, M.; Edwards, D. J.; Shen, B., The biosynthetic gene cluster for the antitumor drug bleomycin from Streptomyces verticillus ATCC15003 supporting functional interactions between nonribosomal peptide synthetases and a polyketide synthase. *Chem Biol* **2000,** *7* (8), 623-642.

55. Lo Grasso, L.; Maffioli, S.; Sosio, M.; Bibb, M.; Puglia, A. M.; Alduina, R., Two Master Switch Regulators Trigger A40926 Biosynthesis in Nonomuraea sp. Strain ATCC 39727. *J Bacteriol* **2015,** *197* (15), 2536-2544.

56. Park, S. R.; Yoo, Y. J.; Ban, Y. H.; Yoon, Y. J., Biosynthesis of rapamycin and its regulation: past achievements and recent progress. *J Antibiot (Tokyo)* **2010,** *63* (8), 434-441.

57. Pfeifer, B. A.; Wang, C. C.; Walsh, C. T.; Khosla, C., Biosynthesis of Yersiniabactin, a complex polyketide-nonribosomal peptide, using Escherichia coli as a heterologous host. *Appl Environ Microbiol* **2003,** *69* (11), 6698-6702.

58. Walsh, C. T.; Chen, H.; Keating, T. A.; Hubbard, B. K.; Losey, H. C.; Luo, L.; Marshall, C. G.; Miller, D. A.; Patel, H. M., Tailoring enzymes that modify nonribosomal peptides during and after chain elongation on NRPS assembly lines. *Curr Opin Chem Biol* **2001,** *5* (5), 525-534.

59. Samel, S. A.; Marahiel, M. A.; Essen, L. O., How to tailor non-ribosomal peptide products--new clues about the structures and mechanisms of modifying enzymes. *Mol Biosyst* **2008,** *4* (5), 387-393.

60. Vaillancourt, F. H.; Yeh, E.; Vosburg, D. A.; O'Connor, S. E.; Walsh, C. T., Cryptic chlorination by a non-haem iron enzyme during cyclopropyl amino acid biosynthesis. *Nature* **2005,** *436* (7054), 1191-1194.

61. Cryle, M. J.; Meinhart, A.; Schlichting, I., Structural characterization of OxyD, a cytochrome P450 involved in beta-hydroxytyrosine formation in vancomycin biosynthesis. *J Biol Chem* **2010,** *285* (32), 24562-24574.
62. Haslinger, K.; Maximowitsch, E.; Brieke, C.; Koch, A.; Cryle, M. J., Cytochrome P450 OxyBtei catalyzes the first phenolic coupling step in teicoplanin biosynthesis. *Chembiochem* **2014,** *15* (18), 2719-2728.
63. Marahiel, M. A., A structural model for multimodular NRPS assembly lines. *Nat Prod Rep* **2016,** *33* (2), 136-140.
64. Konz, D.; Klens, A.; Schorgendorfer, K.; Marahiel, M. A., The bacitracin biosynthesis operon of Bacillus licheniformis ATCC 10716: molecular characterization of three multi-modular peptide synthetases. *Chem Biol* **1997,** *4* (12), 927-937.
65. Uhlmann, S.; Sussmuth, R. D.; Cryle, M. J., Cytochrome p450sky interacts directly with the nonribosomal peptide synthetase to generate three amino acid precursors in skyllamycin biosynthesis. *ACS Chem Biol* **2013,** *8* (11), 2586-2596.
66. Matthews, M. L.; Krest, C. M.; Barr, E. W.; Vaillancourt, F. H.; Walsh, C. T.; Green, M. T.; Krebs, C.; Bollinger, J. M., Substrate-triggered formation and remarkable stability of the C-H bond-cleaving chloroferryl intermediate in the aliphatic halogenase, SyrB2. *Biochemistry* **2009,** *48* (20), 4331-4343.
67. Haslinger, K.; Brieke, C.; Uhlmann, S.; Sieverling, L.; Sussmuth, R. D.; Cryle, M. J., The structure of a transient complex of a nonribosomal peptide synthetase and a cytochrome P450 monooxygenase. *Angew Chem Int Ed Engl* **2014,** *53* (32), 8518-8522.

68. Walsh, C. T.; Chen, H. W.; Keating, T. A.; Hubbard, B. K.; Losey, H. C.; Luo, L. S.; Marshall, C. G.; Miller, D. A.; Patel, H. M., Tailoring enzymes that modify nonribosomal peptides during and after chain elongation on NRPS assembly lines. *Curr Opin Chem Biol* **2001,** *5* (5), 525-534.
69. Chen, H.; Hubbard, B. K.; O'Connor, S. E.; Walsh, C. T., Formation of beta-hydroxy histidine in the biosynthesis of nikkomycin antibiotics. *Chem Biol* **2002,** *9* (1), 103-12.
70. Kokona, B.; Winesett, E. S.; von Krusenstiern, A. N.; Cryle, M. J.; Fairman, R.; Charkoudian, L. K., Probing the selectivity of beta-hydroxylation reactions in non-ribosomal peptide synthesis using analytical ultracentrifugation. *Anal Biochem* **2016,** *495*, 42-51.
71. Ueki, M.; Galonic, D. P.; Vaillancourt, F. H.; Garneau-Tsodikova, S.; Yeh, E.; Vosburg, D. A.; Schroeder, F. C.; Osada, H.; Walsh, C. T., Enzymatic generation of the antimetabolite gamma,gamma-dichloroaminobutyrate by NRPS and mononuclear iron halogenase action in a streptomycete. *Chem Biol* **2006,** *13* (11), 1183-1191.
72. Chen, H.; Hubbard, B. K.; O'Connor, S. E.; Walsh, C. T., Formation of beta-hydroxy histidine in the biosynthesis of nikkomycin antibiotics. *Chem Biol* **2002,** *9* (1), 103-112.
73. Wise, C. E.; Makris, T. M., Recruitment and Regulation of the Non-ribosomal Peptide Synthetase Modifying Cytochrome P450 Involved in Nikkomycin Biosynthesis. *ACS Chem Biol* **2017,** *12* (5), 1316-1326.

CHAPTER 2

Dioxygen Activation by the Biofuel-Generating Cytochrome P450 OleT[1]

[1] Reprinted with Permission from: Wise, C. E.; Hsieh, C. H.; Poplin, N. L.; and Makris, T. M. Dioxygen Activation by the Biofuel-Generating Cytochrome P450 OleT. *ACS Catalysis* **2018**, *8* (10), 9342-9352. Copyright 2018 American Chemical Society.

2.1 ABSTRACT

OleT, a recently discovered member of the CYP152 family of cytochrome P450s, catalyzes a unique decarboxylation reaction, converting free fatty acids into 1-olefins and carbon dioxide using H_2O_2 as an oxidant. The C-C reaction proceeds through hydrogen atom abstraction by an iron(IV)-oxo intermediate known as Compound I. The capacity of the enzyme for generating important commodity chemicals and liquid biofuels has inspired a flurry of investigations seeking to maximize its biosynthetic potential. One common approach has sought to address the limitations imposed by the H_2O_2 co-substrate, particularly for *in vivo* applications. Numerous reports have shown relatively efficient decarboxylation activity with various combinations of the enzyme with pyridine nucleotides, biological redox donors, and dioxygen, implicating a mechanism whereby OleT can generate Compound I via a canonical P450 O_2 dependent reaction scheme. Here, we have applied transient kinetics, cryoradiolysis, and steady state turnover studies to probe the precise origins of OleT turnover from surrogate redox systems. Electron transfer from several redox donors is prohibitively sluggish and the enzyme is unable to form the hydroperoxo-ferric adduct that serves as a critical precursor to Compound I. Despite the ability for OleT to readily bind O_2 once it is reduced, autoxidation of the enzyme and redox partners leads to the generation of H_2O_2, which is ultimately responsible for the vast majority of turnover. These results illuminate several strategies for improving OleT for downstream biocatalytic applications.

2.2 INTRODUCTION

The biocatalytic conversion of metabolites from the phylogenetically ubiquitous fatty acid synthesis (FAS) pathway to hydrocarbons provides a renewable resource for the supplementation or replacement of petroleum-derived transportation fuels. Collective efforts from the past decade have resulted in the elucidation of several biochemical routes for hydrocarbon biosynthesis. A great deal of these pathways are comprised of enzymes that utilize a myriad of iron-containing cofactors (reviewed in [1]) that activate O_2 or H_2O_2 for the transformation of C_n chain length fatty aldehyde or fatty acids to C_{n-1} alkanes [2, 3] or alkenes [4-6] respectively. A common feature of these enzymes is the utilization of catalytic sites for carbon-carbon cleaving reactions that resemble or duplicate those typically associated with monoxygenation chemistry. In addition to discerning the precise molecular basis for this enzymatic reprogramming, a global challenge is to now leverage these catalysts in a suitable recombinant host with the hope of providing an economically viable route for advanced biofuel production.

To date, the vast majority of attempts at recombineering genetically-tractable organisms such as *E. coli* [3, 7, 8] or *S. cerevisiae* [9, 10] for the production of FAS-derived biofuels have utilized the introduction of a two-step pathway from cyanobacteria (Figure 2.1A, lower pathway).[3] This route makes use of an acyl-ACP reductase (AAR) to reduce an acyl carrier protein (ACP) linked hydrocarbon from the FAS pathway to generate a free C_n aldehyde. In the subsequent step, a non-heme diiron enzyme known as aldehyde deformylating oxygenase (ADO) forms the C_{n-1} alkane. This pathway has been successfully introduced into several heterologous hosts for the production of gaseous and liquid fuels. [3, 8, 10] Despite providing an excellent template for the transplantation of a pathway to enable

advanced biofuel production, the resulting titers that result from these bioengineering efforts are often too low to be economically viable. This is attributed to the sluggish rate of ADO catalysis that originates from rate-limiting electron transfer steps, [11-13] inhibitory side-products that can be generated both by ADO [14] and AAR, [15] and the relative inefficiency of the AAR step for producing the necessary substrate aldehydes.

A potentially attractive alternative route for biocatalytic fuel generation may be provided by a recently discovered group of cytochrome P450s (CYPs) from the CYP152 family named OleT [4] that have the ability to generate terminal olefins from fatty acid substrates in a single step (Figure 2.1A, upper pathway). [16, 17] In addition to serving as valuable fuel components, the alkenes produced by OleT can also be utilized as important synthetic precursors for a wide array of commercially valuable commodity chemicals. Importantly, the synthetic biology tools necessary for generating large amounts (as high as grams per liter) of free fatty acids with carbon chain lengths that can be finely-tuned for different types of transportation fuels have been developed for several species.[10, 18, 19] OleT, in turn, has been demonstrated to metabolize a broad range of fatty acid substrates *in vitro* with catalytic rates [20-23] that far exceed those of ADO.

A limitation for leveraging OleT catalysis, particularly for *in vivo* bioengineering platforms, is its requirement for H_2O_2 as a cosubstrate for the oxidation of the heme-iron to generate the high-valent intermediate known as Compound I (intermediate 7 in Figure 2.1B). Transient kinetic studies from our laboratory have shown that fatty acid decarboxylation is initiated by C-H bond cleavage by this ferryl intermediate. [16, 17, 22, 24] The efficient utilization of H_2O_2 by OleT and its orthologs differs from the vast majority of CYPs that instead generate Compound I through the binding and activation of

atmospheric dioxygen using reducing equivalents that are ultimately derived from pyridine dinucleotide and delivered through an auxiliary redox chain. In contrast, the activation of H_2O_2 to initiate OleT decarboxylation is a process that is highly inefficient for most O_2 dependent CYPs, even though it has long served as a highly desirable attribute for leveraging key industrial transformations.[25, 26] This inexpensive oxidant (at least 10,000 fold cheaper than reduced nicotinamide on a molar basis) is easily scalable and eliminates the need for auxiliary redox proteins.

OleT has been leveraged with biological [27] and photochemical (e.g. dye-mediator) [28, 29] approaches that generate H_2O_2 in a controlled manner *in situ* and can thus support high levels of alkene production *in vitro* by preventing unwanted catalyst inactivation that occurs upon exposure to excess oxidant.[30] The efficient production of olefins *in vivo* has remained more elusive as reactive oxygen species (ROS) are ill tolerated by most species and highly efficient cellular detoxification mechanisms have evolved to prevent their accumulation in a cellular milieu. Thus a major goal for developing *in vivo* platform for alkene generation has been to redirect OleT to utilize O_2 with a suitably poised biological redox chain. To address this, a number of recent reports have shown that a combination of pyridine nucleotide (NAD(P)H) and surrogate redox partners can support alkene formation by OleT [20, 21, 23, 31-33] and orthologous CYP152 decarboxylases [34] and hydroxylases [35] *in vitro*. Redox chains have included genetic fusions of OleT with RhFred,[36] a donor that can be fused to and serve as a surrogate redox donor to several CYPs,[37] the reductase domain of cytochrome P450 BM3,[33] as well as multi-component systems such as the putidaredoxin (Pd)/putidaredoxin reductase (PdR) system [20, 21, 23, 34] that is native to the CYP camphor 5-hydroxylase CYP101 ($P450_{CAM}$).[38] Although these have shown to promote FA

decarboxylation in studies using purified enzymes or cell-free extracts, in some cases resulting in total turnover numbers (TTON > 100), attempts to leverage catalysis *in vivo* has been met with much more limited success.[4, 32, 39] Nonetheless, the realization of 1-olefin production using OleT and surrogate redox donors has led some to speculate that CYP152s may natively use O_2 and electrons, rather than H_2O_2.[20] However, a recent study has cast some doubt as the inclusion of catalase in reactions of an OleT ortholog eliminates some catalytic activity. [34]

If dioxygen dependent catalysis is indeed supported by OleT, the catalytic cycle would most likely need to be comprised of the same set of steps and intermediates that are common to the vast majority of dioxygen-dependent CYPs and have been resolved over the course of several decades. These are designated by the purple arrows in Figure 2.1B and we refer to individual intermediates by their corresponding number throughout the manuscript. Briefly, oxygen activation by OleT would need to involve reduction of the substrate-bound enzyme, the subsequent binding of O_2, and finally, the proton-linked processes that enable heterolysis of the O-O bond to form Compound I. The efficiency of these steps have yet to be clarified for OleT or for any other CYP152. Here, we utilize transient kinetics to probe the rate of electron transfer from several biological redox donors to OleT, examine the reactivity of the ferrous enzyme with dioxygen, and use cryoradiolytic methods to address whether OleT can catalyze O-O bond cleavage. Together with turnover studies that reveal the origins for the observed turnover by OleT from pyridine nucleotide in the aforementioned studies, these results highlight several features that hamper dioxygen activation by OleT. Furthermore, they serve to distinguish the clear boundaries between oxygenase and peroxygenase catalysis. Ultimately this work may

provide an important roadmap for enabling future bioengineering efforts to develop new platforms for sustainable biofuel synthesis.

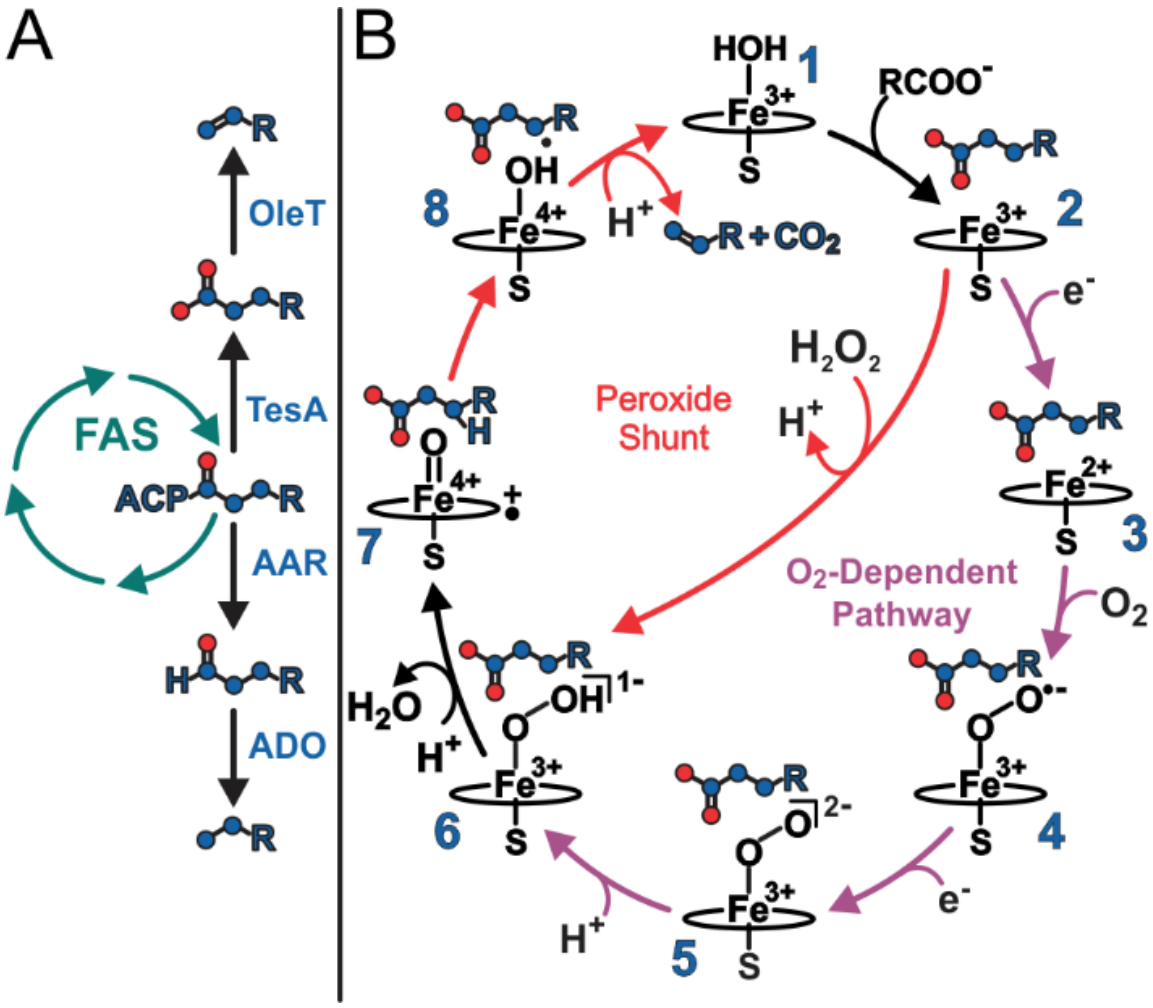

Figure 2.1. Biofuel production via fatty acid synthesis (A) and the P450 catalytic cycle (B). (**A**) Hijacking of the fatty acid synthesis (FAS) pathway for advanced biofuel synthesis. In the lower cyanobacterial pathway, the acyl carrier protein (ACP) linked acyl group is reduced by an acyl-ACP reductase (AAR) and further metabolized by the dinuclear iron enzyme aldehyde deformylating oxygenase (ADO) to an C_{n-1} alkane. In the upper pathway, a C_{n-1} olefin is formed from the generation of a free fatty acid by the thioesterase TesA and subsequent decarboxylation by the cytochrome P450 OleT. (**B**) The H_2O_2 shunt mechanism (red) for the formation of the reactive Compound I oxidant in OleT versus a canonical dioxygen dependent mechanism of cytochrome P450 involving heme-iron reduction, O_2 binding, and O-O bond heterolysis to form Compound I (purple).

2.3 RESULTS AND DISCUSSION

2.3.1 Sluggish electron transfer to OleT from biological redox donors

The previously measured redox properties for eicosanoic acid bound OleT suggest that the high-spin (HS) enzyme (**2**) exhibits an unusually high redox potential (E_m ~ -100 mV versus NHE) [40] that could provide a favorable thermodynamic driving force for electron transfer from a redox partner such as Pd (E_m ~ -240 mV) to occur. [41] The binding of Pd to CYP101 involves a transient association of the two proteins using a complementary electrostatic interface.[42] Several basic residues (e.g. Arg109 and Arg112) [43, 44] on CYP101 are critical for mediating this interaction. A comparison of the surface electrostatics of CYP101 and OleT shows that the latter enzyme lacks this potential binding interface, but has another positively charged surface that could possibly serve as a favorable docking site (Figure 2.2).

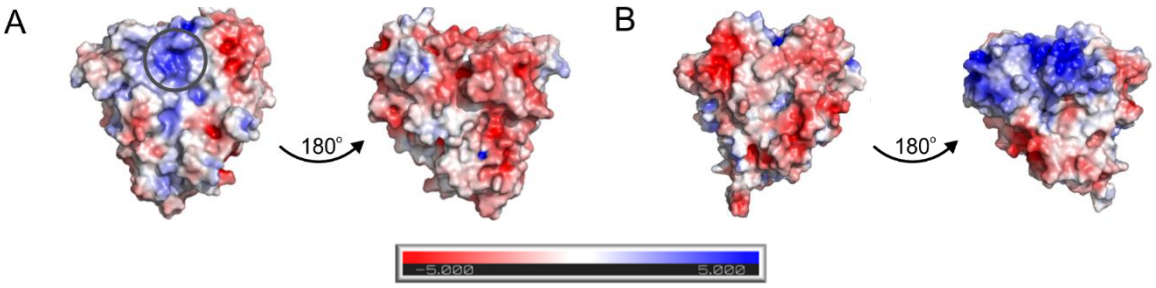

Figure 2.2. Molecular surfaces of (A) CYP101 and (B) OleT showing the charge distribution of both proteins. This was generated by the Adaptive Poisson-Boltzmann Server plugin of Pymol. Acidic and basic functional groups are shown in red and blue respectively. The docking interface for putidaredoxin on CYP101, determined by the Poulos laboratory,[42] is circled for reference.

The efficiency of the Pd/PdR/NADH redox chain with OleT was directly examined using transient kinetic methods. A solution containing eicosanoic acid (EA) bound OleT, Pd and PdR was rapidly mixed with excess NADH in an anoxic atmosphere containing

carbon monoxide and catalase to ensure that any H_2O_2 that could result from uncoupling reactions was quenched. Successful electron transfer to OleT from pyridine nucleotide would result in the formation of the ferrous carbonmonoxy-bound (Fe^{2+}-CO) enzyme with a Soret maximum at 446 nm. The photodiode array (PDA) traces that resulted from the rapid mixing of OleT:Pd:PdR in a 1:10:10 ratio with a excess NADH are shown in Figure 2.3A. The HS substrate-bound enzyme, with a Soret maximum at 395 nm, very slowly converts to the Fe^{2+}-CO state. Even over the course of 1,000 seconds, only a fraction of the enzyme (~ 50 %) was reduced. The time course for reduction at 450 nm is shown in the inset of Figure 2.3A. Fitting of the time course to a single exponential process revealed an observed electron transfer rate k_{ET}^{obs} = 0.0011 ± 0.0004 s^{-1}. Notably, this reduction rate is over four orders of magnitude slower than that of Pd to HS camphor bound CYP101 (k_{ET} ~ 20 s^{-1})[45] and primary electron transfer rates for other native P450:redox pairs (e.g. [46-48]). This process is also more sluggish than the reported turnover frequency of OleT using the Pd/PdR/NADPH couple (~0.01 s^{-1} at room temperature).[20, 21]

In attempts to explore the origin for the slow kinetics for first electron transfer and possibly improve upon the efficiency of this process for *in vivo* studies, we turned our attention to an an alternative flavin-containing redox partner that is native to *E. coli* termed NAD(P)H:flavin oxidoreductase (Fre).[49] Fre is thought to have a labile flavin cofactor [50, 51] and its use could eliminate the need for forming a preorganized binding interface with OleT. Although Fre is known to serve as a redox partner to several classes of enzymes as well as cytosolic Fe^{3+}, it is not known to interact directly with CYPs. Nonetheless, Fre was able to readily convert HS camphor-bound CYP101 to the ferrous state but failed to support camphor 5-hydroxylation (Figure 2.4 [S2]). This stems from the well-known inability for

redox donors other than Pd to provide the second electron required for O_2 activation in CYP101, where binding of the redox partner also serves an indispensable effector role.[52] It is also consistent with the inability of a solitary flavin cofactor to synchronize the sequential and timed delivery of two reducing equivalents to a CYP. Nonetheless, we tested if this system could be more efficient than Pd for primary electron transfer to OleT. Rapid mixing of solution containing a 1:10:10 ratio of HS OleT:FAD:Fre with excess NADH resulted in almost complete conversion of HS OleT to the ferrous-CO form (Figure 2.5B). Moreover, the observed electron transfer rate, shown in the inset of Figure 2.5B, indicated that the process is an order of magnitude faster (k_{ET}^{obs} = 0.0105 ± 0.0004 s^{-1}) than the Pd/PdR/NADH system.

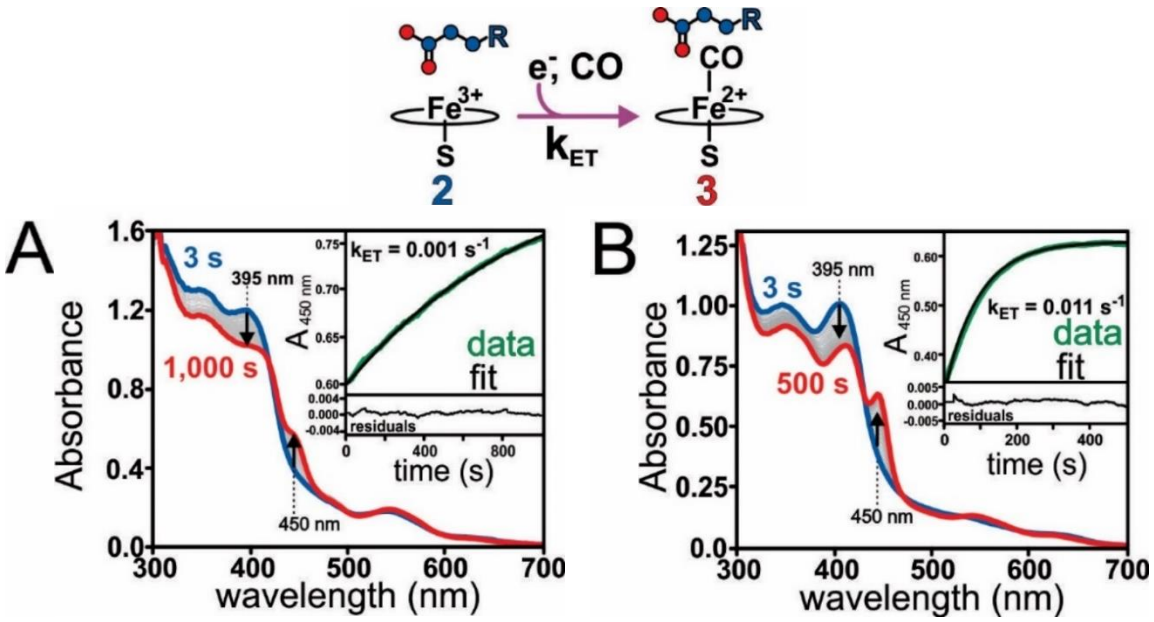

Figure 2.3. Primary electron transfer to eicosanoic acid bound OleT. Eicosanoic acid bound high-spin OleT was rapidly mixed with a solution containing (**A**) putidaredoxin (Pd), putidaredoxin reductase (PdR), and NADH or (**B**) flavin reductase (Fre), flaving adenine dinucleotide (FAD), and NADH, at 4 °C in the presence of catalase and carbon monoxide. Concentrations after mixing were 5 µM OleT and 125 µM NADH and either 50 µM Pd, 50 µM PdR or 50 µM Fre, 50 µM FAD respectively. The insets shows single exponential fitting of the timecourse for reduced carbonmonoxy bound OleT formation followed at 450 nm with observed electron transfer rates (k_{ET}) indicated.

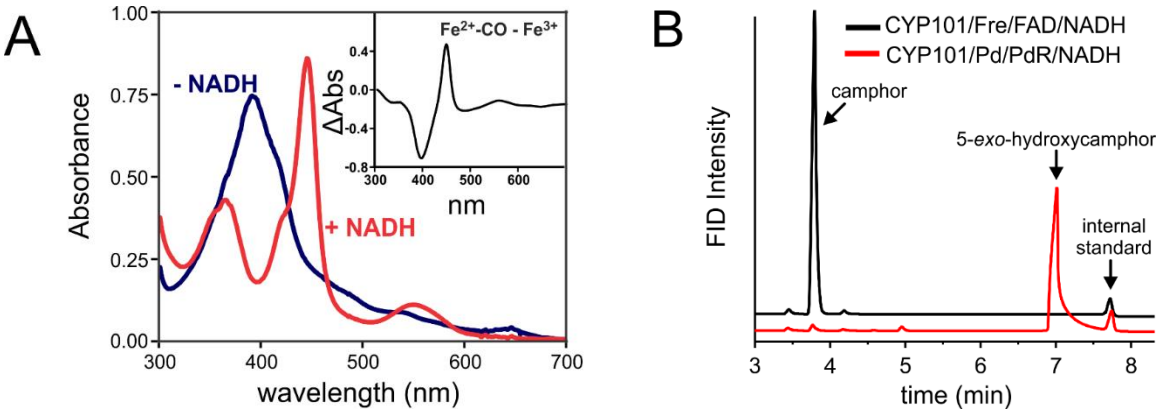

Figure 2.4. Reduction and attempted turnover of CYP101 with Fre and FAD. Analysis of the potential for E. coli NAD(P)H flavin reductase (Fre) to support primary electron transfer (**A**) and turnover (**B**) with the camphor 5-hydroxylase CYP101. UV/visible spectra in (**A**) show the reaction of camphor-bound CYP101 (10 μM), FAD (10 μM), and Fre (10 μM) before (red) or shortly following (blue) the addition of 100 μM NADH in a carbon monoxide (CO) atmosphere. The inset shows the Fe^{2+}-CO minus Fe^{3+} difference spectrum, indicating that electron transfer has occurred. The gas chromatograms in (**B**) show a comparison of the reactions of CYP101 with the Fre/FAD/NADH (black) or Pd/PdR/NADH turnover systems (red). Reactions included 1 μM CYP101, 1 mM camphor, 50 μM catalase, and 2 mM NADH, and either 10 μM FAD and 10 μM FAD Fre (black) or 2.2 μM PdR and 10 μM Pd. Following incubation for 1 hour at 25°C, reactions were quenched and extracted with chloroform and 200 nmol 3-bromocamphor as an internal standard. Products were separated by a DB-5 GC column using the following oven temperature gradients (170°C, 3 min; 2°C min^{-1} to 200 °C) and were identified by comparison to the flame ionization detector (FID) chromatograms of authentic compounds.

2.3.2 Favorable Binding of Dioxygen to Ferrous OleT

Following electron transfer, O_2-driven catalysis by OleT would necessitate the binding of dioxygen to the ferrous-iron (3) to form a ferric-superoxide species (4). To our knowledge, this process has yet to be examined for any CYP152. Ferrous OleT:EA, prepared via reduction with dithionite, was rapidly mixed with a solution containing saturating O_2 (~2 mM) at 4 °C (Figure 2.5A). Figure 2.5A shows the photodiode traces corresponding to the first 200 ms of the reaction. The ferrous enzyme, with a λ_{max} ~ 412 nm, rapidly decays to form a species with a Soret maximum at 426 nm and a predominant Q band at 550 nm with a small shoulder at 580 nm. The Soret maximum is red-shifted

relative to many[53, 54] but not all[55] O_2-bound CYPs and is well within the large range observed for comparable species in thiolate heme proteins such as chloroperoxidase (CPO) [56] and nitric oxide synthase (NOS).[57, 58] The difference in absorbance features of oxyOleT versus those of many other CYPs may arise from differences at the proximal "cys-pocket" or from interactions with bound dioxygen at the distal pocket, both of which are significantly different in CYP152s. A particularly salient example of the perturbation of the oxyferrous spectrum by the distal pocket is found in oxyNOS, where interactions with the bound L-arginine substrate induce a similar spectral shift, rendering the ligand more superoxide-like in character.[59] The binding of dioxygen to the ferrous enzyme was followed by monitoring the time course for absorbance changes at 440 nm, yielding an observed rate of formation $k_{obs} \sim 50\ s^{-1}$ (Figure 2.5A, inset). The binding process was further characterized by monitoring the formation of oxy-OleT with varying concentrations of dioxygen (Figure 2.5B). The on-rate, determined from the slope of the plot, yields a bimolecular rate constant ($k_{on} = 5.7 \pm 0.5 \times 10^4\ M^{-1}\ s^{-1}$). This value is quite similar to those measured for O_2-dependent CYPs, revealing that O_2 binding characteristics are largely preserved. [1, 53, 60, 61]

2.3.3 OxyOleT Decays Slowly to the Low-Spin Enzyme and Forms Product

For coupled O_2 driven catalysis to occur, the Fe^{3+}-O_2^- complex (4) must be sufficiently stable to allow for second electron transfer and ensuing O-O heterolysis, thereby preventing the unwanted production of superoxide. The PDA traces corresponding to the decomposition of oxyOleT from 200 ms to 500 s and the full kinetics of the process are shown in Figures 2.6A and 2.6B respectively. The spectra reveal a very slow and relatively complex process whereby the OleT oxy-complex appears to directly decay to the

low-spin enzyme (λ_{max} ~ 418 nm) over the course of 10 minutes at 4 °C. No spectroscopically distinct intermediate accumulates during decomposition as revealed by several isosbestic points for the transtion. The timecourse for oxyOleT decay required a two summed exponential function for adequate fitting. The predominant phase, accounting for ~90 % of the spectral amplitude exhibits a rate of ~ 0.004 s^{-1} while the smaller phase (~10 % amplitude) has a decay rate of ~ 1 s^{-1}. This kinetic behavior could in principle result from a decay process involving multiple steps or more likely from multiple configurations of the oxy-complex which decay at different rates. One plausible source of this heterogeneity could arise from a small fraction of low-spin, substrate free enzyme present at 4 °C, typically 10 – 15%, under the limiting EA used to prepare enzyme:substrate complexes for the single-turnover studies described in the following section. To test this, the autoxidation properties of substrate-free OleT were examined, revealing a much higher rate of decomposition (~ 10 s^{-1}) than the substrate-bound enzyme (Figure 2.7).

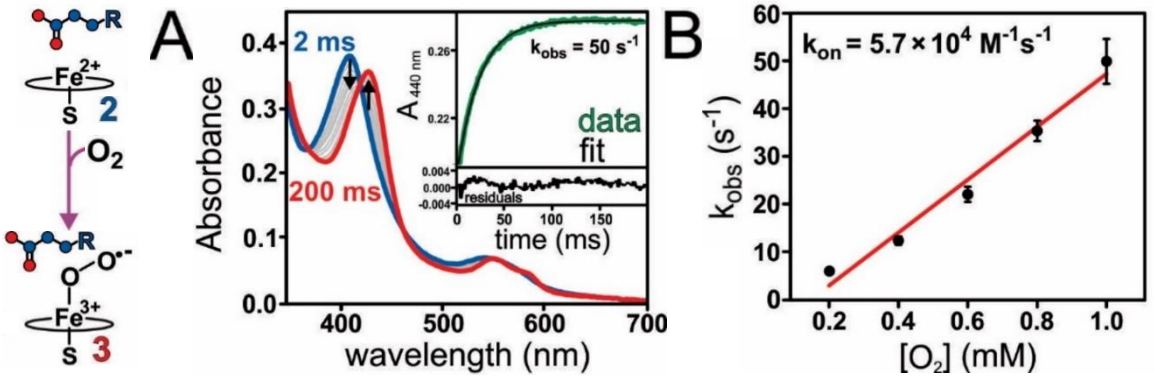

Figure 2.5. Dioxygen binding to ferrous substrate-acid bound OleT. (**A**) The dithionite reduced eicosanoic acid bound enzyme (10 µM, blue spectrum) was rapidly mixed with 2 mM O_2 at 4 °C. The inset shows the time course for oxyOleT (red spectrum) formation at 440 nm. Single exponential fitting reveals a rate of formation ~ 50 s^{-1}. (**B**) O_2 concentration dependence oxyOleT formation. The slope of the plot reveals the bimolecular rate for dioxygen binding, k_{on} = 5.7 x 10^4 $M^{-1}s^{-1}$.

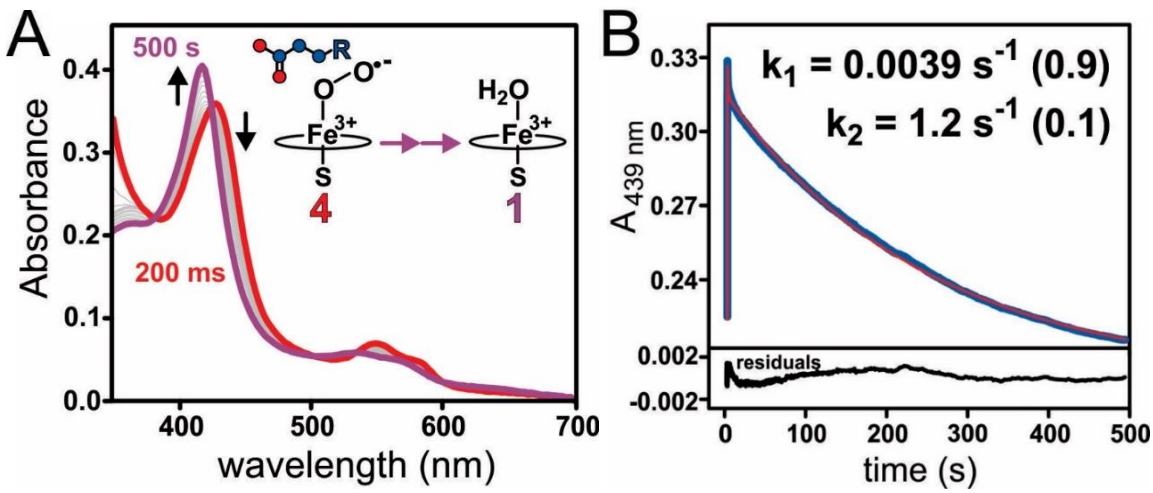

Figure 2.6. Autoxidation of oxyOleT at 4 ºC monitored by stopped flow spectroscopy. (**A**) The oxy-complex (red spectrum) decays over the course of 500 s to the low-spin ferric enzyme (violet spectrum). (**B**) The time course for oxyOleT formation and decay at 440 nm. Fitting required a three summed exponential with the two reciprocal relaxation times corresponding to decay processes (in s^{-1}) shown and their relative spectral amplitudes in parentheses. Protein and O_2 concentrations were identical to those described in Figure 2.3A.

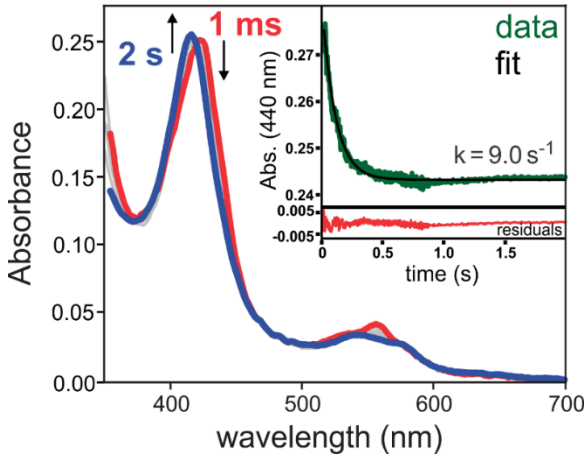

Figure 2.7. Autoxidation properties of substrate free oxy-OleT. The substrate-free enzyme (5 µM) was rapidly mixed with 2 mM O_2 at 4ºC. Oxy-OleT (red spectrum) rapidly decays to the ferric low-spin enzyme (blue spectrum). The inset shows the time course for decay at 440 nm. Single exponential fitting reveals a rate of decay ~ 9 s^{-1}.

Overall, the kinetics and thermodynamics (Figure 2.8) for oxyOleT decomposition reveal an intermediate that in the presence of substrate is amongst the most stable of any CYP reported to date and very similar to the bacterial archetype CYP101.[52] At first glance, the substrate-mediated stabilization of oxyOleT (by ~3 orders of magnitude) by the fatty acid substrate would appear to be a highly advantageous trait to ensure that the consumption of pyridine nucleotide can be coupled to product formation. Despite its stability, however, the rate for oxyOleT decay is still comparable to primary electron transfer from Pd or Fre/FAD to OleT, and for many CYPs, delivery of the second electron required to reduce the oxy-intermediate to the peroxo-level can be significantly slower.[62, 63] The most intriguing aspect of the decay process, however, is that the HS EA-bound form of the enzyme fails to regenerate at the end of the reaction. Single turnover transient kinetics studies have shown that, upon reaction with excess H_2O_2, HS OleT converts to the LS form [40] with intervening Compound I (7) [16, 22] and Compound II (8) intermediates.[17] The decay of the latter intermediate, accompanied by a rate-limiting product release step, [24] results in formation of the 1-alkene. Although failure to restore the HS state from oxyOleT could signal the metabolism of the substrate it could also stem from alteration of the substrate-binding mode, or release of the substrate from the enzyme altogether, upon reduction and oxygenation. This prompted us to more closely examine the autoxidation properties of oxyOleT in the presence of catalase in the reaction mixture. The PDA spectra that correspond to oxyOleT decay (from 200 ms to 1000s) are shown in Figure 2.9A. Due to the overlapping background absorption of catalase, the difference spectra generated by substracting the spectrum of oxyOleT (4) from those corresponding to later timepoints are more revealing. Difference spectra are compared for reactions that included or omitted

catalase in Figure 2.9B. The features with positive absorption (pointing upward) are associated with the developing species while those pointing downward correspond to oxyOleT. The negative absorbance features are quite similar in both sets of difference spectra, as expected, but the positive features reveal significant differences in the identity of the oxyOleT decay product. The difference spectra obtained from reactions where catalase was omitted reveal a dominant positive feature at 418 nm and a much smaller shoulder at 396 nm, suggesting that oxyOleT largely (> 80 %) decays to the LS form. On the other hand, the addition of catalase resulted in the regeneration of the HS enzyme-substrate complex with a maximal positive absorption feature at 396 nm.

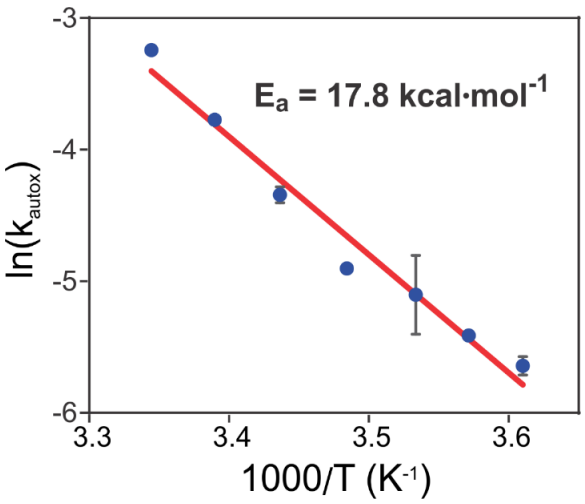

Figure 2.8. Arrhenius plot of the rate constant for eicosanoic-acid bound oxy-OleT decay. The ferrous enzyme was reacted with O_2-saturated buffer and the autoxidation, with maximal absorbance change at 440 nm, was monitored by stopped flow. The rate constant was derived at each temperature by the slowest phase of a summed-three exponential fit.

The possibility of a product-forming pathway involving H_2O_2 as a consequence of autoxidation was further probed by following the formation of the C_{n-1} alkene product. A solution of ferrous EA:OleT was oxygenated and aged several minutes prior to extraction with chloroform and analysis by gas chromatography. Paired reactions included catalase in the reaction mixture as well as the O_2-saturated buffer to ensure efficient H_2O_2-scavenging. Catalase-supplemented reactions resulted in the production of only 0.13 ± 0.02 equivalents of 1-nonadecene per HS-OleT, versus nearly stoichiometric production of the olefin (0.98 ± 0.05 per HS OleT) in catalase-free reaction (Figure 2.10A). This strongly implicates a mechanism involving peroxide, rather than direct reduction of bound O_2, as the pathway utilized by OleT for turnover from dithionite. In order to verify that the H_2O_2 derives from autoxidation of OleT, a set of single turnover reactions were prepared at 4 °C and quenched at various timepoints. The equivalents of 1-nonadecene formed per HS-OleT were plotted as a function of time, and the resulting data was fit to a single exponential function, shown in Figure 2.10B. The fit resulted in a y-intercept of ~0.4 equivalents nonadecene, suggesting a small level of background turnover occurring from a mechanism distinct from autoxidation. This most likely arises from small amounts of H_2O_2 that are formed during preparation of dithionite. Accordingly, this value agrees well with a control reaction containing ferrous-OleT that was directly quenched without the addition of dioxygen, which resulted in 0.37 equivalents of product per HS-OleT. Interestingly, the formation rate of nonadecene formation (0.002 s^{-1}) closely parallels the autoxidation rate of ~0.004 s^{-1}. Together with the substantial quenching that occurs upon the addition of catalase, this strongly implicates a mechanism involving superoxide generation from oxy-OleT followed by more rapid disproportionation to H_2O_2 ($k \sim 10^5$ $M^{-1}s^{-1}$ at neutral pH).[64]

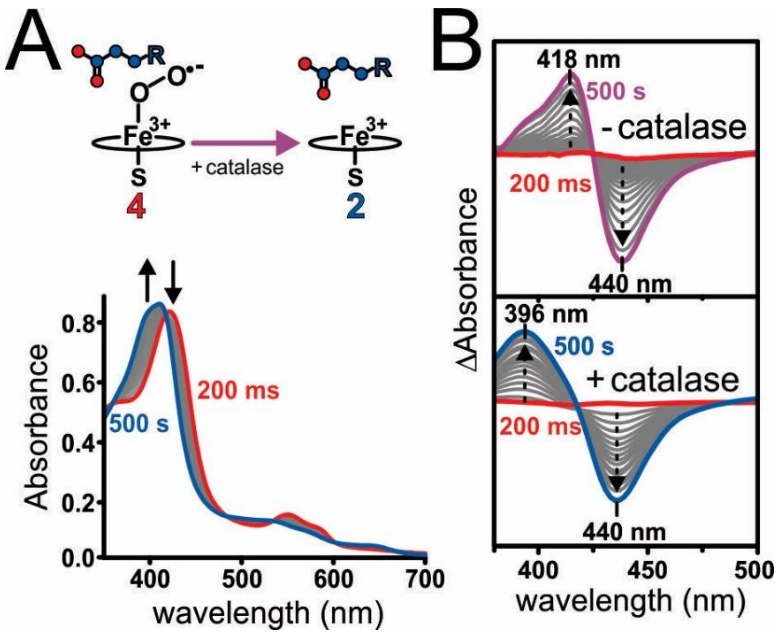

Figure 2.9. OleT autoxidizes to the high-spin form in the presence of catalase. (**A**) Autoxidation of 10 μM oxyOleT in the presence of 2.5 μM catalase (active sites) at 4 °C monitored by stopped flow spectroscopy. The oxy-complex (red spectrum) decays over the course of 500 s to form the high-spin ferric enzyme (blue spectrum). (**B**) Comparison of the difference spectra corresponding to oxyOleT decomposition. The spectrum of oxy-OleT (formed at 200 ms) was used as a baseline and subtracted from spectra at later timepoints.

2.3.4 Activation of Molecular Oxygen – Proton Delivery in OleT

Presupposing that a redox donor can be identified to efficiently reduce oxyOleT to the ferric-peroxoanion intermediate (5), generation of the Compound I oxidant would still entail the orchestrated delivery of protons to the distal oxygen atom for O-O heterolysis. In many ways the most surprising aspect of the successful multiple turnover of OleT from pyridine nucleotide is that CYP152s lack the conserved active site acid-alcohol pair shared by most O_2-dependent CYPs. A vast panoply of work has probed the critical role of these residues for proton delivery to generate Compound I in O_2-dependent CYPs, and we refer

the interested reader to comprehensive reviews on the topic. [65, 66] Briefly summarized, structural, spectroscopic, and turnover studies have revealed that mutation of the acid residue typically results in a slow but coupled enzyme where primary proton delivery to form the hydroperoxo adduct (5) is impaired. In contrast, preservation of the active site alcohol is necessary for delivery of the second proton required for O-O heterolysis to form Compound I and suppress uncoupling to H_2O_2. As the relevant peroxo-intermediates (5 and 6) are highly transient, Hoffman, Davydov and colleagues have found that a very useful method to probe the integrity of proton-donation pathways is to generate them via cryoreduction of the oxy- precursor. [67] In CYPs that utilize Compound I as a direct oxidant, proton transfer is highly efficient and cryoradiolysis of the oxy-complex results in formation of the ferric-hydroperoxo adduct as the primary reduced species at 77 K. [68-70]

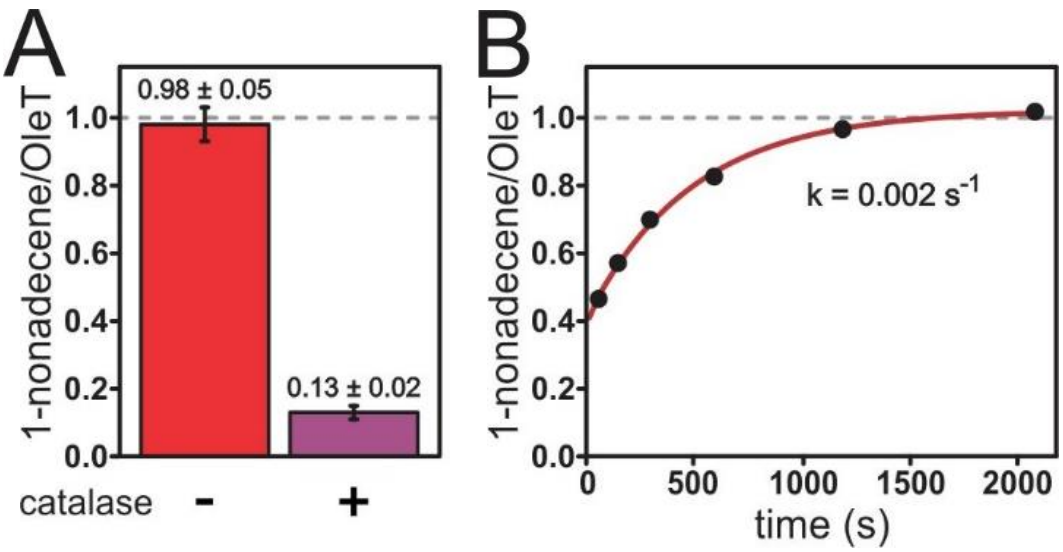

Figure 2.10. Single-turnover experiments of oxyOleT. (**A**) The eicosanoic acid bound OleT-oxy complex (25 µM) was formed and allowed to decay for 35 minutes at 25 °C prior to chloroform extraction and analysis for nonadecene formation. Control reactions included 8 mg/mL catalase. (**B**) Time dependence of nonadecene formation from oxyOleT. OxyOleT was formed at 4 °C and quenched at the indicated time points with HCl and analyzed by gas chromatography to determine the rate for nonadecene formation. The y-intercept (~0.4 equivalents of 1-nonadecene/OleT) is similar to a control reaction where O_2 was omitted.

An EPR spectrum of EA-bound oxy-OleT that was cryoreduced at 77 K and stored for ~ 6 months at liquid N_2 temperature is shown in Figure 2.11. The spectrum shows a major species with g-values at 2.24, 2.15, and 1.90 and a minor contaminant that derives from the ferric low-spin aquo- heme. The low g-anisotropy of the peroxo-adduct is consistent with an assignment as the unprotonated peroxo-anion species (5). For example, very similar EPR spectra are observed in CYPs where the proton delivery network is interrupted through mutagenesis of the conserved acid (e.g. the Asp251Asn mutant of CYP101) or alteration of the immediate hydrogen-bonding environment mediated by active site solvent. [69, 71] Although these coupled but slow CYP101 mutants ultimately form hydroperoxo species at temperatures approaching the glass transition temperature (> 180 K) and ultimately form product, the behavior of cryoreduced oxyOleT differs substantially. As revealed through progressive thermal annealing, the signal corresponding to (5) progressively decays from 180 K to 220 K and does not directly form any species that can be detected. This suggests that the peroxo adduct decays to an intermediate that is either diamagnetic or that has an EPR spectrum that is within the spectral window (g ~ 2) masked by free radicals produced from irradiation. Given the absence of any detectable ferric-hydroperoxo species throughout the annealing process, it is highly unlikely that such a species would represent Compound I. Rather, with analogy to optical annealing experiments of CYP119[72] and horseradish peroxidase (HRP),[73] this more likely reflects a process that involves uncoupling at the peroxo- branchpoint. In these enzymes, the ferric enzyme produced from ligand dissociation is reduced and subsequently binds CO that is formed from the radiolysis of glycerol. Consistent with this, the ferric-LS resting state of OleT was only observed after the sample was fully thawed at 270 K for a prolonged time

and allowed to exchange with oxygen. Taken together, the annealing profile of cryoreduced oxyOleT reflects a combination of the chemical phenotypes associated with absence of both the conserved acid and alcohol in CYP152s, and interruption of both proton transfer steps.

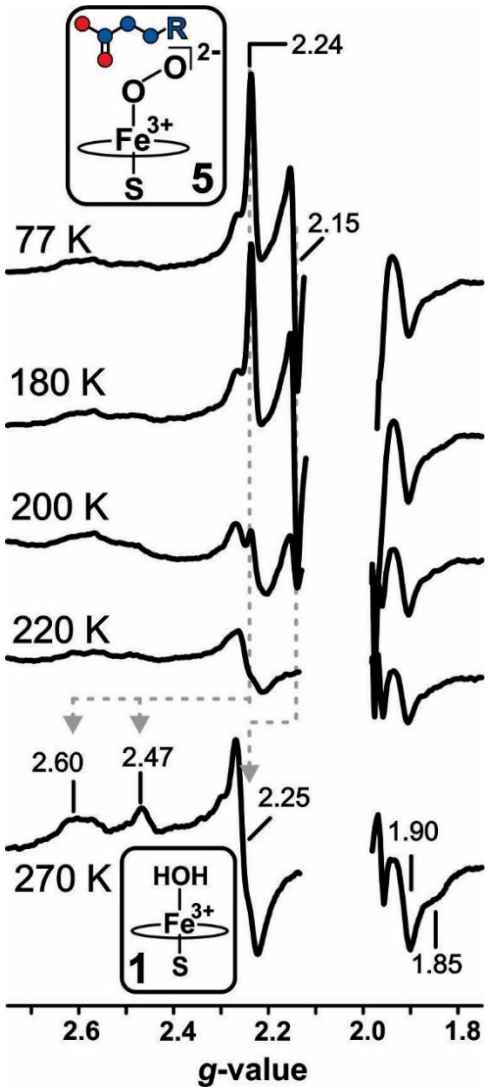

Figure 2.11. Thermal annealing and EPR of the cryo-irradiated OleT oxy-comnplex. X-band EPR spectra of oxy-OleT irradiated by 4 Mrad at 77 K and thermally annealed at the indicated temperatures. The 77 K spectrum was acquired after storage under $N_{2,(l)}$ for 6 months.

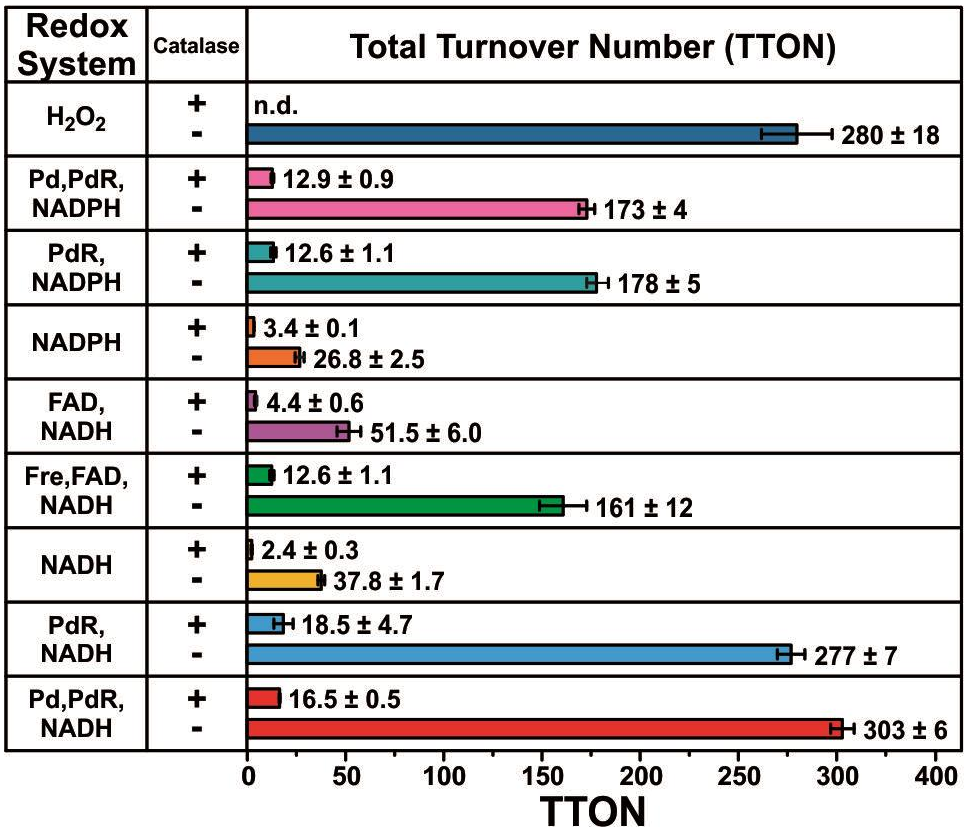

Figure 2.12. Steady state turnover reactions of OleT. Reactions were initiated by the addition of 500 µM H_2O_2 or 500 µM NAD(P)H with the redox chain indicated, and incubated for one hour at room temperature prior to analysis by GC. Solutions contained 1 µM OleT, 500 µM eicosanoic acid and 10 µM of the redox components (Pd, PdR, Fre, and FAD) in the combinations indicated. Reactions with catalase were performed in the presence of 2 µM tetramer. All combinations were tested in triplicate with the mean total turnover number (TTON) and 1 standard deviation of the mean indicated by the error bars.

2.3.5 OleT multiple turnover with NAD(P)H results from H_2O_2 production

Multiple turnover studies were utilized to assess the decarboxylation ability of OleT with the Pd/PdR and Fre/FAD redox systems. The results from steady-state turnover experiments performed in triplicate are shown in Figure 2.12. For experiments using the Pd/PdR couple, reactions that used either NADH or NADPH were analyzed, as the NADPH/Pd/PdR system was previously demonstrated to result in higher alkene yields than

those using NADH.[20] This is surprising given the highly preferential nature of PdR for NADH. Work by Peterson and colleagues has shown that the reduction of PdR by NADPH is 3 orders of magnitude slower than NADH.[74] This suggests that the previously observed OleT activity may have originated from processes independent from electron transfer. Reactions were performed in triplicate in the absence and presence of catalase (≥ 1000 U/mL) over the course of one hour before extraction and analysis by GC. A large amount of catalase was used due to the relatively high-affinity of OleT and the CYP152 hydroxylase BSβ for H_2O_2 ($K_D^{H_2O_2}$~ 50 μM).[17, 22, 24, 75] Likewise, relatively short (1 hour) reaction times were employed in order to prevent the unwanted inactivation of OleT and catalase. The catalase concentrations and reaction conditions used here were able to fully eliminate the activity of OleT when 500 nmol of H_2O_2, equivalent to the amount of pyridine nucleotide used in the turnover studies described below,was slowly added to the enzyme over the course of an hour. In the absence of catalase, the Pd/PdR/NADH system produced 303 ± 6 nmol of alkene product with NADH, and despite the relative inability for PdR to utilize NADPH, 173 ± 4 nmol of nonadecene was still observed when the less preferred pyridine nucleotide was used. The omission of Pd from the presumptive redox chain resulted in a large retention (> 93 %) of activity and reactions that only included NAD(P)H still showed a good degree of decarboxylation (12 – 15 %). Despite the inability of Fre to serve as a CYP effector and unlikelihood that it can deliver the second electron required for O-O bond cleavage, the Fre/FAD/NADH redox system still showed relatively high activity (> 50 %) when compared to the Pd/PdR/NADH couple. The absence of any clear correlation of activity to redox donor properties or components clearly invokes a mechanism distinct from the canonical O_2/e^- cycle for CYPs. Instead, the elimination of ≥

90% of the decarboxylation product by catalase clearly points to H_2O_2, produced as a result of redox cofactor autoxidation, as the major source for OleT activity from pyridine nucleotide.

2.4 CONCLUSIONS

Biological redox chains have proven to be effective for OleT turnover and studies using these systems have elaborated on the catalytic versatility of this enzyme class for decarboxylating a suite of fatty acid substrates. Despite the success of such bioengineering efforts for elucidating and expanding upon the substrate scope of OleT, the results presented in this manuscript serve as a cautionary guide when searching for new redox donors to enhance OleT activity or to adapt this enzyme for *in vivo* biofuel synthesis. The sluggishness of electron transfer and inability for OleT to mediate the proton-dependent cleavage of dioxygen leaves little doubt that the turnover observed in these systems stems from the adventitious production of H_2O_2. This can occur through autoxidation from the oxy-ferrous complex, the redox donor, or the pyridine nucleotide itself[75] (Figure 2.13). As a result, the coupling value (product formed per NADH), commonly used as a metric to gauge the efficiency of the process, is a poor guide as all of these processes could yield stoichiometric product per pyridine nucleotide consumed. In addition to rewiring electron and proton donor pathways, the ability for OleT to efficiently scavenge H_2O_2 could be harnessed for generating biofuels in hosts that are oxidatively challenged through chemical or genetic approaches. The autoxidation shunt pathway revealed in these studies provide an equally intriguing alternative. If the oxy-complex can be sufficiently destabilized, it may be possible to produce H_2O_2 in a manner that is sequestered from ROS scavengers.

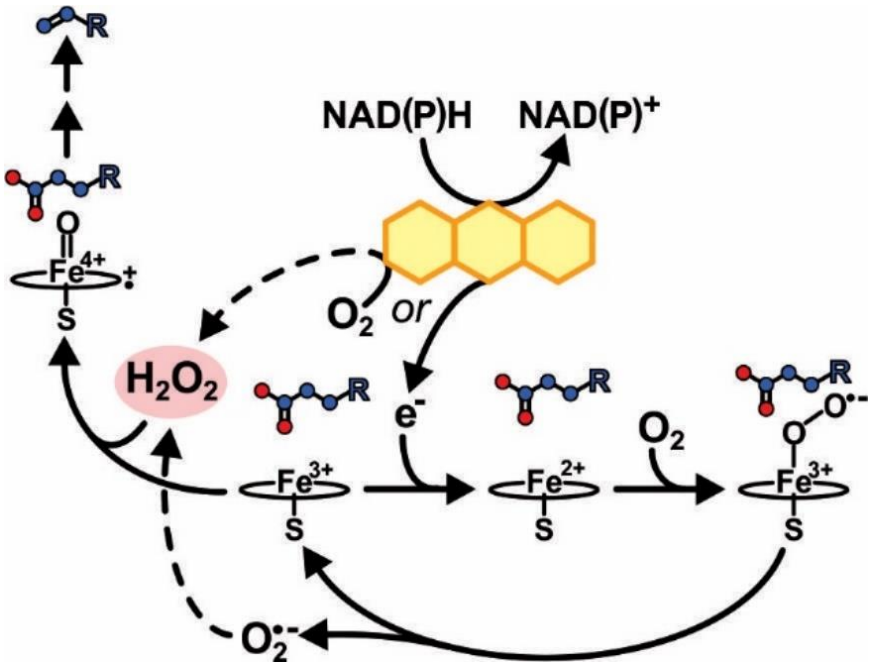

Figure 2.13. Scheme for the generation of H_2O_2 from pyridine nucleotide and OleT. Operant pathways involve the autoxidation of the redox donor (a flavin group is designated) or the OleT-oxy complex to form superoxide, and ultimately H_2O_2.

2.5 MATERIALS AND METHODS

2.5.1 Chemicals and Reagents

All microbiology reagents and media, reduced β-nicotinamide adenine dinucleotide (NADH) and reduced β-nicotinamide adenine dinucleotide phosphate (NADPH) were purchased from Research Products International. Glycerol, buffers, and chloramphenicol (CAM) were from VWR International. Bovine liver catalase (2,000-5,000 units·mg^{-1}), tetracycline, methyl viologen, 30% hydrogen peroxide, and sodium hydrosulfite (dithionite) were from Sigma Aldrich. Antibiotics and isopropyl-β-D-thiogalactopyranoside (IPTG) were from Gold Biotechnology. Hemin was purchased from Carbosynth. Flavin adenine dinucleotide (FAD), 1-hexadecene, and 1-nonadecene gas

chromatography standards were from Tokyo Chemical Industry (TCI) Company. The pChuA plasmid was a gift from Alan Jasanoff (Addgene plasmid # 42539).[76] The pG-Tf2 chaperone plasmid was from Takara Bio Inc. Protiated ($C_{20}H_{40}O_2$) and perdeuterated ($C_{20}D_{40}O_2$) eicosanoic acid were from Supelco Analytical and CDN Isotopes respectively.

2.5.2 Protein Expression and Purification

Heterologous expression and purification of OleT is described in earlier work. [24] The *fre* gene was cloned from genomic DNA prepared from *E. coli* DH5α cells using a Promega Wizard SV Genomic DNA Purification kit. The *fre* gene, which encodes *E. coli* NAD(P)H:flavin oxidoreductase, was amplified and subsequently cloned into a pet21b vector following PCR amplification using the following primers with restriction sites underlined: FreFwd (*Nde*I) 5'-GGATGGCATATGACAACCTTAAGCTGTA-3' and FreRvs (*Xho*I) 5'-GGATGGCTCGAGGATAAATGCAAACGCA-3'. The resulting construct was transformed into *E. coli* BL21(DE3) cells and grown in 2 L flasks containing 1 L of Luria broth (LB) supplemented with 100 mg/L ampicillin and inoculated with 10 mL of an overnight starter culture at 37 °C and 180 rpm. At OD_{600} = 0.7, expression was induced via addition of 250 μM IPTG and the temperature was decreased to 18 °C for 24 hours. Cells were harvested via centrifugation and stored at -70 °C. Fre-containing cells were resuspended in pH 8.0 lysis buffer containing 50 mM NaH_2PO_4, 300 mM NaCl, 10 mM imidazole, and 0.1 % (v/v) Triton-X100. Following sonication and centrifugation, the clarified lysate was loaded onto a Ni-NTA column pre-equilibrated in lysis buffer, then washed in the same buffer containing 20 mM imidazole. Bound protein was eluted with 50 mM NaH_2PO_4, 300 mM NaCl, 250 mM imidazole, and 0.1 % (v/v) Triton X-100 pH 8.0. Fractions containing protein were pooled, and dialyzed overnight against 50 mM NaH_2PO_4

and 300 mM NaCl pH 8.0, then concentrated and stored at -70 °C. Pentahistidine-tagged putidaredoxin reductase and hexahistidine-tagged puridaredoxin were expressed and purified using published procedures.[77, 78]

2.5.3 Ultraviolet-Visible (UV-vis) Spectroscopy

Optical spectra were recorded using an HP 8453 spectrophotometer. The concentration and high-spin content of OleT was determined using ε_{395} = 53 $mM^{-1}cm^{-1}$ and ε_{418} = 110 $mM^{-1}cm^{-1}$ for the low-spin enzyme, ε_{395} = 96 $mM^{-1}cm^{-1}$ and ε_{418} = 52 $mM^{-1}cm^{-1}$ for the high-spin form, and ε_{406} = 81 $mM^{-1}cm^{-1}$ for the isosbestic point between the two species. High-spin, substrate-bound enzyme was prepared by adding 2 molar equivalents of eicosanoic acid (dissolved at a concentration of 10 mM in 10 % Triton X-100: 90 % ethanol (v:v), incubating on ice, and centrifuging to eliminate the unsolubilized fatty acid and aggregated protein. This preparation yielded P450 with a high spin content of approximately 85 – 90 %. When low-spin OleT was required, the as-purified enzyme was treated with 4 equivalents of H_2O_2, incubated for 1 hour, and subsequently desalted on a PD-10 column.

Dithionite solutions were prepared in septa-sealed vials with anaerobic buffer, and concentrations were determined by optical spectroscopy in a sealed anaerobic cuvette prior to use with ε_{315} = 8 mM^{-1} cm^{-1}.[79] NADH and NADPH were quantified aerobically using ε_{340} = 6.2 mM^{-1} cm^{-1}.[80] The concentrations of Pd and PdR were determined using ε_{412} = 11 $mM^{-1}cm^{-1}$ and ε_{454} = 10 mM^{-1} cm^{-1}respectively.[77] The percent of FAD bound to Fre was found to vary between preparations, so in order to accurately quantify Fre (ε_{280} = 27 $mM^{-1}cm^{-1}$ for the apoprotein) it was necessary to subtract the contribution of FAD at 280 nm $\varepsilon_{280, FAD}$ = 20 $mM^{-1}cm^{-1}$ determined using the unique absorption of the cofactor ($\varepsilon_{450, FAD}$ =

11 $mM^{-1}cm^{-1}$). [81] Catalase stocks were prepared fresh daily by dissolving 8 - 20 mg of the lyophilized protein in 1 mL of 50 mM KH_2PO_4 pH 7.5. Solutions were centrifuged and dissolved catalase was quantified based on the heme content for the tetrameric protein using ε_{405} = 324 $mM^{-1}cm^{-1}$. [82]

2.5.4 Transient Kinetics Studies

Stopped flow spectroscopy was performed on an Applied Photophysics SX20 stopped flow with a 1 msec dead-time using a photodiode array (PDA) detector. For anaerobic studies, the instrument was equipped with an anaerobic accessory and scrubbed of oxygen using a 2-5 mM dithionite solution, then rinsed thoroughly with an anaerobic buffer prepared by sparging with N_2 gas. Electron transfer studies were conducted by preparing a carbon monoxide (CO) saturated solution of 10 µM high-spin OleT, 5 µM excess eicosanoic acid, 2.6 µM catalase, and either 100 µM Fre/FAD or 100 µM Pd/PdR. This solution was rapidly mixed with 250 µM NADH, supplemented with 0.8 µM catalase tetramer, which was degassed in the same manner as the protein samples. Spectra were collected and traces at 446 nm were fit to a single exponential equation using Pro-Data SX Software to determine the electron transfer rate.

Oxy-complex formation and decay was performed in a 250 mM KH_2PO_4 pH 7.5, 250 mM NaCl buffer. Buffer was purged with oxygen gas on ice for 2 hours to achieve O_2-saturation (~2 mM O_2 at 4 ^oC). Protein samples contained either 10 µM of a stoichiometric OleT:eicosanoic acid complex or the substrate free enzyme. The protein was sparged with N_2 gas on ice and complete reduction of P450 was acheived by the addition of approximately 50 µM dithionite in the presence of 1 µM methyl viologen. Ferrous P450 was transferred anaerobically to the stopped flow using a gastight syringe, and rapidly

mixed with either an O_2-saturated buffer or a mixture of O_2 and N_2 saturated buffers for the O_2 concentration dependence studies. Formation of the oxy-complex is kinetically well resolved from autoxidation phases, which are much slower. The O_2 on rate was determined through fitting the increase in absorbance at 440 nm over short time (< 1 s) time scales where no appreciable decay occurs to a single exponential expression to determine an observed rate (k_{obs}) for oxyOleT formation. The O_2 on rate is determined by the slope of the k_{obs} versus O_2 concentration plots under pseudo-first order conditions in O_2. Autoxidation rates were determined by fitting the 440 nm time courses to the following three summed exponential equation which is appropriate for a series of first order or pseudo first order reactions. $A_{t,obs}$ is the observed absorbance, 1/t is the reciprocal relaxation time (RRT) of a particular phase (in inverse seconds), a is the amplitude of that phase, t is the time (seconds), and A_∞ is the final absorbance:

$$A_{t,obs} = A_\infty + a_1 e^{-t/t_1} + a_2 e^{-t/t_2} + a_3 e^{-t/t_3}$$

The observed reciprocal relaxation times were kinetically well separated where the fastest phase with a negative amplitude (positive absorbance) represents the observed rate for oxyferrous formation. The two slower phases with positive amplitudes represent the rates of autoxidation which are O_2 independent and hence irreversible in nature. In experiments that probed autoxidation in the presence of catalase, a solution of 20 µM of OleT:eicosanoic acid, 2 µM methyl viologen and 5 µM catalase (active sites) was made anaerobic and reduced as described above. The solution was mixed at 4 ^oC with a KH_2PO_4 solution containing 2 mM O_2.

2.5.5 Product Formation Studies

Single Turnover - Single turnover experiments were performed at 4 °C on ice in 10 mL anaerobic, septum-sealed vials. Initial reaction mixtures (2 mL) contained 25 µM high-spin OleT:$C_{20}D_{40}O_2$ complex and 2.5 µM methyl viologen in 150 mM KH_2PO_4 pH 7.5, and 150 mM NaCl. The protein was sparged with N_2 gas and subsequently reduced via the addition of 5 equivalents of dithionite. Following a 2-3 minute incubation to allow complete reduction, 2 mL of O_2-saturated buffer was added. Reactions were quenched at 1, 2.5, 5, 10, 20, or 35 minutes after O_2 addition via the addition of HCl to a final concentration of ~ 2 M. N_2-saturated buffer was added to the anaerobic control. For reactions where catalase was included, the O_2 solution contained 8 $mg{\cdot}mL^{-1}$ catalase in both the initial reaction mixture and the O_2-saturated buffer. As an internal standard, 50 nmol of 1-hexadecene was added and samples were analyzed by gas chromatography using methods we have reported previously. [24, 30]

Multiple Turnover - Multiple turnover reactions were performed in 75 mM KH_2PO_4 and 75 mM NaCl pH 7.5 at room temperature over a 60 minute time course. Each 1 mL reaction contained 1 µM Ole, 0.5 mM eicosanoic acid, 10 µM redox partner(s), and either 0.5 mM NADH or NADPH. Peroxide control reactions were carried out by slow perfusion of 0.5 mM H_2O_2 via syringe pump over the same time period. All reactions were performed in triplicate and paired with reactions containing 2 µM catalase tetramer, also in triplicate. Due to the photoreactivity of FAD, reactions containing this component were set-up and carried out in the dark. Reactions were quenched and analyzed as described above.

2.5.6 Cryoreduction Studies

A 0.75 mL solution of 200 µM OleT bound to deuterated eicosanoic acid (~80% high-spin content) and 20 µM methyl viologen in 200 mM KH_2PO_4 pH 7.5, 200 mM NaCl, and 20% glycerol was sparged with N_2 on ice in a septum-sealed anaerobic vial. Dithionite from a 40 mM stock was added to achieve a final concentration of 1 mM, and the protein mix was stirred on ice for ~3 minutes to ensure complete reduction. The sample was subsequently transferred to 3 septum-sealed EPR tubes. Samples were chilled in a -15 °C dry ice/ethanol cryobath, and O_2 was gently bubbled into the protein solution for 10 - 20 seconds while quickly lowering and raising the EPR tube in and out of the cryobath to generate the oxy-ferrous intermediate. Septa were removed and the tubes were frozen in liquid nitrogen within 1 minute of oxygen exposure. The OleT oxy complexes were γ-irradiated at 77 K to a total absorbed dose of ~4 Mrad with a ^{60}Co source at the Notre Dame Radiation Laboratory and kept at liquid nitrogen temperatures prior to analysis. Samples were thermally annealed in one minute increments using a liquid nitrogen-cooled ethanol cryobath initially set at ~160 K. Temperatures were increased by 10-20 K increments via titration of cyclohexane into the cryobath, were subsequently annealed at 270 K for 5-10 minutes. For each annealing temperature, EPR spectra were collected using a Bruker X-band EMXplus equipped with an Oxford Instruments ESR continuous flow liquid helium cryostat at 20 K using a microwave power of 2 mW and a modulation amplitude of 10 gauss. Samples were maintained at 77 K between annealing and transfer to the EPR cavity. Following annealing, samples were thawed, extracted in chloroform, then analyzed for 1-nonadecene formation by GC.

2.6 ACKNOWLEDGMENTS

This work was supported by National Science Foundation CAREER Grant 1555066 and grants from the University of South Carolina Vice President of Research to T.M.M. through the ASPIRE I and II programs. We thank Prof. James Kincaid and Yilin Liu (Marquette University) and Dr. Jay A. LaVerne at Notre Dame Radiation Laboratory (Notre Dame University, IN), a facility of the US Department of Energy, Office of Basic Energy Science, for their assistance in cryoreduction experiments.

2.7 REFERENCES

1. Wise, C. E.; Grant, J. L.; Amaya, J. A.; Ratigan, S. C.; Hsieh, C. H.; Manley, O. M.; Makris, T. M., Divergent mechanisms of iron-containing enzymes for hydrocarbon biosynthesis. *J Biol Inorg Chem* **2017,** *22* (2-3), 221-235.
2. Qiu, Y.; Tittiger, C.; Wicker-Thomas, C.; Le Goff, G.; Young, S.; Wajnberg, E.; Fricaux, T.; Taquet, N.; Blomquist, G. J.; Feyereisen, R., An insect-specific P450 oxidative decarbonylase for cuticular hydrocarbon biosynthesis. *Proc Natl Acad Sci USA* **2012,** *109* (37), 14858-14863.
3. Schirmer, A.; Rude, M. A.; Li, X.; Popova, E.; del Cardayre, S. B., Microbial biosynthesis of alkanes. *Science* **2010,** *329* (5991), 559-62.
4. Rude, M. A.; Baron, T. S.; Brubaker, S.; Alibhai, M.; Del Cardayre, S. B.; Schirmer, A., Terminal Olefin (1-Alkene) Biosynthesis by a Novel P450 Fatty Acid Decarboxylase from Jeotgalicoccus Species. *Appl Environ Microb* **2011,** *77* (5), 1718-1727.
5. Rui, Z.; Harris, N. C.; Zhu, X. J.; Huang, W.; Zhang, W. J., Discovery of a Family of Desaturase-Like Enzymes for 1-Alkene Biosynthesis. *ACS Catal* **2015,** *5* (12), 7091-7094.
6. Rui, Z.; Li, X.; Zhu, X. J.; Liu, J.; Domigan, B.; Barr, I.; Cate, J. H. D.; Zhang, W. J., Microbial biosynthesis of medium-chain 1-alkenes by a nonheme iron oxidase. *Proc Natl Acad Sci USA* **2014,** *111* (51), 18237-18242.
7. Choi, Y. J.; Lee, S. Y., Microbial production of short-chain alkanes. *Nature* **2013,** *502* (7472), 571-4.

8. Kallio, P.; Pasztor, A.; Thiel, K.; Akhtar, M. K.; Jones, P. R., An engineered pathway for the biosynthesis of renewable propane. *Nat Commun* **2014,** *5*, 4731.
9. Buijs, N. A.; Zhou, Y. J.; Siewers, V.; Nielsen, J., Long-chain alkane production by the yeast Saccharomyces cerevisiae. *Biotechnol Bioeng* **2015,** *112* (6), 1275-9.
10. Zhou, Y. J.; Buijs, N. A.; Zhu, Z.; Qin, J.; Siewers, V.; Nielsen, J., Production of fatty acid-derived oleochemicals and biofuels by synthetic yeast cell factories. *Nat Commun* **2016,** *7*, 11709.
11. Rajakovich, L. J.; Norgaard, H.; Warui, D. M.; Chang, W. C.; Li, N.; Booker, S. J.; Krebs, C.; Bollinger, J. M.; Pandelia, M. E., Rapid Reduction of the Diferric-Peroxyhemiacetal Intermediate in Aldehyde-Deformylating Oxygenase by a Cyanobacterial Ferredoxin: Evidence for a Free-Radical Mechanism. *J Am Chem Soc* **2015,** *137* (36), 11695-11709.
12. Warui, D. M.; Li, N.; Norgaard, H.; Krebs, C.; Bollinger, J. M.; Booker, S. J., Detection of Formate, Rather than Carbon Monoxide, As the Stoichiometric Coproduct in Conversion of Fatty Aldehydes to Alkanes by a Cyanobacterial Aldehyde Decarbonylase. *J Am Chem Soc* **2011,** *133* (10), 3316-3319.
13. Zhang, J. J.; Lu, X. F.; Li, J. J., Conversion of fatty aldehydes into alk (a/e)nes by in vitro reconstituted cyanobacterial aldehyde-deformylating oxygenase with the cognate electron transfer system. *Biotechnol Biofuels* **2013,** *6*.
14. Aukema, K. G.; Makris, T. M.; Stoian, S. A.; Richman, J. E.; Munck, E.; Lipscomb, J. D.; Wackett, L. P., Cyanobacterial aldehyde deformylase oxygenation of aldehydes yields n-1 aldehydes and alcohols in addition to alkanes. *ACS Catal* **2013,** *3* (10), 2228-2238.

15. Patrikainen, P.; Carbonell, V.; Thiel, K.; Aro, E. M.; Kallio, P., Comparison of orthologous cyanobacterial aldehyde deformylating oxygenases in the production of volatile C3-C7 alkanes in engineered E. coli. *Metab Eng Commun* **2017,** *5*, 9-18.
16. Grant, J. L.; Hsieh, C. H.; Makris, T. M., Decarboxylation of fatty acids to terminal alkenes by cytochrome P450 compound I. *J Am Chem Soc* **2015,** *137* (15), 4940-3.
17. Grant, J. L.; Mitchell, M. E.; Makris, T. M., Catalytic strategy for carbon-carbon bond scission by the cytochrome P450 OleT. *Proc Natl Acad Sci USA* **2016,** *113* (36), 10049-10054.
18. Lu, X.; Vora, H.; Khosla, C., Overproduction of free fatty acids in E. coli: implications for biodiesel production. *Metab Eng* **2008,** *10* (6), 333-9.
19. Xu, P.; Gu, Q.; Wang, W.; Wong, L.; Bower, A. G.; Collins, C. H.; Koffas, M. A., Modular optimization of multi-gene pathways for fatty acids production in E. coli. *Nat Commun* **2013,** *4*, 1409.
20. Dennig, A.; Kuhn, M.; Tassoti, S.; Thiessenhusen, A.; Gilch, S.; Bulter, T.; Haas, T.; Hall, M.; Faber, K., Oxidative Decarboxylation of Short-Chain Fatty Acids to 1-Alkenes. *Angew Chem Int Ed Engl* **2015,** *54* (30), 8819-8822.
21. Dennig, A.; Kurakin, S.; Kuhn, M.; Dordic, A.; Hall, M.; Faber, K., Enzymatic Oxidative Tandem Decarboxylation of Dioic Acids to Terminal Dienes. *Eur J Org Chem* **2016,** (21), 3473-3477.
22. Hsieh, C. H.; Huang, X.; Amaya, J. A.; Rutland, C. D.; Keys, C. L.; Groves, J. T.; Austin, R. N.; Makris, T. M., The Enigmatic P450 Decarboxylase OleT Is Capable of, but Evolved To Frustrate, Oxygen Rebound Chemistry. *Biochemistry* **2017,** *56* (26), 3347-3357.

23. Wang, J. B.; Lonsdale, R.; Reetz, M. T., Exploring substrate scope and stereoselectivity of P450 peroxygenase OleTJE in olefin-forming oxidative decarboxylation. *Chem Commun (Camb)* **2016,** *52* (52), 8131-3.

24. Amaya, J. A.; Rutland, C. D.; Leschinsky, N.; Makris, T. M., A Distal Loop Controls Product Release and Chemo- and Regioselectivity in Cytochrome P450 Decarboxylases. *Biochemistry* **2018,** *57* (3), 344-353.

25. Joo, H.; Lin, Z.; Arnold, F. H., Laboratory evolution of peroxide-mediated cytochrome P450 hydroxylation. *Nature* **1999,** *399* (6737), 670-3.

26. Kumar, S.; Liu, H.; Halpert, J. R., Engineering of cytochrome P450 3A4 for enhanced peroxide-mediated substrate oxidation using directed evolution and site-directed mutagenesis. *Drug Metab Dispos* **2006,** *34* (12), 1958-65.

27. Matthews, S.; Tee, K. L.; Rattray, N. J.; McLean, K. J.; Leys, D.; Parker, D. A.; Blankley, R. T.; Munro, A. W., Production of alkenes and novel secondary products by P450 OleT(JE) using novel H2O2-generating fusion protein systems. *FEBS Lett* **2017,** *591* (5), 737-750.

28. Zachos, I.; Gassmeyer, S. K.; Bauer, D.; Sieber, V.; Hollmann, F.; Kourist, R., Photobiocatalytic decarboxylation for olefin synthesis. *Chem Commun (Camb)* **2015,** *51* (10), 1918-21.

29. Bojarra, S.; Reichert, D.; Grote, M.; Baraibar, A. G.; Dennig, A.; Nidetzky, B.; Mugge, C.; Kourist, R., Bio-based ,-Functionalized Hydrocarbons from Multi-step Reaction Sequences with Bio- and Metallo-catalysts Based on the Fatty Acid Decarboxylase OleT(JE). *ChemCatChem* **2018,** *10* (5), 1192-1201.

30. Amaya, J. A.; Rutland, C. D.; Makris, T. M., Mixed regiospecificity compromises alkene synthesis by a cytochrome P450 peroxygenase from Methylobacterium populi. *J Inorg Biochem* **2016,** *158*, 11-16.
31. Fang, B.; Xu, H. F.; Liu, Y.; Qi, F. X.; Zhang, W.; Chen, H.; Wang, C.; Wang, Y. L.; Yang, W. X.; Li, S. Y., Mutagenesis and redox partners analysis of the P450 fatty acid decarboxylase OleT(JE). *Sci Rep* **2017,** *7*.
32. Liu, Y.; Wang, C.; Yan, J. Y.; Zhang, W.; Guan, W. N.; Lu, X. F.; Li, S. Y., Hydrogen peroxide-independent production of alpha-alkenes by OleT(JE) P450 fatty acid decarboxylase. *Biotechnol Biofuels* **2014,** *7*.
33. Lu, C.; Shen, F.; Wang, S.; Wang, Y.; Liu, J.; Bai, W.-J.; Wang, X., An Engineered Self-Sufficient Biocatalyst Enables Scalable Production of Linear α-Olefins from Carboxylic Acids. *ACS Catal* **2018**, 5794-5798.
34. Xu, H.; Ning, L.; Yang, W.; Fang, B.; Wang, C.; Wang, Y.; Xu, J.; Collin, S.; Laeuffer, F.; Fourage, L.; Li, S., In vitro oxidative decarboxylation of free fatty acids to terminal alkenes by two new P450 peroxygenases. *Biotechnol Biofuels* **2017,** *10*, 208.
35. Girhard, M.; Schuster, S.; Dietrich, M.; Durre, P.; Urlacher, V. B., Cytochrome P450 monooxygenase from Clostridium acetobutylicum: a new alpha-fatty acid hydroxylase. *Biochem Biophys Res Commun* **2007,** *362* (1), 114-9.
36. Liu, Y.; Wang, C.; Yan, J.; Zhang, W.; Guan, W.; Lu, X.; Li, S., Hydrogen peroxide-independent production of alpha-alkenes by OleTJE P450 fatty acid decarboxylase. *Biotechnol Biofuels* **2014,** *7* (1), 28.

37. Li, S.; Podust, L. M.; Sherman, D. H., Engineering and analysis of a self-sufficient biosynthetic cytochrome P450 PikC fused to the RhFRED reductase domain. *J Am Chem Soc* **2007,** *129* (43), 12940-1.
38. Katagiri, M.; Ganguli, B. N.; Gunsalus, I. C., A Soluble Cytochrome P-450 Functional in Methylene Hydroxylation. *J Biol Chem* **1968,** *243* (12), 3543-&.
39. Chen, B.; Lee, D. Y.; Chang, M. W., Combinatorial metabolic engineering of Saccharomyces cerevisiae for terminal alkene production. *Metab Eng* **2015,** *31*, 53-61.
40. Belcher, J.; McLean, K. J.; Matthews, S.; Woodward, L. S.; Fisher, K.; Rigby, S. E. J.; Nelson, D. R.; Potts, D.; Baynham, M. T.; Parker, D. A.; Leys, D.; Munro, A. W., Structure and Biochemical Properties of the Alkene Producing Cytochrome P450 OleTJE (CYP152L1) from the Jeotgalicoccus sp 8456 Bacterium. *J Biol Chem* **2014,** *289* (10), 6535-6550.
41. Wilson, G. S.; Tsibris, J. C.; Gunsalus, I. C., Electrochemical studies of putidaredoxin and its selenium analog. *J Biol Chem* **1973,** *248* (17), 6059-61.
42. Tripathi, S.; Li, H. Y.; Poulos, T. L., Structural Basis for Effector Control and Redox Partner Recognition in Cytochrome P450. *Science* **2013,** *340* (6137), 1227-1230.
43. Shimada, H.; Nagano, S.; Hori, H.; Ishimura, Y., Putidaredoxin-cytochrome P450cam interaction. *J Inorg Biochem* **2001,** *83* (4), 255-260.
44. Unno, M.; Shimada, H.; Toba, Y.; Makino, R.; Ishimura, Y., Role of Arg112 of cytochrome p450cam in the electron transfer from reduced putidaredoxin. Analyses with site-directed mutants. *J Biol Chem* **1996,** *271* (30), 17869-74.

45. Davies, M. D.; Sligar, S. G., Genetic variants in the putidaredoxin-cytochrome P-450cam electron-transfer complex: identification of the residue responsible for redox-state-dependent conformers. *Biochemistry* **1992,** *31* (46), 11383-9.
46. Guengerich, F. P.; Johnson, W. W., Kinetics of ferric cytochrome P450 reduction by NADPH-cytochrome P450 reductase: rapid reduction in the absence of substrate and variations among cytochrome P450 systems. *Biochemistry* **1997,** *36* (48), 14741-50.
47. Ost, T. W.; Clark, J.; Mowat, C. G.; Miles, C. S.; Walkinshaw, M. D.; Reid, G. A.; Chapman, S. K.; Daff, S., Oxygen activation and electron transfer in flavocytochrome P450 BM3. *J Am Chem Soc* **2003,** *125* (49), 15010-20.
48. Uhlmann, H.; Bernhardt, R., The role of threonine 54 in adrenodoxin for the properties of its iron-sulfur cluster and its electron transfer function. *J Biol Chem* **1995,** *270* (50), 29959-66.
49. Fontecave, M.; Eliasson, R.; Reichard, P., NAD(P)H:flavin oxidoreductase of Escherichia coli. A ferric iron reductase participating in the generation of the free radical of ribonucleotide reductase. *J Biol Chem* **1987,** *262* (25), 12325-31.
50. Gray, K. A.; Pogrebinsky, O. S.; Mrachko, G. T.; Xi, L.; Monticello, D. J.; Squires, C. H., Molecular mechanisms of biocatalytic desulfurization of fossil fuels. *Nat Biotechnol* **1996,** *14* (13), 1705-9.
51. Niviere, V.; Vanoni, M. A.; Zanetti, G.; Fontecave, M., Reaction of the NAD(P)H:flavin oxidoreductase from Escherichia coli with NADPH and riboflavin: identification of intermediates. *Biochemistry* **1998,** *37* (34), 11879-87.

52. Lipscomb, J. D.; Sligar, S. G.; Namtvedt, M. J.; Gunsalus, I. C., Autooxidation and Hydroxylation Reactions of Oxygenated Cytochrome P-450cam. *J Biol Chem* **1976,** *251* (4), 1116-1124.

53. Denisov, I. G.; Grinkova, Y. V.; Baas, B. J.; Sligar, S. G., The ferrous-dioxygen intermediate in human cytochrome P450 3A4 - Substrate dependence of formation and decay kinetics. *J Biol Chem* **2006,** *281* (33), 23313-23318.

54. Peterson, J. A.; Ishimura, Y.; Griffin, B. W., Pseudomonas putida cytochrome P-450: characterization of an oxygenated form of the hemoprotein. *Arch Biochem Biophys* **1972,** *149* (1), 197-208.

55. Wise, C. E.; Makris, T. M., Recruitment and Regulation of the Non-ribosomal Peptide Synthetase Modifying Cytochrome P450 Involved in Nikkomycin Biosynthesis. *ACS Chem Biol* **2017,** *12* (5), 1316-1326.

56. Sono, M.; Eble, K. S.; Dawson, J. H.; Hager, L. P., Preparation and properties of ferrous chloroperoxidase complexes with dioxygen, nitric oxide, and an alkyl isocyanide. Spectroscopic dissimilarities between the oxygenated forms of chloroperoxidase and cytochrome P-450. *J Biol Chem* **1985,** *260* (29), 15530-5.

57. Abu-Soud, H. M.; Gachhui, R.; Raushel, F. M.; Stuehr, D. J., The ferrous-dioxy complex of neuronal nitric oxide synthase. Divergent effects of L-arginine and tetrahydrobiopterin on its stability. *J Biol Chem* **1997,** *272* (28), 17349-53.

58. Bec, N.; Gorren, A. C.; Voelker, C.; Mayer, B.; Lange, R., Reaction of neuronal nitric-oxide synthase with oxygen at low temperature. Evidence for reductive activation of the oxy-ferrous complex by tetrahydrobiopterin. *J Biol Chem* **1998,** *273* (22), 13502-8.

59. Marchal, S.; Gorren, A. C.; Sorlie, M.; Andersson, K. K.; Mayer, B.; Lange, R., Evidence of two distinct oxygen complexes of reduced endothelial nitric oxide synthase. *J Biol Chem* **2004,** *279* (19), 19824-31.

60. Bui, S. H.; McLean, K. J.; Cheesman, M. R.; Bradley, J. M.; Rigby, S. E.; Levy, C. W.; Leys, D.; Munro, A. W., Unusual spectroscopic and ligand binding properties of the cytochrome P450-flavodoxin fusion enzyme XplA. *J Biol Chem* **2012,** *287* (23), 19699-714.

61. Kashem, M. A.; Dunford, H. B., The formation and decay of the oxyferrous complex of beef adrenocortical cytochrome P-450scc. Rapid-scan and stopped-flow studies. *Biochem Cell Biol* **1987,** *65* (5), 486-92.

62. Zhang, H.; Gruenke, L.; Arscott, D.; Shen, A.; Kasper, C.; Harris, D. L.; Glavanovich, M.; Johnson, R.; Waskell, L., Determination of the rate of reduction of oxyferrous cytochrome P450 2B4 by 5-deazariboflavin adenine dinucleotide T491V cytochrome P450 reductase. *Biochemistry* **2003,** *42* (40), 11594-603.

63. Brewer, C. B.; Peterson, J. A., Single turnover kinetics of the reaction between oxycytochrome P-450cam and reduced putidaredoxin. *J Biol Chem* **1988,** *263* (2), 791-8.

64. Bielski, B. H. J.; Allen, A. O., Mechanism of Disproportionation of Superoxide Radicals. *J Phys Chem A* **1977,** *81* (11), 1048-1050.

65. Denisov, I. G.; Makris, T. M.; Sligar, S. G.; Schlichting, I., Structure and chemistry of cytochrome P450. *Chem Rev* **2005,** *105* (6), 2253-77.

66. Poulos, T. L.; Madrona, Y., Oxygen activation and redox partner binding in cytochromes P450. *Biotechnol Appl Biochem* **2013,** *60* (1), 128-33.

67. Davydov, R.; Hoffman, B. M., Active intermediates in heme monooxygenase reactions as revealed by cryoreduction/annealing, EPR/ENDOR studies. *Arch Biochem Biophys* **2011,** *507* (1), 36-43.

68. Davydov, R.; Macdonald, I. D. G.; Makris, T. M.; Sligar, S. G.; Hoffman, B. M., EPR and ENDOR of catalytic intermediates in cryoreduced native and mutant oxy-cytochromes P450cam: Mutation-induced changes in the proton delivery system. *J Am Chem Soc* **1999,** *121* (45), 10654-10655.

69. Davydov, R.; Makris, T. M.; Kofman, V.; Werst, D. E.; Sligar, S. G.; Hoffman, B. M., Hydroxylation of camphor by reduced oxy-cytochrome P450cam: mechanistic implications of EPR and ENDOR studies of catalytic intermediates in native and mutant enzymes. *J Am Chem Soc* **2001,** *123* (7), 1403-15.

70. Denisov, I. G.; Makris, T. M.; Sligar, S. G., Cryotrapped reaction intermediates of cytochrome p450 studied by radiolytic reduction with phosphorus-32. *J Biol Chem* **2001,** *276* (15), 11648-52.

71. Makris, T. M.; von Koenig, K.; Schlichting, I.; Sligar, S. G., Alteration of P450 distal pocket solvent leads to impaired proton delivery and changes in heme geometry. *Biochemistry* **2007,** *46* (49), 14129-40.

72. Denisov, I. G.; Hung, S. C.; Weiss, K. E.; McLean, M. A.; Shiro, Y.; Park, S. Y.; Champion, P. M.; Sligar, S. G., Characterization of the oxygenated intermediate of the thermophilic cytochrome P450 CYP119. *J Inorg Biochem* **2001,** *87* (4), 215-26.

73. Denisov, I. G.; Makris, T. M.; Sligar, S. G., Formation and decay of hydroperoxo-ferric heme complex in horseradish peroxidase studied by cryoradiolysis. *J Biol Chem* **2002,** *277* (45), 42706-10.

74. Roome, P. W.; Peterson, J. A., The Reduction of Putidaredoxin Reductase by Reduced Pyridine-Nucleotides. *Arch Biochem Biophys* **1988,** *266* (1), 32-40.

75. Matsunaga, I.; Yamada, M.; Kusunose, E.; Nishiuchi, Y.; Yano, I.; Ichihara, K., Direct involvement of hydrogen peroxide in bacterial alpha-hydroxylation of fatty acid. *FEBS Lett* **1996,** *386* (2-3), 252-4.

76. Lelyveld, V. S.; Brustad, E.; Arnold, F. H.; Jasanoff, A., Metal-Substituted Protein MRI Contrast Agents Engineered for Enhanced Relaxivity and Ligand Sensitivity. *J Am Chem Soc* **2011,** *133* (4), 649-651.

77. Sevrioukova, I. F.; Hazzard, J. T.; Tollin, G.; Poulos, T. L., Laser flash induced electron transfer in P450cam monooxygenase: Putidaredoxin reductase-putidaredoxin interaction. *Biochemistry* **2001,** *40* (35), 10592-10600.

78. Sevrioukova, I. F.; Garcia, C.; Li, H. Y.; Bhaskar, B.; Poulos, T. L., Crystal structure of putidaredoxin, the [2Fe-2S] component of the P450cam monooxygenase system from Pseudomonas putida. *J Mol Biol* **2003,** *333* (2), 377-392.

79. Yousafzai, F. K.; Eady, R. R., Dithionite reduction kinetics of the dissimilatory coppercontaining nitrite reductase of Alcalegenes xylosoxidans - The SO2 radical binds to the substrate binding type 2 copper site before the type 2 copper is reduced. *J Biol Chem* **2002,** *277* (37), 34067-34073.

80. Bergmeyer, H. U., *Methods of Enzymatic Enalysis*. Verlag Chemie: Weinheim, 1974.

81. Chapman, S. K.; Reid, G. A., *Flavoprotein Protocols*. Humana Press: Totowa, N.J., 1999.

82. Haber, J.; Maslakiewicz, P.; Rodakiewicznowak, J.; Walde, P., Activity and Spectroscopic Properties of Bovine Liver Catalase in Sodium Bis(2-Ethylhexyl)Sulfosuccinate Isooctane Reverse Micelles. *Eur J Biochem* **1993,** *217* (2), 567-573.

CHAPTER 3

Recruitment and Regulation of the Non-Ribosomal Peptide Synthetase Modifying Cytochrome P450 Involved in Nikkomycin Biosynthesis[1]

[1] Reprinted with Permission from: Wise, C. E. and Makris, T. M. Recruitment and Regulation of the Non-ribosomal Peptide Synthetase Modifying Cytochrome P450 Involved in Nikkomycin Biosynthesis. *ACS Chemical Biology* **2017**, *12* (5), 1316-1326. Copyright 2017 American Chemical Society.

3.1 ABSTRACT

The beta-hydroxylation of L-histidine is the first step in the biosynthesis of the imidazolone base of the antifungal drug nikkomycin. The cytochrome P450 (NikQ) hydroxylates the amino acid while it is appended via a phosphopantetheine linker to the non-ribosomal peptide synthetase (NRPS) NikP1. The latter enzyme is comprised of an MbtH, and single adenylation and thiolation domains, a minimal composition that allows for detailed binding and kinetics studies using an intact and homogeneous NRPS substrate. Electron paramagnetic resonance studies confirm that a stable complex is formed with NikQ with NikP1 when the amino acid is tethered. Size exclusion chromatography is used to further refine the principal components that are required for this interaction. NikQ binds NikP1 in the fully charged state, but binding also occurs when NikP1 is lacking both the phosphopantetheine arm and appended amino acid. This demonstrates that the interaction is mainly guided by presentation of the thiolation domain interface, rather than the attached amino acid. Electrochemistry and transient kinetics have been used to probe the influence of L-His-NikP1 binding on catalysis by NikQ. Unlike many P450s, the binding of substrate fails to induce significant changes on the redox potential and autoxidation properties of NikQ, and slows down the binding of dioxygen to the ferrous enzyme to initiate catalysis. Collectively, these studies demonstrate a complex interplay between the NRPS maturation process and the recruitment and regulation of an auxiliary tailoring enzyme required for natural product biosynthesis.

3.2 INTRODUCTION

Nonribosomal peptides (NRPs) often contain amino acids with moieties that are not found in translationally-synthesized proteins. This expanded chemical diversity can impart potent and medicinally-important biological activities that include functions as antibiotics, siderophores, anti-cancer therapeutics, and immunosuppressants, among others.[1-3] Construction of these intricate chemical architectures is accomplished by the tandem role of non-ribosomal peptide synthetases (NRPS) and in some cases, accessory tailoring enzymes that interact with the NRPS at various stages of peptide assembly. The NRPS machinery, highly variable in terms of complexity and domain composition, is principally comprised of repeating modules that include a domain for amino acid adenylation (A), a thiolation (T) domain (also referred to as a peptidyl carrier protein, or PCP) which serves as a scaffold for the growing peptide, and a condensation domain (C) which catalyzes amide bond formation between adjacent modules.[2, 4] The thiolation domain can then exist in three distinct post-translationally modified states during antibiotic assembly: an unmodified *apo* form, one in which a conserved serine on the T-domain is phosphopantetheinylated (termed *holo*), or an aminoacylated (*aa*) form in which an amino acid or peptide is appended to the phosphopantetheine (ppant).[2] Non-proteinogenic amino acids are incorporated into the growing peptide as a result of their biosynthesis and subsequent activation by the A domain, modifications in *cis* by specialized NRPS modules, or in *trans* by accessory enzymes that are distinct from the NRPS machinery. In this latter approach, an amino acid is tailored during the chain elongation process while it is appended to the T-domain via a thioester linkage to a phosphopantetheine arm.[5-6]

The principle molecular determinants which govern tailoring enzyme specificity have yet to be fully clarified despite a central importance in the biosynthesis pathways of many bacterial virulence factors and clinically deployed pharmaceuticals. Elucidating the basis for NRPS interactions with *trans*-acting proteins may prove invaluable for engineering catalysts to act on non-native substrates and allow for the targeted production of new natural products with enhanced pharmacological properties or the synthesis of diverse libraries of compounds. For example, the demonstrated highly selective nature of some tailoring enzymes, combined with the modular nature of the NRPS assembly process, enables a specific amino acid, and even a single C-H bond in a very complex polypeptide, to be selectively modified. Though highly sought-after, this feat is extraordinarily difficult to achieve through late stage functionalization strategies after the peptide is assembled.

One major limitation for understanding the basis of NRPS:tailoring enzyme interactions stems from challenges with obtaining these complex substrates in suitably large quantities and in a homogeneous form. For instance, NRPS-linked substrates can sometimes consist of a complex polypeptide appended to an extremely large synthetase composed of several modules. A particularly relevant example includes the extensive and well-ordered P450-catalyzed oxidative cross coupling reactions involved in the maturation of glycopeptide (GPA) antibiotics such as vancomycin.[7-9] To circumvent some of the limitations in working with these complex substrates, one common approach for interrogating the binding of accessory enzymes with NRPS-linked substrates has been the excision of a single module, often as the minimal ~10 kDa T-domain. This strategy has been utilized for the reconstitution of activity of many newly-discovered NRPS-modifying enzymes,[9-13] and in some cases, has permitted more detailed binding and structural

studies[13-15] to gauge the individual contributions of T-domain surface, ppant arm, and tethered amino acid on molecular recognition. Studies using isolated peptidyl carrier proteins, as native stand-alone proteins or excised from larger NRPS modules, have collectively that both the NRPS-tailoring enzyme interface and identity of the tethered amino acid can guide these interactions and be used to trigger catalysis.[13, 15-16]

The omission of additional NRPS subunits may undervalue potential contributions of neighboring domains or linker regions on the molecular recognition of auxiliary proteins. For the GPA antibiotics, elegant studies by the Cryle laboratory have shown that a specialized module, known as the X-domain, mediates the correct recruitment and ensuing catalysis of enzymes involved in peptide crosslinking.[17-19] However, this module is highly-specific to GPAs and is not present in many NRP biosynthetic pathways that contain tailoring enzymes. An additional layer of complexity arises from the extraordinary conformational flexibility of the NRPS in different charged states. Structural studies of individual A and T domains,[20-23] complexes obtained from mechanism-based inhibitors,[24-25] and recent comparative x-ray crystal structures of AT modules,[26-27] have illustrated that the NRPS is highly dynamic and can adopt several different architectures during peptide assembly. It is not known whether these substantial structural changes influence the presentation of aminoacyl substrates, or the T domain surface, and gate the binding of enzymes for efficient tailoring to occur.

In order to examine how the NRPS coordinates the binding of auxiliary proteins, we sought a relatively simple NRPS and cognate tailoring enzyme pair that would allow for finite control of the NRPS post-translational state and enable detailed spectroscopic and kinetic studies. A system meeting these criteria is provided within the nikkomycin

biosynthetic gene cluster of *Streptomyces tendae* that produces a first-in-class antifungal drug that inhibits cell wall synthesis.[10] The pathway consists of a relatively simple ~70 kDa NRPS (NikP1) that is composed of a single AT module flanked by an N-terminal MbtH-like domain thought to be important for efficient adenylation and for ensuring NRPS folding and solubility *in vitro*.[28-31] Following the activation and tethering of L-histidine, a cytochrome P450 (NikQ) hydroxylates the T-appended amino acid at the beta-position.[10] The regio-specific Cβ-hydroxylation of T-domain-linked amino acids is a common modification found in many natural product biosynthetic pathways and is catalyzed by several classes of iron-containing enzymes including several cytochrome P450s, the non-heme carboxylate-bridged dinuclear iron enzyme CmlA involved in chloramphenicol biosynthesis,[32-33] and a number of Fe^{2+} and α-ketoglutarate-dependent enzymes (e.g. KtzP from the kutzneride pathway).[12, 34-35] In nikkomycin biosynthesis, following hydroxylation by NikQ, a thioesterase (NikP2) releases β-hydroxyhistidine from the NikP1, shown in Figure 3.1.[10] Downstream processing results in the formation of an imidazolone base that can have diverse pharmacological properties.

We have examined the interaction of NikQ with NikP1 at different stages of the NRPS maturation process. Unlike many P450s that undergo a spin-state conversion upon substrate binding, aminoacylated L-His-NikP1 fails to induce appreciable changes to the optical absorption spectrum of NikQ. However, changes in the electron paramagnetic resonance (EPR) spectrum of NikQ upon substrate binding reveal that a stable complex is formed. Analytical size exclusion chromatography (SEC) studies have been used to further probe the nature of the protein interface and identify the NRPS elements that are necessary for efficient binding to occur. Finally, we have examined the influence of the binding of

the L-His-NikP1 substrate on the dioxygen activation strategy of NikQ using spectroelectrochemistry and transient kinetics. Aminoacylated-NikP1 exerts little effect on the low reduction potential of NikQ, but restricts the binding of dioxygen to the heme-iron. In sum, these results reveal a complex linkage of NRPS structural changes for the recruitment and regulation of P450 tailoring enzymes.

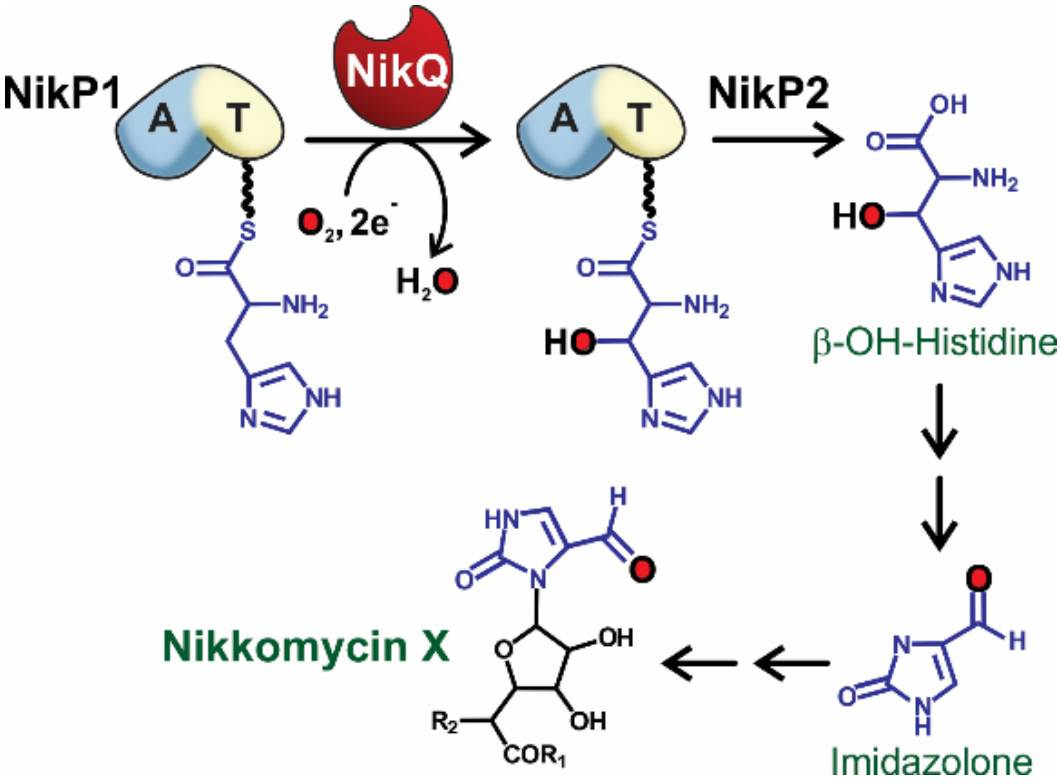

Figure 3.1. The biosynthesis of nikkomycin by *Streptomyces tendae*. The cytochrome P450 NikQ hydroxylates a histidine at the Cβ position while it is appended to the non-ribosomal peptide synthetase (NRPS) NikP1 as a phosphopantetheine-linked thioester. NikP1 is composed of an MbtH (not shown), and single adenylation (A) and thiolation (T) domains. Release by the thioesterase NikP2, followed by downstream processing, results in production of an imidazolone base that is integrated into nikkomycin X.

3.3 Results and Discussion

3.3.1 Fine Control of the NikP1 Post-Translational Modification State

The ability to precisely control the NRPS post-translational state is imperative for calibrated binding studies. Nearly quantitative phosphopantheinylation and aminoacylation reactions were verified by quadrupole time-of-flight mass spectrometry (QTOF-MS) of NikP1. Figure 3.2 shows the deconvoluted mass spectra of NikP1 obtained for the *apo* form, upon co-expression of the NRPS with the phosphopantetheine (ppant) transferase Sfp and following incubation with ATP and L-histidine to initiate successive adenylation and thiolation reactions. The spectra of each preparation show two dominant forms that are separated by m/z = 131 – 134, most likely owing to incomplete excision of the N-terminal methionine during expression. The MS of heterologously expressed and purified NikP1 (Figure 3.2, trace a) displays a main peak at 74,024 ± 4 Da, in close agreement with the expected mass of the *apo* form lacking the methionine (74,028 Da). Upon co-expression with Sfp (Figure 3.2, trace b), both forms convert to a species with a mass that is 342 Da higher, with a main peak at 74366 ± 5 Da, consistent with addition of the ppant arm (m/z = 341 Da) and full conversion to the *holo* form. Following prolonged incubation with ATP and L-histidine (trace c), the spectrum shifts by 135 Da to 74,501 ± 4 Da, demonstrating quantitative attachment of L-histidine to the phosphopantetheine arm as a thioester (m/z = 139 Da). Thus, all of the relevant forms of NikP1 (*apo*, *holo*, and L-His-loaded) can be generated in a highly homogeneous manner.

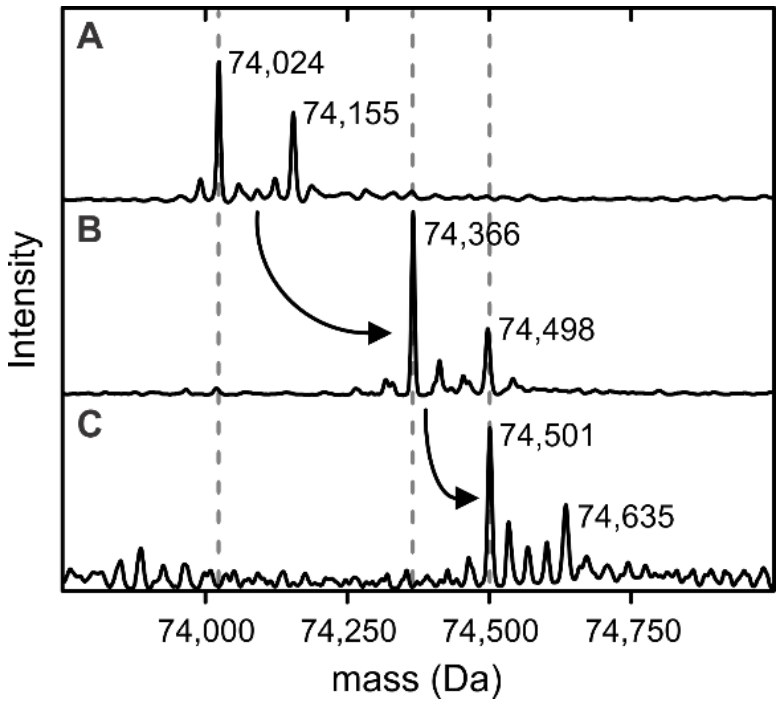

Figure 3.2. Deconvoluted quadrupole time of flight mass spectra of purified NikP1 in different post-translationally modified states. MS was performed on the (**a**) as isolated apo-form, (**b**) upon co-expression with the phosphopantetheine transferase Sfp, and (**c**) after the addition of L-histidine and ATP to produce L-His-NikP1.

3.3.2 Optical and EPR Characterization of NikQ

NikQ was cloned and heterologously expressed in *E. coli* as previously reported[10] and purified through a two-step chromatographic procedure, outlined in the Methods. The enzyme was characterized by optical spectroscopy in the ferric, ferrous, and ferrous-carbonmonoxy bound states (Figure 3.3). NikQ exhibits absorption characteristics that are similar to many other P450 cytochromes. The purified enzyme displays a Soret maximum at 419 nm and Q-bands at 536 and 567 nm, indicative of a ferric low-spin (LS) water bound enzyme. Upon reduction with dithionite, the Soret and Q-bands shift to 410 and 536 nm respectively. Retention of the axial thiolate ligand was demonstrated after exposure of the

ferrous form to carbon monoxide and produced the characteristic 446 nm Soret maximum that defines the enzyme class. Only a small fraction (≤ 20 % of total enzyme) was found to be in the inactive P420 state (λ_{max}~ 422 nm), which progressively forms in the time frame required to reduce the protein, expose to CO, and collect a spectrum.

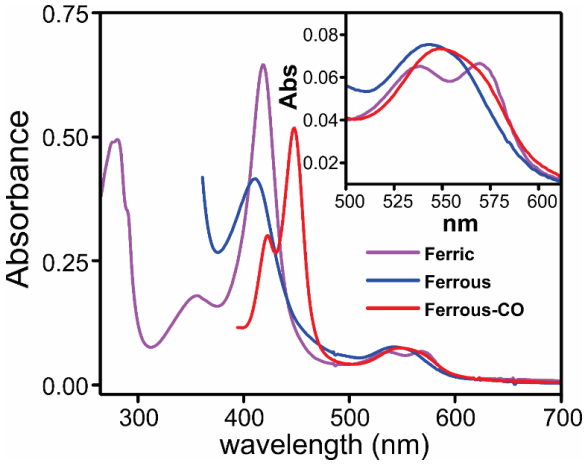

Figure 3.3. Optical absorption spectrum of NikQ in the ferric (purple), ferrous (blue), and ferrous carbonmonoxy-bound states. The inset shows the expanded region from 500 to 600 nm.

Many P450s, including some NRPS-modifying enzymes,[8-9, 13, 17, 36] undergo some degree of Type I spectral changes upon substrate binding that results from a displacement of the axial-bound water. This ligation change can produce a low- to high-spin (HS) state conversion, and accompanying shift in the Soret maximum from 418 nm to around 392 nm. The addition of a 10 fold molar excess of L-His-NikP1 did not result in any appreciable alteration in the optical spectrum of NikQ (Figure 3.4). The absence of absorption changes could be attributed to lack of stable complex formation, a large dissociation constant (K_D) between NikQ and L-His-NikP1, or an optically silent binding event. These possibilities are addressed below.

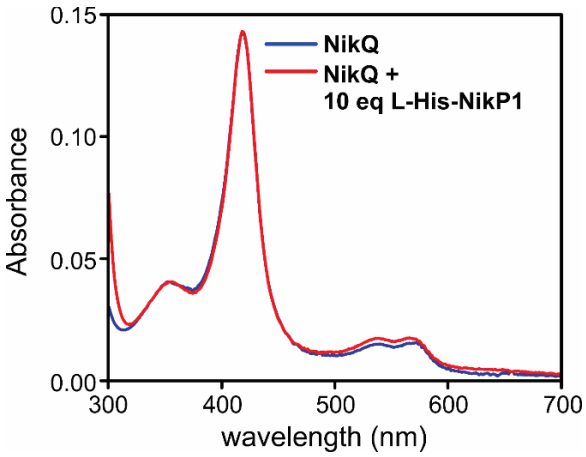

Figure 3.4. NikQ does not undergo an optical change upon addition of substrate. Absorption spectrum of ferric NikQ alone (blue), and in the presence of 10 molar equivalents of L-His-NikP1 (red).

The binding of NikP1 to NikQ was also probed by electron paramagnetic resonance (EPR) spectroscopy (Figure 3.5). The spectrum of NikQ is highly homogeneous and exhibits a single set of g-values at 2.44, 2.25, and 1.91, features that are consistent with a LS thiolate ligated heme with an axial-bound water and in good agreement with the optical data (Figure 3.5, trace A). Upon addition of 5 molar equivalents of NikP1 in the *holo*-form lacking an appended amino acid, the signal was unchanged (Figure 3.5, trace B). However, introduction of a similar amount L-His-NikP1 to NikQ resulted in a decrease of the signal at g_z = 2.44 which is accompanied by the appearance of two new features at g_z = 2.47 and 2.41 and a new g_x signal at 1.92 (Figure 3.5, trace C). These new spectral forms of NikQ were not observed when free L-histidine was added to NikQ at a similar stoichiometry (Figure 3.5, trace D), congruent with previous studies that have concluded that the free amino acid is not a competent substrate.[10] This implies that NikP1, the ppant arm, and the amino acid are all required to bind to NikQ, or in the very least, are necessary to elicit the observed electronic changes at the heme-iron.

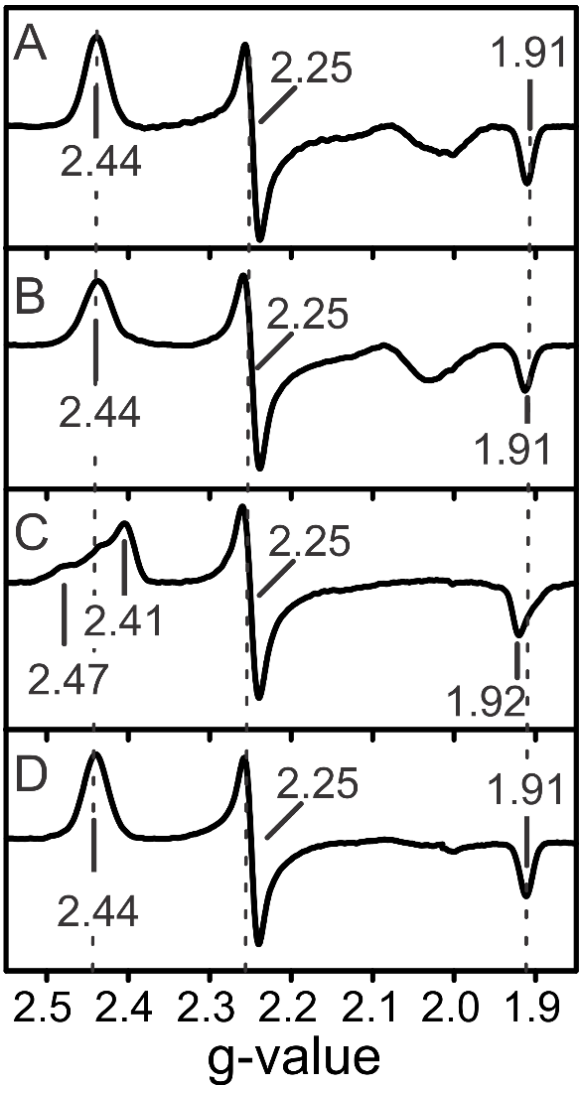

Figure 3.5. EPR of NikQ in the absence or presence of substrate, the holo-NRPS, or L-histidine. 8K X-band EPR of 100 μM NikQ (**A**) in the substrate free form, or with addition of 5 molar equivalents of (**B**) holo-NikP1, (**C**) L-His-NikP1, or (**D**) free L-histidine. The principle g-values of all major species are indicated.

Both new sets of g-values observed with L-His-NikP1 binding are consistent with the introduction of a tethered L-histidine substrate into the active site of NikQ and in close proximity to the heme iron. Based on similarity to EPR of P450s bound to nitrogen donors (e.g. azole),[37-39] we assign the less populated g_z = 2.47 state as most likely arising from direct coordination of the tethered histidine. The origin of the major g_z = 2.41 species is more difficult to interpret, but may signal an alteration in the strength of the axial water upon introduction of a hydrogen bond acceptor to the pocket. This binding conFigureuration may not be anticipated to produce significant changes to the absorption spectrum of NikQ at room temperature.[37] The spectral perturbations that occur upon L-His-NikP1 binding were used as a probe to determine the affinity of NikQ to its cognate aminoacylated NRPS. L-His-NikP1 was added at several different concentrations to 100 μM NikQ and EPR spectra were collected. Following baseline subtraction of the spectra, the g_z signals were fit to a series of Gaussians, and the resulting areas were used to determine the fraction of NikQ bound to L-His-NikP1. Representative spectra of the expanded g_z region and the fits at several NRPS concentrations are shown in the inset of Figure 3.6. Both of the EPR species specific to binding grow with increasing concentrations of L-His-NikP1 and appear to saturate at molar ratios of NRPS:P450 above 3:1 (300 μM L-His-NikP1 and 100 μM NikQ). When plotted as a function of L-His-NikP1 and fit to a Morrison quadratic equation, necessary due to the large concentration of NikQ required for EPR titrations, a dissociation constant of 22 ± 5 μM was obtained. The dissociation constant measured for L-His-NikP1 and NikQ by EPR falls within the considerably large range of values measured for P450 Cβ amino acid hydroxylases obtained from other methods (Table 3.1).

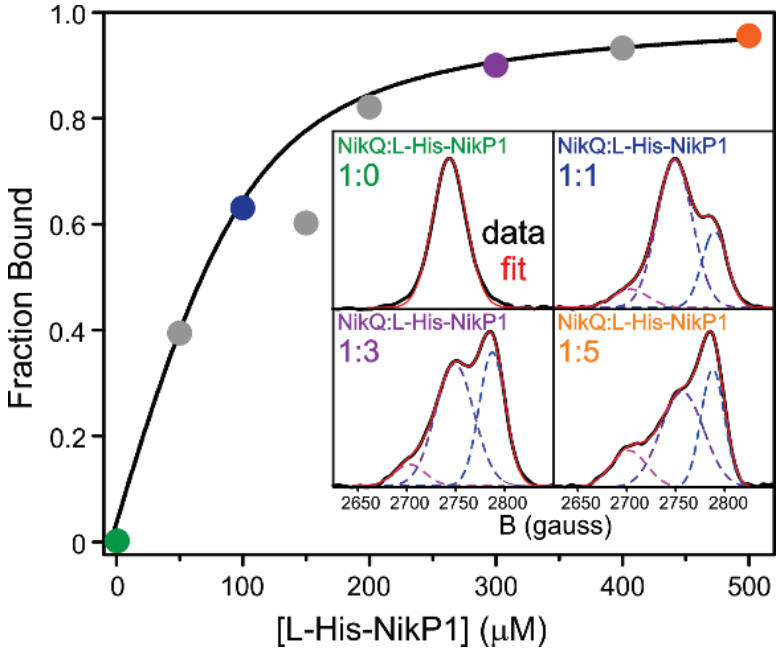

Figure 3.6. X-band EPR of NikQ with varying concentrations of L-His-NikP1. The fraction bound was calculated by a ratio of the forms corresponding to substrate-bound NikQ (g_z = 2.47, 2.41) over the total area and a dissociation constant was determined by fitting to the Morrison equation. Inset: Expanded g_z region after baseline subtraction and Gaussian fits to three individual species with g_z values of 2.47, 2.44, and 2.41 respectively. The resulting fit is indicated in red. The molar ratios of NikQ to L-His-NikP1 are noted for each titration point and the NikQ concentration was 100 μM.

Table 3.1 Binding Parameters of NRPS-amino acid Cβ hydroxylases

P450	NRPS composition	Amino Acid	K_D (μM)	Method	Reference
NikQ	AT	L-His	22	EPR	This study
$P450_{Sky}$	T	L-(O-Me)-Tyr	89[a] - 93[b]	[a] UV/Vis, [b]Sedimentation Velocity	13a, 15b
$P450_{Sky}$	T	L-Phe	187	UV/Vis	13
OxyD	T	L-Tyr	14	UV/Vis	8

3.3.3 Multiple forms of NikP1 bind to NikQ

The absence of EPR signal changes with *holo*-NikP1 could be due to a lack of stable complex formation or from the inability of the bare ppant arm to extend far enough into the NikQ active-site to induce electronic changes at the heme-iron. In order to correlate the EPR spectral perturbations to a macromolecular binding event, size exclusion chromatography (SEC) was employed to identify the minimal requirements necessary for stable complex formation. Crystallographic studies of an NRPS-modifying P450 β-hydroxylase ($P450_{sky}$) ligated to an excised T-domain containing an unnatural azole-containing ppant analog have suggested that the interface may be largely dominated by hydrophobic interactions between the two proteins.[14] Each form of NikP1 was added to NikQ and analyzed by SEC under both low (150 mM) and high (500 mM) ionic strength conditions to examine the nature of the interaction and assess the importance of electrostatics for binding (Figures 3.7 and 3.8 respectively). The elution pattern was monitored for total protein at 280 nm and by SDS-PAGE, and analysis of heme-containing fractions at 417 nm. In the absence of NikP1, NikQ (46 kDa) elutes off an S200 column with a retention volume of approximately 24 mL, consistent with an assignment as a monomer (Figure 3.9). NikP1 similarly elutes as a monomer at ~16 mL (Figure 3.8). The addition of a ten-fold molar excess of L-His-NikP1 results in nearly complete (>95%) disappearance of the peak corresponding to unbound NikQ and is replaced by a new peak with a significantly lower retention volume (~13.5 mL), evident in both the 280 nm and 417 nm traces (Figure 3.8 A, B). SDS-PAGE of individual elution fractions shows that both NikQ and NikP1 are present in this higher molecular weight form, consistent with formation of a stable complex (Figure 3.8 C). Under lower ionic strength conditions, the

peak corresponding to the ternary complex at 13.5 mL still forms, albeit to a lesser (~ 80 %) degree (Figure 3.7). The efficiency and partial enhancement for hetero-oligomer formation with high salt suggests that hydrophobic interactions are likely to be the most important for stabilizing the NRPS-P450 interface. A comparison of the absorption spectra of free NikQ and the enriched NikQ:L-His-NikP1 complex purified by SEC showed only very small changes in the Soret region (Figure 3.10).

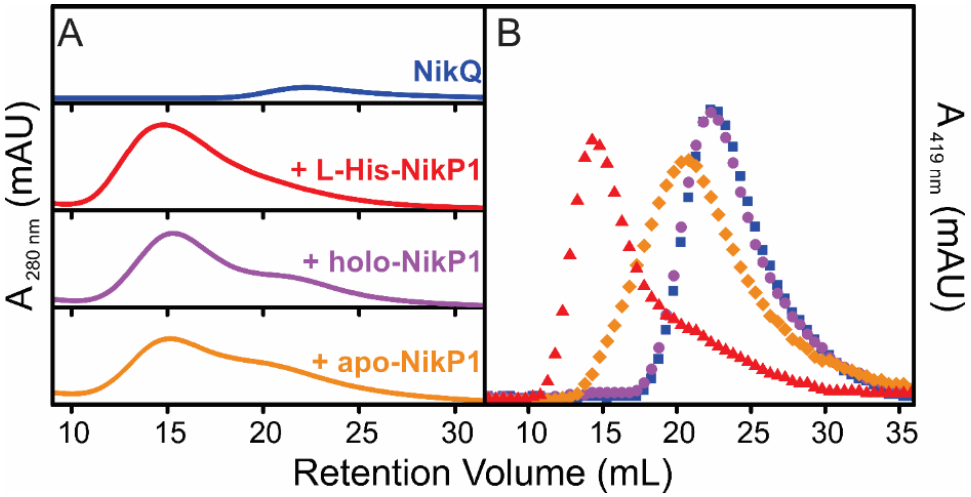

Figure 3.7. SEC reveals stable complex formation between NikQ and L-His-NikP1. Size exclusion chromatography (SEC) of free NikQ, or NikQ with the addition of different forms of NikP1 at a stoichiometry of 1:10 (NikQ:NikP1) in 25 mM HEPES pH 7.5, 150 mM NaCl. Chromatograms are from (**A**) online monitoring at 280nm or through (**B**) analysis of heme containing fractions at 419 nm.

The prerequisites for binding to NikQ were further probed using the *holo*- and *apo*-forms of NikP1 at the same fixed NRPS:P450 ratio of 10:1. The 419 nm chromatograms of NikQ incubated with *holo*-NikP1 were identical to those of free NikQ alone, with one elution peak at 24 mL, and SDS PAGE on individual fractions verified that no P450 was apparent in earlier fractions that would correspond to those of a complex. This would seem

to insinuate that the presence of the appended amino acid is critical for binding to occur. As a result, chromatograms obtained by mixing *apo*- form with NikQ were surprising as they revealed the formation (~ 60 %) of a new higher molecular weight complex that eluted significantly earlier than free NikQ. This new peak is differentiable in its retention volume (15.5 mL) from the L-His-NikP1:NikQ complex and free NikQ. As with the aminoacylated form, the *apo*-NikP1:NikQ complex still forms, but less efficiently in lower ionic strength.

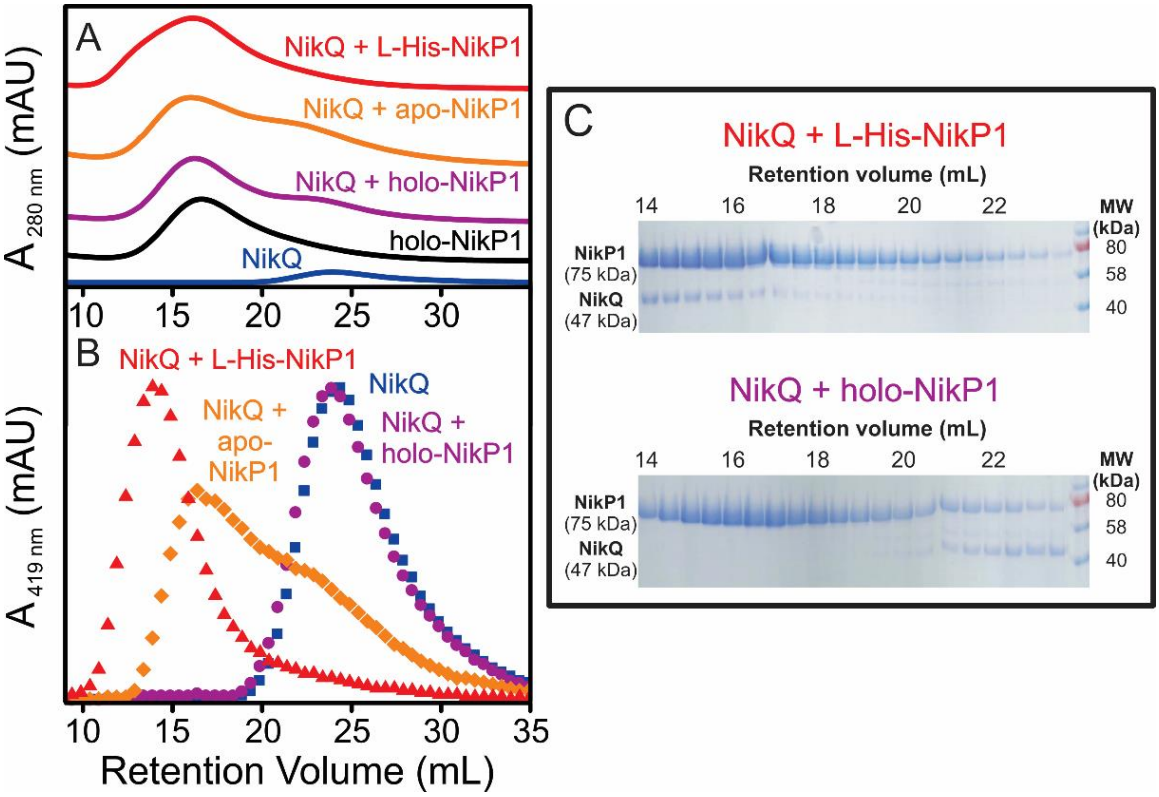

Figure 3.8: NikQ:L-His-NikP1 complex-formation exhibits an ionic strength dependence. Size exclusion chromatography (SEC) of free NikQ, or NikQ with the addition of different forms of NikP1 at a stoichiometry of 1:10 (NikQ:NikP1) in 25 mM HEPES pH 7.5, 500 mM NaCl. Chromatograms are from (**A**) online monitoring at a wavelength of 280 nm or through (**B**) analysis of heme containing fractions at 419 nm. (**C**) SDS PAGE of elution fractions.

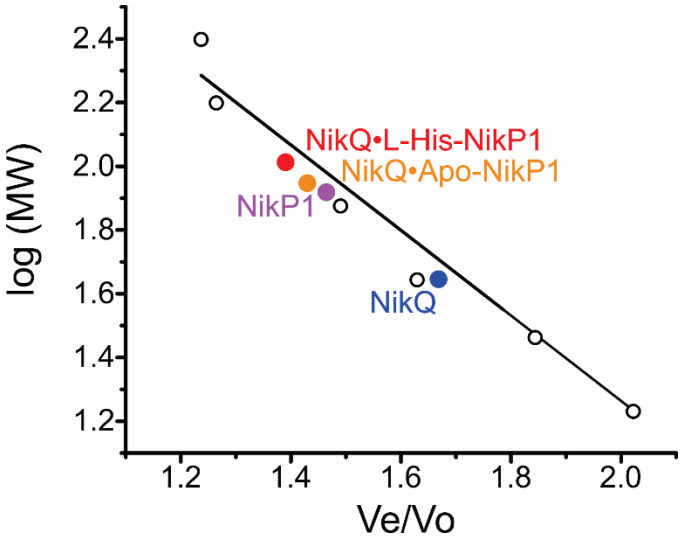

Figure 3.9. Size exclusion chromatography of NikQ, NikP1, and NikP1:NikQ complexes. The elution volume (Ve), normalized to the void volume (Vo) is plotted for NikQ and a series of calibrated molecular weight standards. The calculated molecular weight of the NikQ and NikP1 fall within the predicted range expected for a monomer. The apparent and calculated molecular weights follow: NikQ (43.7 kDa measured, 46.6 kDa calculated), NikP1 (80.7 kDa measured, 74.2 kDa calculated, NikQ:L-His-NikP1 (103.1 kDa measured, 121.2 kDa calculated), NikQ:apoNikP1 (87.6 kDa measured, 120.8 kDa calculated).

The SEC studies reveal an unusual pattern for the association of NikP1 and NikQ, which does not appear to scale with progressive modifications at the T-domain. In comparison, the broad-specificity Cβ hydroxylase involved in skyllamycin biosynthesis ($P450_{sky}$)[13] fails to bind to *apo*- or *holo*- T-domain forms,[15] suggesting that the NRPS cargo may help to establish interactions in that system. Given that different types of complexes seem to form with *apo*- and L-His-NikP1, reflecting slight differences in hydrodynamic radii, we probed the binding site location of NikQ with *apo*-NikP1. Provided that NikQ binds *apo*-NikP1 with similar contacts near the site of ppant attachment, rather than a distal

site (e.g. at the A or MbtH domains), the presence of NikQ should occlude phosphopantetheinyl transfer to NikP1.

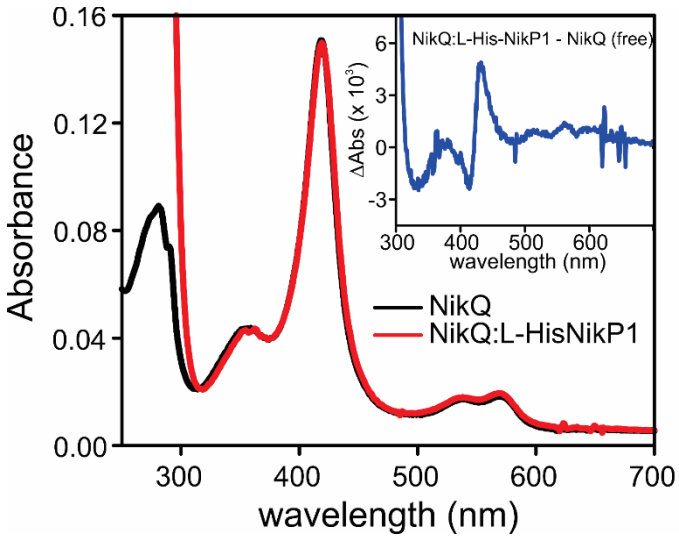

Figure 3.10. Absorbance spectra of SEC-eluted NikQ:L-His-NikP1 complex, versus free NikQ. Optical absorption spectrum of enriched NikQ:L-His-NikP1 (red) and free NikQ (black). Fractions of the co-complex, partially purified by size exclusion chromatography, were compared to the free enzyme. The Soret band is normalizes to facilitate comparison. A difference spectrum is shown in the inset, and shows minimal absorption differences.

The efficiency of ppant transfer to *apo*-NikP1 by the general-utility transferase (Sfp) was probed at various time points using a Bodipy-CoA analog, allowing for direct visualization of its addition by fluorescence. The SDS-PAGE gel, stained by coomassie or imaged at a wavelength near the excitation maximum of Bodipy, is shown in Figure 3.11. In the absence of NikQ, efficient ppant transfer proceeded rapidly and reached completion within 10 minutes. In comparison, when a five-fold molar excess of NikQ was included in the reaction mixture, the extent of ppant transfer progressed much more slowly and was incomplete by 20 minutes. Taken together with the SEC data, the Bodipy-CoA assay

provides evidence that NikQ binds *apo*- and L-His-NikP1 at very similar sites. Thus, the surface composition of the protein interface, rather than the appended amino acid, is the most important element for guiding molecular recognition by NikQ. In this context, the inability of *holo*-NikP1 to bind to NikQ would seem to originate from an alternative conformation of the NRPS that does not successfully expose the T-domain surface that is used for binding. Using a mechanism-based inhibitor, Gulick and Aldrich have structurally-characterized an AT didomain[24] and full NRPS module[26] in states that approximate those used during thioester formation. If a similar architecture is adopted by *holo*-NikP1, the surface of the T-domain required for NikQ binding would be occluded due to extensive interactions with the A domain, which are also thought to be largely hydrophobic.

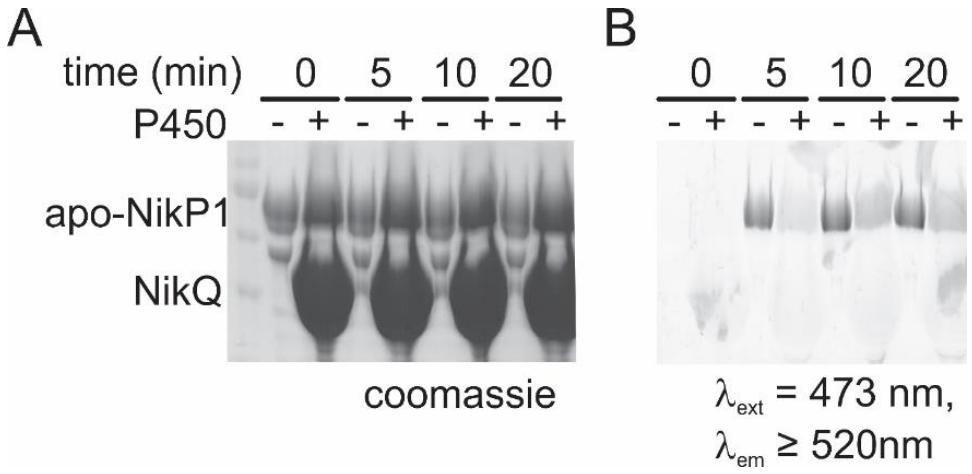

Figure 3.11. Bodipy-CoA binding to apo-NikP1 is impaired in the presence of NikQ. SDS PAGE of phosphopantetheinylation reactions of 20 µM *apo*-NikP1 in the absence (-) or presence (+) of 100 µM NikQ using a Bodipy-coenzyme A analog. Reactions were quenched at the indicated time points and visualized by (**A**) Coomassie staining or (**B**) excitation at 473 nm to monitor the transfer of the Bodipy to the NRPS.

3.3.4 Role of the L-His-NikP1 on the Regulation of NikQ Dioxygen Activation

P450s are often finely regulated at several steps of catalysis by effectors that can be broadly characterized as small molecules (e.g. substrates or inhibitors), or auxiliary proteins (e.g. redox partners). In some ways, an NRPS-tethered substrate could resemble a hybrid of both classes. In light of the lack of a spectroscopic change in NikQ upon binding to L-His-NikP1, we sought to examine whether this substrate exerted any effects on the early catalytic steps of NikQ. To the best of our knowledge, the influence of NRPS binding on individual steps of the oxygen activation process has not been probed for any P450 to date. For many P450s, substrate binding is accompanied by an increase in heme midpoint potential,[40-41] which thermodynamically gates transfer of the first electron required by the catalytic cycle. The midpoint potential of NikQ was measured in the presence and absence of L-His-NikP1 using a dye-mediator approach that is described in the Materials and Methods. The resulting Nernst plots for both conditions are presented in Figure 3.12, and representative spectra obtained from reductive titrations of substrate-free and -bound NikQ are shown in the inset of Figure 3.12 and in Figure 3.13 respectively. In the substrate-free form, NikQ exhibits a midpoint potential of -415 ± 40 mV. This value is lower than many, but still within the range (-300 to -400 mV) observed for low-spin P450s (Table 3.2). The Nernst plot of the substrate-bound form is superimposable with substrate-free NikQ, and linear fitting results in an identical value within the experimental error (-414 ± 20 mV). These results imply that the perturbations that are observed by EPR upon L-His-NikP1 binding do not exert any appreciable changes on heme electronics. In the absence of any additional changes that may occur upon redox partner binding, electron transfer appears to be completely decoupled from substrate binding. Although the native redox partner for

NikQ has yet to be identified, the redox potential values measured here are consistent with previous turnover studies by Chen *et al* that utilized the low-potential spinach ferredoxin (-420 mV)[42] as a competent, albeit sluggish, surrogate redox donor.[10]

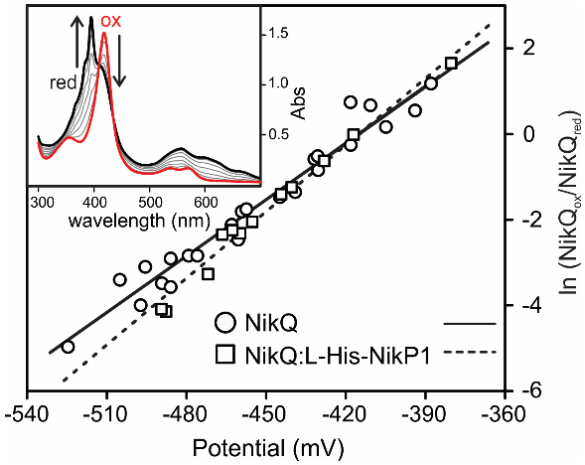

Figure 3.12. Reduction potential measurements of NikQ. Nernst plots for the reduction of free NikQ (open circles) and NikQ bound to L-His-NikP1 (open squares). *Inset:* Reductive titration of free NikQ.

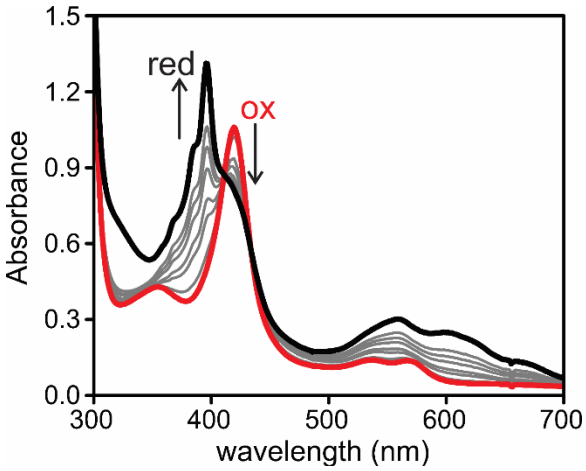

Figure 3.13. Representative spectra from reduction potential measurement with methyl viologen indicator dye. These were obtained during reductive titration of the NikQ:NikP1 co-complex.

Table 3.2 Redox Potential, O_2-binding (k_{on}), and autoxidation rates (k_{autox}) of NikQ in comparison to other cytochromes P450

P450	Substrate	E° (mV)	k_{on} ($M^{-1}s^{-1}$)	k_{autox} (s^{-1})	References
NikQ	-	-415	2.2×10^6	2.8	This study
	L-His-NikP1	-415	4.6×10^4	2.5	This study
CYP3A4	-	[a]-220	[b]5×10^5	[b]20	[a]54
	bromocriptine	[a]-137	[b]3.5×10^4	[b]0.12	[b]55
CYP101	-	[c]-303		[d]0.002	[c]41, [d]56
	camphor	[e]-170	[f]7.7×10^5	[f]0.0001	[e]57, [f]58
CYP102	-	[g]-427	[g]3.0×10^6 *	[g]0.11*	[g]44
	arachidonate	[g]-289		[h]0.032	[h]59
CYP11A1	-	[i]-412		[j]0.004 †	[i]60, [j]61
	cholesterol	[i]-278	[k]5.8×10^5	[j]0.0003 †	[k]62
CYP8A1	-		5.9×10^5	12	63
XplA	-	-268	6.6×10^6 *	2.25*	64

Unless otherwise noted, O_2 on rates (k_{on}) and autoxidation rates (k_{autox}) were determined at temperatures of 2 °C – 10 °C. *measured at 15 – 25 °C; †measured at -17 °C

Dioxygen binding in P450s, and the stability of the resulting oxy-complex, is also finely tuned by the binding of either small molecule or protein effectors. NRPS-substrates have been previously shown to trigger O_2-activation in other types of tailoring enzymes, such as the Fe^{2+} and α-ketoglutarate-dependent halogenase SyrB2[16] and the dinuclear iron Cβ-hydroxylase CmlA.[33, 43] To probe for these influences in NikQ, we measured the oxygen binding and autoxidation rates by rapidly mixing the ferrous form of the enzyme with O_2 at 4 °C in stopped flow studies. Photodiode array (PDA) traces for the reactions of substrate-free and bound NikQ with 200 μM O_2 are shown in Figure 3.14 A and B. The PDA spectra are essentially identical and reveal rapid formation of the NikQ-oxy complex with a Soret maximum at 426 nm and Q-band at 556 nm. This is followed by the decay of the oxy-complex over the course of 1 second to the low-spin ferric enzyme at 418 nm.

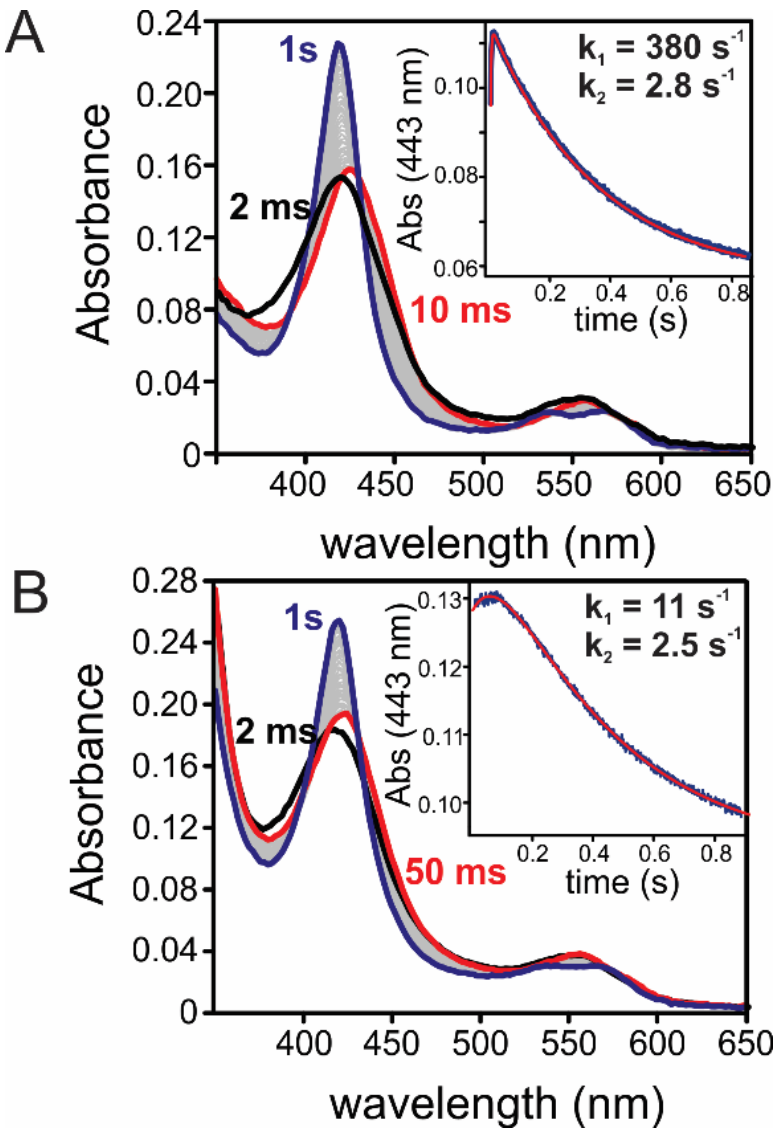

Figure 3.14. Transient kinetic studies of the reaction of ferrous (A) NikQ, and the (B) ferrous NikQ:L-His-NikP1 complex with O_2 at 4°C. Concentrations were ~2.5 μM NikQ and 200 μM O_2 after mixing. Photodiode array spectra show the initial ferrous heme (black), formation of the oxy-ferrous intermediate (red), and decay to the ferric-aquo state (blue). *Inset:* Timecourse for oxyferrous formation (k_1) and decay (k_2) monitored at 443 nm, fit to a two summed exponential expression with observed rates shown.

The time courses for oxy- formation and decay at 443 nm, shown in the insets, are more revealing. Fitting to a two-exponential expression revealed a relatively fast rate of autoxidation (2.8 s^{-1}) of NikQ compared to many P450s (Table 3.2). The rate constants for autoxidation of the L-His-NikP1:NikQ complex are largely unchanged (2.5 s^{-1}), demonstrating that the origin of fast decay in both cases most likely stems from the low reduction potential[44] of NikQ. However, the formation of the oxyferrous intermediate is considerably altered upon L-His-NikP1 binding. A plot of the observed rates versus O_2 concentration yield linear plots (Figure 3.15). The bimolecular rate constants for formation of the oxygenated complex, obtained from the slopes, are 2.2 x 10^6 M^{-1} s^{-1} and 4.6 x 10^4 M^{-1} s^{-1} for substrate-free and L-His-NikP1 bound NikQ.

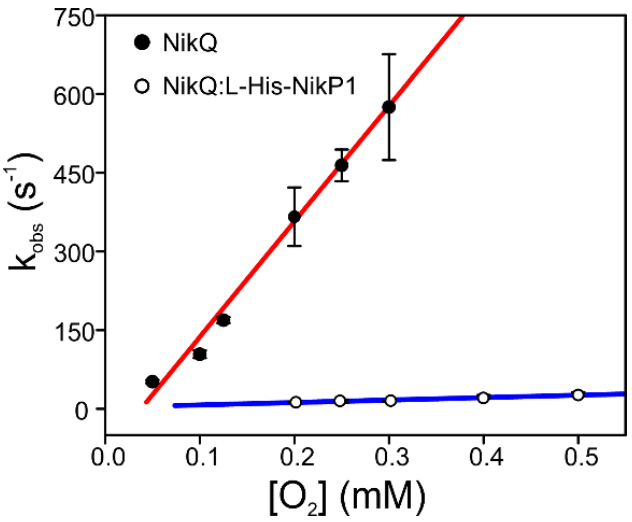

Figure 3.15. O_2-dependence of NikQ oxy-intermediate formation. Oxygen concentration dependence of the observed rates for oxyferrous NikQ formation in the absence (closed circles) and presence (open circles) of L-His-NikP1. The slope of the plot yields the bimolecular rate constant for O_2 binding.

3.4 CONCLUSIONS

The results described here indicate that the regulation of NikQ is gated by the NikP1 assembly process at several steps, revealed by use of an intact trimodular NRPS. Figure 3.16 summarizes our current understanding of the remarkable interplay between NikP1 post-translational modifications and tailoring by NikQ. NikQ binds to apo-NikP1 with an estimated dissociation constant of ~ 50 μM based on the fraction bound that is observed from SEC studies. Although slightly weaker than the interactions with the cognate L-His-NikP1 substrate measured by EPR, this data suggests that correct exposure of the carrier protein surface, rather than the appended amino acid, serves as the most important binding determinant. Once the ppant arm is installed by an associated transferase, the NRPS may adopt a new conformation which is directed towards the A domain for subsequent loading of L-histidine onto the T-domain. As a result, binding to NikQ cannot occur. Following thiolation, the T-domain surface necessary for binding is again exposed, allowing for the recruitment of NikQ. It is possible that other modules of the NRPS may also facilitate the binding process. Intriguingly, the lyngbyatoxin biosynthetic gene cluster contains an unusual P450 that contains an N-terminal MbtH domain, but can oxidize free dipeptides and exhibits a more relaxed substrate specificity than NikQ.[45-46] For nikkomycin, the coupling of macromolecular recognition to NRPS maturation may serve to reinforce directionality in the biosynthetic process. Tailoring enzyme binding is largely thwarted until the NRPS is primed with an amino acid.

The regulation of NikQ by NikP1 is highly atypical for P450s and much different than other classes of tailoring enzymes such as CmlA and SyrB2. The redox potential and autoxidation rate of NikQ are largely unregulated, and even dysregulated in the case of

dioxygen binding, from a substrate binding event. At first glance, this would appear to uncouple an important biosynthetic process and possibly lead to the production of reactive oxygen species. The most straightforward explanation is that the low redox potential of NikQ ensures that first electron transfer is thermodynamically unfavorable and rate-limiting with respect to O_2 binding and subsequent catalytic steps. It is possible that free NikQ is limited by the rapid adenylation of L-histidine by NikP1, or possibly, through a regulation of steps after installation of the OH at the Cβ position. A slow release of the product from NikQ, coupled to sluggish hydrolysis by the thioesterase NikP2[10] could possibly serve this role.

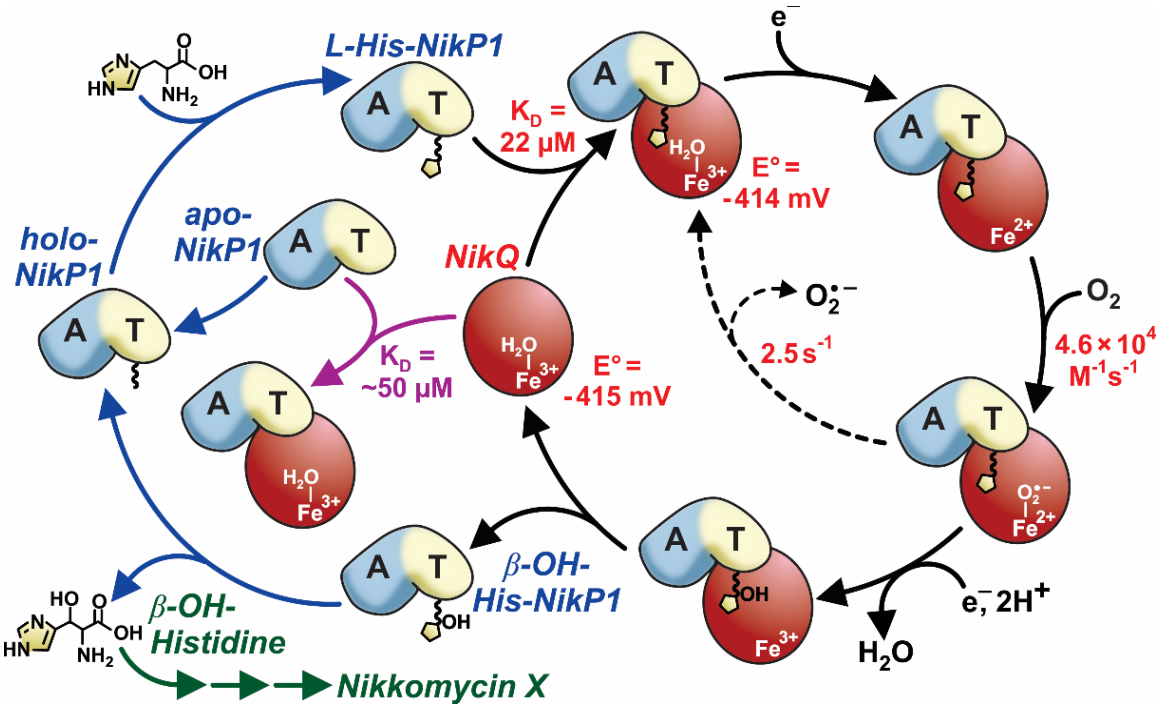

Figure 3.16. Proposed summary of the interplay of NikP1 maturation, the recruitment of NikQ, and the regulation of early catalytic steps by L-His-NikP1. The MbtH domain of NikP1 is omitted for clarity. The K_D value describing the interaction between NikQ and apo-NikP1 was approximated from the level of complex formation observed during SEC experiments. The K_D value for L-His-NikP1 was determined by EPR. Redox potentials and O_2 binding and autoxidation rates were determined by spectroelectrochemistry and rapid mixing stopped flow studies respectively.

3.5 MATERIALS AND METHODS

3.5.1 Reagents and Chemicals

The p283 plasmid was obtained from the DNASU plasmid repository. All microbiology reagents, and adenosine 5'-triphosphate (ATP), chloramphenicol, dithiothreitol (DTT), and kanamycin were purchased from Research Products International. Ampicillin and lysozyme were purchased from bioWorld. δ-aminolevulinic acid was from Carbosynth. L-histidine, Neutral Red, Safranin T, sodium hydrosulfite, Tris-(2-carboxyethyl)-phosphine hydrochloride (TCEP) were from Sigma Aldrich. Isopropyl-β-D-Thiogalactopyranoside (IPTG) was from Gold Biotechnology. Vectors for overproduction of the general utility phosphopantetheine transferase from *Bacillus subtilis* (Sfp)[47] and co-expression were provided by Prof. Courtney Aldrich.

3.5.2 Cloning, Heterologous Expression, and Purification

Genomic DNA was isolated from *Streptomyces tendae Tü901* (ATCC) using a Promega Wizard SV Genomic DNA Purification kit with the following modifications. The cell pellet was resuspended in a mixture of 480 µL 50 mM EDTA and 120 µL 10 mg/mL chicken lysozyme, incubated at 37 °C for 1 hour, then centrifuged and the supernatant discarded. Polymerase chain reactions (PCR) were performed to amplify the *nikQ* and *nikP1* genes using the following primers with restriction sites underlined.

NikQF (NdeI) 5'-CCCAAACATATGAGAGTTGACCTGTTCGACCCGCTC-3'

NikQR (XhoI) 5'-CCCTATCTCGAGTCAGGCCCTCGGGACGAATTT-3'

NikP1F (NdeI) 5'-CCCGGGCATATGGTGAACCCGATTCATGACGACAAC-3'

NikP1R (XhoI) 5'-GGAATACTCGAGGCTCCGTCCGGCGCG-3'

The *nikQ* insert was cloned into pET28b and the *nikP1* insert into pET21b. In order to ensure that the C-terminal hexahistidine tag on the NRPS had no influence on P450 binding parameters, the *nikP1* gene was also cloned into a p283 vector to introduce a tobacco etch virus (TEV) protease cleavable histidine tag, using the same forward primer and the following reverse primer.

NikP1R2 (EcoRI) 5'-GAGATAGAATTCGCTCCGTCCGGCGCG-3'

No significant changes were noted in size exclusion chromatography studies. NikQ was expressed using BL21(DE3) cells in 1 liter cultures of Luria Broth (LB) from Research Products International (RPI), and supplemented with 50 µg/mL kanamycin (RPI), 25 µM $FeCl_3$, and 25 µM δ-aminolevulinic acid. Following inoculation with 10 mL of an overnight starter culture, the cultures were grown to OD_{600} = 0.8 at 37 °C and 200 rpm, then incubated for 74 hours at 15 °C and 150 rpm. Cells were harvested via centrifugation, then resuspended in Ni-NTA equilibration buffer (50 mM potassium phosphate monobasic, 10 mM imidazole, 300 mM NaCl, pH 7.5), lysed by sonication and centrifuged at 16,000 RPM. The clarified lysate was loaded onto an Ni-NTA column equilibrated in the same buffer. The column was washed with 10 column volumes of Ni-NTA wash buffer (50 mM potassium phosphate monobasic, 25 mM imidazole, 300 mM NaCl, pH 7.5), and eluted in the same buffer containing 200 mM imidazole. Red fractions were dialyzed overnight at 4 °C against 50 mM HEPES pH 7.5 with 5% glycerol. The dialyzed fractions were loaded onto a DEAE column equilibrated with 50 mM HEPES pH 6.5, and eluted with a 500 mL gradient of 50 mM HEPES pH 6.5 from 0 to 500 mM NaCl. The resulting protein was ~95% pure, based on SDS-PAGE analysis and by optical spectroscopy, with an R_z (A_{417}/A_{280}) = 1.70.

NikP1 was expressed in BL21 (DE3) cells to yield the *apo* form, and co-expressed with Sfp to produce the *holo* form. Similar expression conditions were used for the heterologous expression of both constructs in LB media, with the exception of the antibiotic used (100 µg/mL ampicillin for pET21b, and 50 µg/mL kanamycin for p283). When co-expressed with Sfp, 30 µg/mL chloramphenicol was also included. Following inoculation, cultures were grown at 37 °C to an OD_{600} = 0.9 - 1.2, 60 µM of IPTG was added, and the temperature was decreased to 15 °C. Cells were harvested 16 hours after induction via centrifugation and purified by Ni-NTA chromatography as described above for NikQ. Following elution, protein-containing fractions were dialyzed against 75 mM Tris, 10% glycerol, 1 mM dithiothreitol, pH 7.5. The resulting protein was >95% pure, as determined by SDS-PAGE. The extinction coefficient of NikQ at 419 nm was determined using the pyridine hemochromagen method ($\varepsilon_{419\ nm}$ = 110 mM^{-1} cm^{-1}).[48] An extinction coefficient for NikP1 at 280 nm was estimated using a calculated extinction coefficient from ExPASy ProtParam ($\varepsilon_{280\ nm}$ = 84 mM^{-1} cm^{-1}).[49]

3.5.3 Aminoacylation of NikP1

Aminoacylation reactions of NikP1 were carried out at the following final concentrations: 30 µM Holo-NikP1, 3 mM Tris-(2-Carboxyethyl)-Phosphine Hydrochloride (TCEP), 750 µM L-histidine, 3 mM Adenosine 5'-Triphosphate Disodium Salt Hydrate, 10 mM $MgCl_2$, and 75 mM Tris pH 7.5. Reactions were incubated at 4 °C for 12-16 hours and desalted into 50 mM HEPES pH 7.5 buffer using PD-10 desalting columns from GE Healthcare Life Sciences. Samples were then concentrated at 4 °C using Amicon Ultra-15 30,000 kDa filters. Samples that were not used immediately were frozen

in liquid nitrogen and stored at -70 °C. MS analysis showed no influence of desalting, concentrating, or freeze-thawing on the post-translational state of the NikP1.

3.5.4 Mass Spectrometry

Apo-, holo-, and L-histidine-loaded NikP1 samples were desalted into water using a PD-10 desalting column, concentrated to 120 µM, flash frozen in liquid nitrogen, and stored at -20 °C prior to mass spectrometric (MS) analysis. Prior to injection, samples were thawed on ice, and diluted to 7.5 µM by adding 10 µL of the 120 µM protein to 150 µM 1:1 MeOH/H_2O with 1% acetic acid. MS was performed at the Mass Spectrometry Center at the University of South Carolina. ESI (+) spectra were obtained using a Waters Quadrupole Time-of-Flight (QTOF) Micromass instrument and deconvoluted using MaxEnt software.

3.5.5 Absorbance Spectrophotometry

An Agilent 8453 UV-vis instrument was used for all optical spectrophotometric studies. Sodium hydrosulfite (dithionite) was prepared in a septum-sealed bottle at a concentration of 10 mM by degassing the solid, followed by the addition of N_2-purged 50 mM HEPES pH 7.5 using a gas-tight Hamilton syringe. The solution was subsequently degassed for an additional 40 minutes to ensure complete anaerobicity. In a sealed cuvette, 1 mL of 6 µM NikQ in 50 mM HEPES pH 7.5 was purged on ice with CO gas for 20 minutes, and a low spin/oxidized spectrum was recorded. The protein was reduced via the addition of dithionite solution, and a Fe^{2+}-CO spectrum was collected. The experiment was repeated using the same protein stock and preparation method, but purging the cuvette and protein with N_2 gas instead of CO, to obtain the ferrous P450 spectrum. In order to investigate whether NikQ undergoes any spectral changes upon substrate binding, 10 µM

NikQ was titrated with L-His-NikP1 to concentrations of 100 µM, and the spectrum of free NikQ compared to that of the enzyme in the presence of excess L-His-NikP1. These spectra were comparable, both in terms of Soret and Q-band maxima, to those obtained from fractions containing the NikQ:L-His-NikP1 complex in size exclusion chromatography (SEC) studies.

3.5.6 Electron Paramagnetic Resonance (EPR)

L-His-NikP1 was prepared as described above, and concentrations ranging from 0 to 500 µM were incubated with 100 µM NikQ in a total volume of 225 µL for 1 hour at 4 °C before transferring into EPR tubes and flash freezing in liquid nitrogen. Data was collected at 8-9 K using a Bruker X-band EMXplus EPR with an Oxford Instruments ESR900 X-band continuous flow liquid helium cryostat with 10 G modulation amplitude and a microwave power of 2 mW. Data was baseline corrected using SpinCount and Origin software using a spline function. The g_z peak (2600 to 2900 Gauss) was fit to a single Gaussian function for samples containing NikQ, NikQ + L-histidine, and NikQ + holo-NikP1, or the sum of three Gaussians for spectra of NikQ + L-His-NikP1. For EPR data from samples containing L-His-NikP1 and NikQ, the sum of areas corresponding to spectral signatures of the bound complex (g_z = 2.47 and 2.41), were divided by the sum of the total area (g_z = 2.47, 2.44, and 2.41), and the fraction of NikQ perturbed was calculated for each NikQ:L-His:NikP1 ratio. The bound fraction was calculated and plotted as a function of L-His-NikP1 concentration. The dissociation constant (K_D) was calculated from a Morrison fit[50] using the following equation, where f_{pert} is the fraction perturbed, $f_{pert,max}$ is the spectral perturbation at saturation, [ES] is the concentration of NikQ:L-His-NikP1 complex, [E_{tot}] is total NikQ concentration, [S_{tot}] is the total L-His-NikP1 concentration, and the fraction

bound is given by the ratio of [ES] to [E_{tot}]. Non-linear fitting procedures indicated that $f_{pert,Max}$ ~ 0.52.

$$\frac{f_{pert}}{f_{pert,max}} = \frac{[ES]}{[E_{tot}]} = \frac{(K_D + [E_{tot}] + [S_{tot}]) - \sqrt{(K_D + [E_{tot}] + [S_{tot}])^2 - (4\,[E_{tot}]\,[S_{tot}])}}{2\,[E_{tot}]}$$

3.5.7 Size Exclusion Chromatography (SEC)

SEC experiments were carried out using a HiPrep 16/60 Sephacryl S200 HR column from GE Healthcare using an ÄKTA FPLC with a P-920 pump, Frac900 fraction collector, and UPC900 monitor equipped with a 280 nm UV filter. A 25 mM HEPES pH 7.5 buffer containing either 500 or 150 mM NaCl was used to equilibrate the column. A 1.3 mL mixture of 10 µM NikQ, alone or in the presence of 100 µM *apo*-, *holo*-, or L-His-NikP1, was incubated on ice for 1 hour, and loaded onto the column with a flow rate of 0.3 mL/minute over a 5 mL block column injection equipped with a 1.1 mL injection loop at 8 °C. The elution was carried out over a 120 mL at a flow rate of 0.4 mL/minute, and 0.5 mL fractions were collected and analyzed for absorbance at 419 nm on to determine the quantity of NikQ in each fraction. The absorbance at 419 nm was plotted against the retention volume corresponding to each fraction.

3.5.8 Reduction Potential Measurements

The reduction potential of free and bound NikQ was determined spectrophotometrically using a dye/mediator approach described previously.[41] Methyl viologen (E°= -446 mV) was chosen as a redox indicator dye following unsuccessful attempts using safranin T (E°= -289 mV) or neutral red (E°= -325 mV) that suggested that NikQ has a reduction potential significantly lower than these indicators. A 1 mL mixture of 10 µM NikQ and 10 µM methyl viologen in 50 mM HEPES pH 7.5 was purged in N_2

gas in a septum-sealed cuvette on ice for 20 minutes. After taking an initial spectrum of the starting degassed mixture, dithionite was titrated into the cuvette in 1 µL aliquots from an anaerobic 5 mM stock solution. After each addition of dithionite, multiple spectra were taken to ensure equilibrium was reached. This procedure was repeated until both the dye and P450 were fully reduced. The absorbance increase at 395 nm upon reduction of methyl viologen (ε_{395nm} = 42.1 $mM^{-1}cm^{-1}$)[51] and decrease at 419 nm upon reduction of P450 (ε_{419nm} = 110 $mM^{-1}cm^{-1}$) were used to monitor the reduction of dye and P450 respectively. Data processing was analyzed using the Nernst equation in the manner previously described by Wilson et al.[52] The reduction potential of NikQ in the presence of 100 µM L-His-NikP1 was measured in an identical fashion.

3.5.9 Stopped Flow Spectroscopy

An Applied Photophysics SX20 stopped flow equipped with an anaerobic accessory was used for all rapid kinetics experiments. Degassed 50 mM HEPES pH 7.5 buffer and 10 mM sodium dithionite were prepared as described above. Stopped flow syringes were rinsed with dithionite followed by anaerobic buffer to scrub the system of O_2. NikQ (5 µM) was degassed under N_2 gas in a sealed bottle on ice stirring for 20 minutes. The protein solution was reduced using a limited amount of sodium dithionite and transferred to the stopped flow with a gas-tight Hamilton syringe. In the experiments containing NRPS, samples were prepared as described for NikQ, but with 50 µM L-His-NikP1 added. Oxygen-saturated buffers were prepared by bubbling 50 mM HEPES with O_2 gas on ice for at least 20 minutes. Desired O_2 concentrations were prepared by mixing O_2-saturated buffer with N_2-degassed buffer using a Hamilton syringe. Measurements were collected at 4 °C using photodiode array (PDA) detection. Single wavelength time traces

at 443 nm were extracted from the data, as this wavelength displayed the maximum difference in absorption between ferrous (Fe^{2+}), oxygen bound (Fe^{2+}-O_2) and autoxidized ferric (Fe^{3+}) low-spin forms. The 443 nm traces were fit to a two-summed exponential expression using Applied Photophysics Pro-Data SX software according to Equation 1 below, where $k_{1,obs}$ is the observed formation rate of the oxy-intermediate, and k_2 is the autoxidation rate. Both are in units of s^{-1} under pseudo-first order conditions.

$$Fe^{2+} + O_2 \xrightarrow{k_{1,obs}} Fe^{2+}\text{-}O_2 \xrightarrow{k_2} Fe^{3+} + O_2^{\cdot -}$$

The bimolecular rate constant for O_2 binding was determined by repeating the experiment at several O_2 concentrations under pseudo-first order conditions and plotting $k_{1,obs}$ (s^{-1}) as a function of O_2. The slope yields the bimolecular rate constant (M^{-1} s^{-1}) for dioxygen binding, and the y-intercept (equal to zero) indicates that the formation of the oxy-ferrous complex is essentially irreversible. When the autoxidation rate constant (k_2), was plotted as a function of O_2, no appreciable dependence was observed, as expected due to the irreversibility of this step.

3.5.10 Phosphopantetheinylation Assay

The boron-dipyrromethene (Bodipy) coenzyme A derivative was synthesized using published procedures[53] and stored at -20 °C until further use. Concentrations were determined using an extinction coefficient of $\varepsilon_{504\ nm}$ = 68 mM^{-1} cm^{-1}. Phosphopantetheinylation reactions (500 µL total volume) consisted of 40 µM Bodipy-CoA and 20 µM *apo*-NikP1 in a buffer containing 50 mM HEPES pH 8.1, 500 mM NaCl, and 10 mM $MgCl_2$. For reactions containing NikQ, the P450 was added to a final concentration of 100 µM. Reactions were initiated by the addition of Sfp (100 nM) and 20 µL aliquots were quenched with 10 µL SDS-loading buffer at various time points and

incubated at 85 °C for 5 minutes. Samples were run on a 12.5% SDS-PAGE gel and imaged using a Typhoon FLA 7000 imager using an excitation wavelength of 473 nm, a 520 nm filter, and a PMT detection of 650 V.

3.6 Acknowledgements

We thank M. Walla and W. Cotham at the USC Mass Spectrometry center for their assistance in analyzing NRPS samples. We thank Prof. C. Aldrich for providing the plasmids for Sfp co- and over-expression, and Prof. J. Sodetz for his assistance in the analytical SEC measurements. This work was supported by National Science Foundation CAREER grant 1555066 and an ASPIRE grant from the USC Vice President of Research to T.M.M..

3.7 REFERENCES

1. Cane, D. E.; Walsh, C. T.; Khosla, C., Biochemistry - Harnessing the biosynthetic code: Combinations, permutations, and mutations. *Science* **1998,** *282* (5386), 63-68.
2. Fischbach, M. A.; Walsh, C. T., Assembly-line enzymology for polyketide and nonribosomal peptide antibiotics: Logic, machinery, and mechanisms. *Chem. Rev.* **2006,** *106* (8), 3468-3496.
3. Marahiel, M. A.; Stachelhaus, T.; Mootz, H. D., Modular Peptide Synthetases Involved in Nonribosomal Peptide Synthesis. *Chem. Rev.* **1997,** *97* (7), 2651-2674.
4. Finking, R.; Marahiel, M. A., Biosynthesis of nonribosomal peptides. *Annu. Rev. Microbiol.* **2004,** *58*, 453-488.
5. Lin, S.; Huang, T.; Shen, B., Tailoring enzymes acting on carrier protein-tethered substrates in natural product biosynthesis. *Methods Enzymol.* **2012,** *516*, 321-43.
6. Walsh, C. T.; Chen, H. W.; Keating, T. A.; Hubbard, B. K.; Losey, H. C.; Luo, L. S.; Marshall, C. G.; Miller, D. A.; Patel, H. M., Tailoring enzymes that modify nonribosomal peptides during and after chain elongation on NRPS assembly lines. *Curr. Opin. Chem. Biol.* **2001,** *5* (5), 525-534.
7. Bischoff, D.; Pelzer, S.; Bister, B.; Nicholson, G. J.; Stockert, S.; Schirle, M.; Wohlleben, W.; Jung, G.; Sussmuth, R. D., The biosynthesis of vancomycin-type glycopeptide antibiotics - The order of the cyclization steps. *Angew. Chem.* **2001,** *40* (24), 4688-4691.
8. Cryle, M. J.; Meinhart, A.; Schlichting, I., Structural Characterization of OxyD, a Cytochrome P450 Involved in beta-Hydroxytyrosine Formation in Vancomycin Biosynthesis. *J Biol Chem* **2010,** *285* (32), 24562-24574.

9. Woithe, K.; Geib, N.; Zerbe, K.; Li, D. B.; Heck, M.; Fournier-Rousset, S.; Meyer, O.; Vitali, F.; Matoba, N.; Abou-Hadeed, K.; Robinson, J. A., Oxidative phenol coupling reactions catalyzed by OxyB: A cytochrome p450 from the vancomycin producing organism. Implications for vancomycin biosynthesis. *J Am Chem Soc* **2007,** *129* (21), 6887-6895.
10. Chen, H.; Hubbard, B. K.; O'Connor, S. E.; Walsh, C. T., Formation of beta-hydroxy histidine in the biosynthesis of nikkomycin antibiotics. *Chemistry & biology* **2002,** *9* (1), 103-12.
11. Rivera, H.; Dhar, S.; La Clair, J. J.; Tsai, S. C.; Burkart, M. D., An unusual intramolecular trans-amidation. *Tetrahedron* **2016,** *72* (25), 3605-3608.
12. Singh, G. M.; Fortin, P. D.; Koglin, A.; Walsh, C. T., beta-Hydroxylation of the Aspartyl Residue in the Phytotoxin Syringomycin E: Characterization of Two Candidate Hydroxylases AspH and SyrP in Pseudomonas syringae. *Biochemistry-Us* **2008,** *47* (43), 11310-11320.
13. Uhlmann, S.; Sussmuth, R. D.; Cryle, M. J., Cytochrome p450sky interacts directly with the nonribosomal peptide synthetase to generate three amino acid precursors in skyllamycin biosynthesis. *ACS chemical biology* **2013,** *8* (11), 2586-96.
14. Haslinger, K.; Brieke, C.; Uhlmann, S.; Sieverling, L.; Sussmuth, R. D.; Cryle, M. J., The structure of a transient complex of a nonribosomal peptide synthetase and a cytochrome P450 monooxygenase. *Angewandte Chemie* **2014,** *53* (32), 8518-22.

15. Kokona, B.; Winesett, E. S.; von Krusenstiern, A. N.; Cryle, M. J.; Fairman, R.; Charkoudian, L. K., Probing the selectivity of beta-hydroxylation reactions in non-ribosomal peptide synthesis using analytical ultracentrifugation. *Anal Biochem* **2016,** *495*, 42-51.
16. Matthews, M. L.; Krest, C. M.; Barr, E. W.; Vaillancourt, F. H.; Walsh, C. T.; Green, M. T.; Krebs, C.; Bollinger, J. M., Substrate-triggered formation and remarkable stability of the C-H bond-cleaving chloroferryl intermediate in the aliphatic halogenase, SyrB2. *Biochemistry* **2009,** *48* (20), 4331-43.
17. Brieke, C.; Peschke, M.; Haslinger, K.; Cryle, M. J., Sequential In Vitro Cyclization by Cytochrome P450 Enzymes of Glycopeptide Antibiotic Precursors Bearing the X-Domain from Nonribosomal Peptide Biosynthesis. *Angew. Chem. Int. Ed. Engl.* **2015,** *54* (52), 15715-15719.
18. Haslinger, K.; Peschke, M.; Brieke, C.; Maximowitsch, E.; Cryle, M. J., X-domain of peptide synthetases recruits oxygenases crucial for glycopeptide biosynthesis. *Nature* **2015,** *521* (7550), 105-U271.
19. Peschke, M.; Haslinger, K.; Brieke, C.; Reinstein, J.; Cryle, M. J., Regulation of the P450 Oxygenation Cascade Involved in Glycopeptide Antibiotic Biosynthesis. *J Am Chem Soc* **2016,** *138* (21), 6746-6753.
20. Koglin, A.; Mofid, M. R.; Lohr, F.; Schafer, B.; Rogov, V. V.; Blum, M. M.; Mittag, T.; Marahiel, M. A.; Bernhard, F.; Dotsch, V., Conformational switches modulate protein interactions in peptide antibiotic synthetases. *Science* **2006,** *312* (5771), 273-276.

21. Reger, A. S.; Carney, J. M.; Gulick, A. M., Biochemical and crystallographic analysis of substrate binding and conformational changes in Acetyl-CoA synthetase. *Biochemistry* **2007,** *46* (22), 6536-6546.

22. Reger, A. S.; Wu, R.; Dunaway-Mariano, D.; Gulick, A. M., Structural characterization of a 140 degrees domain movement in the two-step reaction catalyzed by 4-Chlorobenzoate : CoA ligase. *Biochemistry* **2008,** *47* (31), 8016-8025.

23. Weber, T.; Baumgartner, R.; Renner, C.; Marahiel, M. A.; Holak, T. A., Solution structure of PCP, a prototype for the peptidyl carrier domains of modular peptide synthetases. *Structure* **2000,** *8* (4), 407-418.

24. Mitchell, C. A.; Shi, C.; Aldrich, C. C.; Gulick, A. M., Structure of PA1221, a Nonribosomal Peptide Synthetase Containing Adenylation and Peptidyl Carrier Protein Domains. *Biochemistry* **2012,** *51* (15), 3252-3263.

25. Sundlov, J. A.; Shi, C.; Wilson, D. J.; Aldrich, C. C.; Gulick, A. M., Structural and Functional Investigation of the Intermolecular Interaction between NRPS Adenylation and Carrier Protein Domains. *Chem. Biol.* **2012,** *19* (2), 188-198.

26. Drake, E. J.; Miller, B. R.; Shi, C.; Tarrasch, J. T.; Sundlov, J. A.; Allen, C. L.; Skiniotis, G.; Aldrich, C. C.; Gulick, A. M., Structures of two distinct conformations of holo-non-ribosomal peptide synthetases. *Nature* **2016,** *529* (7585), 235-238.

27. Tanovic, A.; Samel, S. A.; Essen, L. O.; Marahiel, M. A., Crystal structure of the termination module of a nonribosomal peptide synthetase. *Science* **2008,** *321* (5889), 659-663.

28. Drake, E. J.; Cao, J.; Qu, J.; Shah, M. B.; Straubinger, R. M.; Gulick, A. M., The 1.8 A crystal structure of PA2412, an MbtH-like protein from the pyoverdine cluster of Pseudomonas aeruginosa. *J. Biol. Chem.* **2007,** *282* (28), 20425-20434.

29. Felnagle, E. A.; Barkei, J. J.; Park, H.; Podevels, A. M.; McMahon, M. D.; Drott, D. W.; Thomas, M. G., MbtH-Like Proteins as Integral Components of Bacterial Nonribosomal Peptide Synthetases. *Biochemistry* **2010,** *49* (41), 8815-8817.

30. Herbst, D. A.; Boll, B.; Zocher, G.; Stehle, T.; Heide, L., Structural Basis of the Interaction of MbtH-like Proteins, Putative Regulators of Nonribosomal Peptide Biosynthesis, with Adenylating Enzymes. *J. Biol. Chem.* **2013,** *288* (3), 1991-2003.

31. Zhang, W. J.; Ostash, B.; Walsh, C. T., Identification of the biosynthetic gene cluster for the pacidamycin group of peptidyl nucleoside antibiotics. *Proc. Natl. Acad. Sci. USA* **2010,** *107* (39), 16828-16833.

32. Makris, T. M.; Knoot, C. J.; Wilmot, C. M.; Lipscomb, J. D., Structure of a Dinuclear Iron Cluster-Containing beta-Hydroxylase Active in Antibiotic Biosynthesis. *Biochemistry* **2013,** *52* (38), 6662-6671.

33. Makris, T. M.; Chakrabarti, M.; Munck, E.; Lipscomb, J. D., A family of diiron monooxygenases catalyzing amino acid beta-hydroxylation in antibiotic biosynthesis. *Proc. Natl. Acad. Sci. USA* **2010,** *107* (35), 15391-15396.

34. Neary, J. M.; Powell, A.; Gordon, L.; Milne, C.; Flett, F.; Wilkinson, B.; Smith, C. P.; Micklefield, J., An asparagine oxygenase (AsnO) and a 3-hydroxyasparaginyl phosphotransferase (HasP) are involved in the biosynthesis of calcium-dependent lipopeptide antibiotics. *Microbiology-Sgm* **2007,** *153*, 768-776.

35. Strieker, M.; Nolan, E. M.; Walsh, C. T.; Marahiel, M. A., Stereospecific Synthesis of threo- and erythro-beta-Hydroxyglutamic Acid During Kutzneride Biosynthesis. *J. Am. Chem. Soc.* **2009,** *131* (37), 13523-13530.

36. Cryle, M. J.; Staaden, J.; Schlichting, I., Structural characterization of CYP165D3, a cytochrome P450 involved in phenolic coupling in teicoplanin biosynthesis. *Arch. Biochem. Biophys.* **2011,** *507* (1), 163-173.

37. Conner, K. P.; Cruce, A. A.; Krzyaniak, M. D.; Schimpf, A. M.; Frank, D. J.; Ortiz de Montellano, P.; Atkins, W. M.; Bowman, M. K., Drug modulation of water-heme interactions in low-spin P450 complexes of CYP2C9d and CYP125A1. *Biochemistry* **2015,** *54* (5), 1198-207.

38. Conner, K. P.; Schimpf, A. M.; Cruce, A. A.; McLean, K. J.; Munro, A. W.; Frank, D. J.; Krzyaniak, M. D.; de Montellano, P. O.; Bowman, M. K.; Atkins, W. M., Strength of Axial Water Ligation in Substrate-Free Cytochrome P450s Is Isoform Dependent. *Biochemistry* **2014,** *53* (9), 1428-1434.

39. Conner, K. P.; Vennam, P.; Woods, C. M.; Krzyaniak, M. D.; Bowman, M. K.; Atkins, W. M., 1,2,3-Triazole-Heme Interactions in Cytochrome P450: Functionally Competent Triazole-Water-Heme Complexes. *Biochemistry* **2012,** *51* (32), 6441-6457.

40. Batabyal, D.; Lewis-Ballester, A.; Yeh, S. R.; Poulos, T. L., A Comparative Analysis of the Effector Role of Redox Partner Binding in Bacterial P450s. *Biochemistry* **2016,** *55* (47), 6517-6523.

41. Sligar, S. G.; Gunsalus, I. C., A thermodynamic model of regulation: modulation of redox equilibria in camphor monoxygenase. *Proc. Natl. Acad. Sci. USA* **1976,** *73* (4), 1078-82.

42. Tagawa, K.; Arnon, D. I., Oxidation-Reduction Potentials and Stoichiometry of Electron Transfer in Ferredoxins. *Biochim. Biophys. Acta* **1968,** *153* (3), 602-&.

43. Jasniewski, A. J.; Knoot, C. J.; Lipscomb, J. D.; Que, L., A Carboxylate Shift Regulates Dioxygen Activation by the Diiron Nonheme beta-Hydroxylase CmIA upon Binding of a Substrate-Loaded Nonribosomal Peptide Synthetase. *Biochemistry* **2016,** *55* (41), 5818-5831.

44. Ost, T. W. B.; Clark, J.; Mowat, C. G.; Miles, C. S.; Walkinshaw, M. D.; Reid, G. A.; Chapman, S. K.; Daff, S., Oxygen activation and electron transfer in flavocytochrome P450BM3. *J. Am. Chem. Soc.* **2003,** *125* (49), 15010-15020.

45. Edwards, D. J.; Gerwick, W. H., Lyngbyatoxin biosynthesis: Sequence of biosynthetic gene cluster and identification of a novel aromatic prenyltransferase. *J. Am. Chem. Soc.* **2004,** *126* (37), 11432-11433.

46. Huynh, M. U.; Elston, M. C.; Hernandez, N. M.; Ball, D. B.; Kajiyama, S.; Irie, K.; Gerwick, W. H.; Edwards, D. J., Enzymatic Production of (-)-Indolactam V by LtxB, a Cytochrome P450 Monooxygenase. *J. Nat. Prod.* **2010,** *73* (1), 71-74.

47. Quadri, L. E. N.; Weinreb, P. H.; Lei, M.; Nakano, M. M.; Zuber, P.; Walsh, C. T., Characterization of Sfp, a Bacillus subtilis phosphopantetheinyl transferase for peptidyl carrier protein domains in peptide synthetases. *Biochemistry* **1998,** *37* (6), 1585-1595.

48. Berry, E. A.; Trumpower, B. L., Simultaneous Determination of Hemes-a, Hemes-B, and Hemes-C from Pyridine Hemochrome Spectra. *Anal. Biochem.* **1987,** *161* (1), 1-15.

49. Artimo, P.; Jonnalagedda, M.; Arnold, K.; Baratin, D.; Csardi, G.; de Castro, E.; Duvaud, S.; Flegel, V.; Fortier, A.; Gasteiger, E.; Grosdidier, A.; Hernandez, C.;

Ioannidis, V.; Kuznetsov, D.; Liechti, R.; Moretti, S.; Mostaguir, K.; Redaschi, N.; Rossier, G.; Xenarios, I.; Stockinger, H., ExPASy: SIB bioinformatics resource portal. *Nucleic Acids Res.* **2012,** *40* (Web Server issue), W597-603.

50. Morrison, J. F., Kinetics of Reversible Inhibition of Enzyme-Catalysed Reactions by Tight-Binding Inhibitors. *Biochim. Biophys. Acta* **1969,** *185* (2), 269-&.
51. Watanabe, T.; Honda, K., Measurement of the Extinction Coefficient of the Methyl Viologen Cation Radical and the Efficiency of Its Formation by Semiconductor Photocatalysis. *J. Phys. Chem.* **1982,** *86* (14), 2617-2619.
52. Wilson, G. S.; Tsibris, J. C. M.; Gunsalus, I. C., Electrochemical Studies of Putidaredoxin and Its Selenium Analog. *J. Biol. Chem.* **1973,** *248* (17), 6059-6061.
53. La Clair, J. J.; Foley, T. L.; Schegg, T. R.; Regan, C. M.; Burkart, M. D., Manipulation of carrier proteins in antibiotic biosynthesis. *Chem. Biol.* **2004,** *11* (2), 195-201.
54. Das, A.; Grinkova, Y. V.; Sligar, S. G., Redox potential control by drug binding to cytochrome p450 3A4. *J. Am. Chem. Soc.* **2007,** *129* (45), 13778-+.
55. Denisov, I. G.; Grinkova, Y. V.; Baas, B. J.; Sligar, S. G., The ferrous-dioxygen intermediate in human cytochrome P450 3A4 - Substrate dependence of formation and decay kinetics. *J. Biol. Chem.* **2006,** *281* (33), 23313-23318.
56. Eisenstein, L.; Debey, P.; Douzou, P., P450cam - Oxygenated Complexes Stabilized at Low-Temperature. *Biochem. Biophys. Res. Commun.* **1977,** *77* (4), 1377-1383.
57. Gunsalus, I. C.; Sligar, S. G., Redox regulation of cytochrome P450cam mixed function oxidation by putidaredoxin and camphor ligation. *Biochimie* **1976,** *58* (1-2), 143-7.

58. Peterson, J. A.; Ishimura, Y.; Griffin, B. W., Pseudomonas-Putida Cytochrome-P-450 - Characterization of an Oxygenated Form of Hemoprotein. *Arch. Biochem. Biophys.* **1972,** *149* (1), 197-&.

59. Sevrioukova, I. F.; Peterson, J. A., Reaction of Carbon-Monoxide and Molecular-Oxygen with P450terp (Cyp108) and P450bm-3 (Cyp102). *Arch. Biochem. Biophys.* **1995,** *317* (2), 397-404.

60. Lambeth, J. D.; Kriengsiri, S., Cytochrome-P-450scc-Adrenodoxin Interactions - Ionic Effects on Binding, and Regulation of Cytochrome Reduction by Bound Steroid Substrates. *J. Biol. Chem.* **1985,** *260* (15), 8810-8816.

61. Tuckey, R. C.; Kamin, H., The Oxyferro Complex of Purified Adrenal Cytochrome P-450scc. *Federation Proceedings* **1982,** *41* (4), 1405-1405.

62. Kashem, M. A.; Dunford, H. B., The Formation and Decay of the Oxyferrous Complex of Beef Adrenocortical Cytochrome P-450scc. Rapid-Scan and Stopped-Flow Studies. *Biochem. Cell Biol.* **1987,** *65* (5), 486-492.

63. Yeh, H. C.; Hsu, P. Y.; Tsai, A. L.; Wang, L. H., Spectroscopic characterization of the oxyferrous complex of prostacyclin synthase in solution and in trapped sol-gel matrix. *FEBS J.* **2008,** *275* (9), 2305-2314.

64. Bui, S. H.; McLean, K. J.; Cheesman, M. R.; Bradley, J. M.; Rigby, S. E. J.; Levy, C. W.; Leys, D.; Munro, A. W., Unusual Spectroscopic and Ligand Binding Properties of the Cytochrome P450-Flavodoxin Fusion Enzyme XplA. *J. Biol. Chem.* **2012,** *287* (23), 19699-19714.

CHAPTER 4

Sterics Proximal to the Heme of Carrier Protein-Modifying Cytochrome P450 NikQ Protect Against Inhibitory Substrate Ligation

4.1 ABSTRACT

Mutations to the atypically bulky residues at the 338 and 345 positions proximal to the heme-iron cofactor of P450 tailoring enzyme NikQ have yielded variants, I338G and I338GI345G with altered ligand-binding properties. NikQ performs a β-hydroxylation reaction on an L-histidine residue requisitely tethered to NikP1 (L-his-NikP1), a nonribosomal peptide synthetase, for the biosynthesis of Nikkomycin X antibiotics. Both mutants show L-histidine ligation by the P450 iron in substrate and ligand binding studies using optical and electron paramagnetic resonance spectroscopies. The double mutant in particular exhibits a substantial increase in affinity for the small molecule imidazole, which closely resembles the L-his substrate and a propensity to bind free L-his that is not observed in the wild-type enzyme or the single mutant. Reduction attempts with L-his-NikP1-bound I338GI345G have failed to yield the expected pentacoordinate ferrous geometry, instead resulting in a mixture of nitrogen-ligated hexacoordinate ferrous P450 and seemingly inactivated enzyme. As such, attempts to form the ferric-superoxide intermediate necessary for catalysis have proven unsuccessful in this substrate-bound variant, implicating chemical inhibition through substrate-ligation. These results, alongside those confirming cyanide-ligand displacement by substrate in the mutants, indicate that these unusual isoleucines proximal to the NikQ heme may function in a manner that protects the enzyme against ligation of the protein-tethered substrate L-histidine residue.

4.2 INTRODUCTION

Cytochrome P450 (CYP) NikQ β-hydroxylates a protein-tethered L-histidine residue in the biosynthesis of nikkomycin X antibiotics.[1] CYP reactivity is dependent on a thiolate-ligated heme-iron cofactor and requires one equivalent of O_2, two protons, and two electrons to carry out activation of relatively inert C-H bonds.[2] A vast majority of the mechanistic work on P450s has been on enzymes that catalyze hydroxylation reactions on small molecule substrates.[3, 4] In contrast, the L-his-NikP1 substrate of NikQ is a large 75 kDa nonribosomal peptide synthetase (NRPS) protein. This NRPS has been post-translationally modified at a conserved serine residue by linkage to a phosphopantetheinyl (ppant) group, which forms a thioester bond with the L-histidine (his) target that NikQ acts upon.[1, 5] Previous work on wild-type (WT) NikQ, summarized in Figure 4.1, has demonstrated a unique mode of catalytic regulation by its cognate substrate.[5] However, comparable studies regarding the role of the NRPS substrate on P450 mechanism are extremely limited in the literature.[4] This partially owes to complexities intrinsic to NRPS proteins.[6]

Typically in P450 catalysis, the presence of substrate induces significant thermodynamic and kinetic changes that influence the reactivity of several P450 cycle intermediates.[7-9] L-His-NikP1, however, appears to exert virtually no influence on NikQ catalysis.[5] In particular, WT-NikQ does not exhibit the structural changes upon substrate binding that correspond to a reconfiguration of the heme-iron d-electrons from the 6-coordinate, ferric-aquo low-spin form to the 5-coordinate high-spin state.[5] This spin shift gates the next catalytic step, a one-electron transfer from a redox partner protein, often a ferredoxin, with reduction potential poised between that of the low-spin enzyme and the

more-positive E° of the high-spin form.[9] This thermodynamic regulation serves to prevent consumption of NAD(P)H by an enzyme that lacks the target substrate, as NAD(P)H is an expensive commodity in the energetic currency of the cell and uncoupling leads the generation of deleterious reactive oxygen species (ROS). Indeed, measurements of the NikQ-WT redox potential in the absence and presence of L-his-NikP1 show no alteration to the cofactor E°, with the value being unusually low for a CYP at ~ -415 mV.[5] This is problematic not only from the standpoint of catalytic regulation, but also in regards to reconstitution of a viable turnover system, as most bacterial redox systems do not possess potentials sufficiently negative for favorable reduction of NikQ.

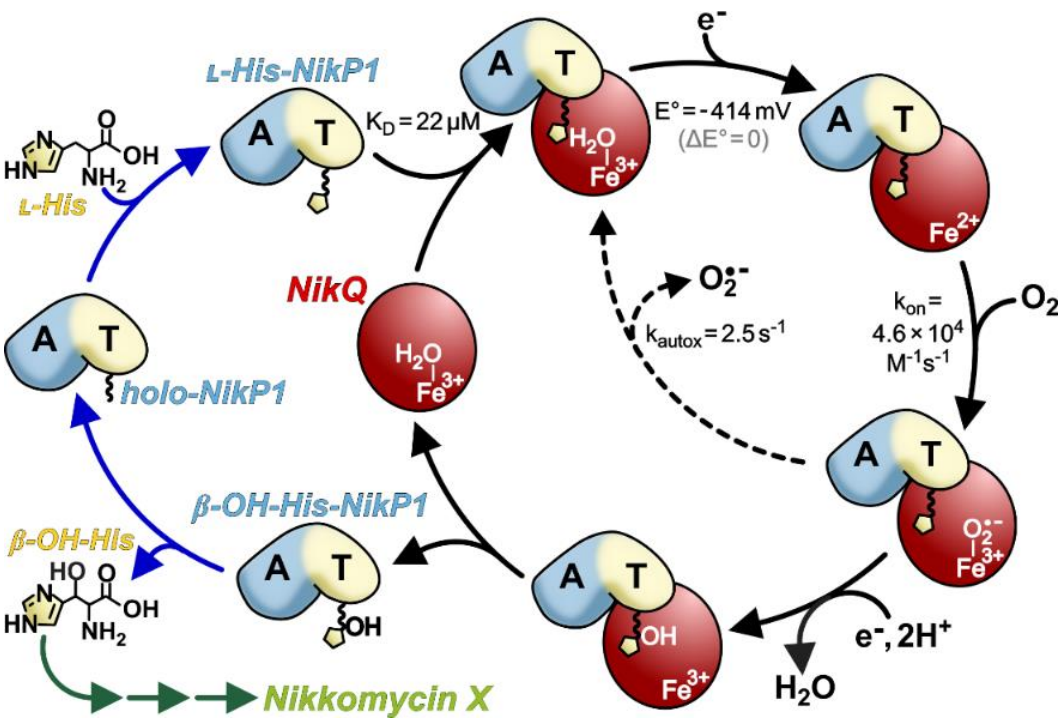

Figure 4.1. A summary of the influence of the L-his-NikP1 substrate on the early steps of NikQ catalysis.[5] The tailoring enzyme binds the loaded NRPS with a dissociation constant of 22 μM, yielding a stable protein-protein complex. Notably, the NikQ reduction potential is atypically low for a CYP, and the autoxidation rate is quite fast. Further, there is no change in the potential of the heme-iron in the substrate-free versus -bound P450, nor is the ferric-superoxide intermediate stabilized by the presence of excess L-his-NikP1.

Following the first electron transfer event in CYP catalysis, atmospheric oxygen ligates the ferrous heme-iron to yield a ferric-superoxide intermediate, colloquially referred to as the *oxy-complex*.[3] Decay of this species can occur through two different pathways, signifying a critical branch-point between uncoupling via superoxide release and productive continuation through the P450 cycle by means of a second reduction, which is classically the rate-limiting step in CYP turnover.[10] Therefore, stability of the dioxygen adduct is paramount to maintaining a coupled and efficient process, as an impaired rate of autoxidation allows time for the slow transfer of a second electron from the ferredoxin. In the presence of substrate, autoxidation is typically at least an order of magnitude slower than in the substrate-free P450.[8, 11-13] This kinetic safeguard against uncoupling, however, is also lacking in WT-NikQ, as there is no appreciable change in autoxidation rate in the absence versus the presence of excess L-his-NikP1.[5] Further, the autoxidation rate constant of ~2.5 s^{-1} is fast even for the superoxide-release of a substrate-free CYP.[5]

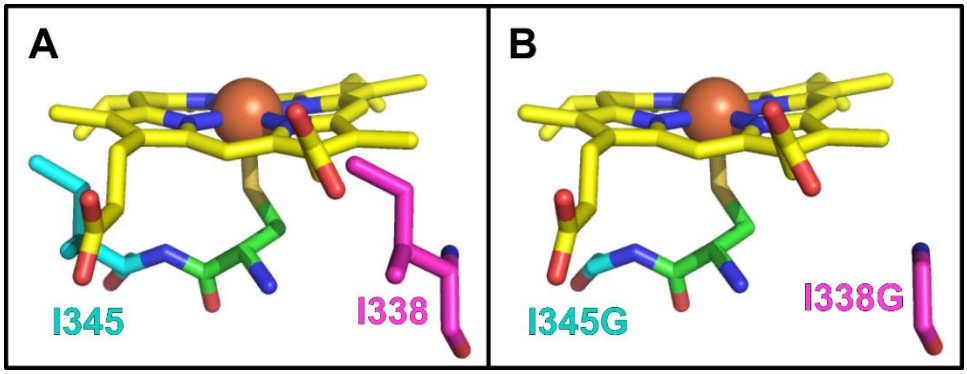

Figure 4.2. The 338 and 345 positions proximal to the NikQ heme. A model of the region proximal to the NikQ heme was generated in SwissModel[47-49] using the PDB 4PWV structure of P450Sky[50] (the most homologous crystallized CYP to NikQ in the Protein Data Bank) as a template. NikQ-WT (**A**) features bulky isoleucine residues at the 338 and 345 positions. Two NikQ variants have been generated, one with a glycine substituted for I338, and another (**B**) with both isoleucines mutated to glycine residues.

Taken together, the lack of regulation by substrate in cytochrome P450 NikQ raises mechanistic questions regarding the functional purpose of this absence of catalytic gating, as well as the molecular determinants that give rise to it. Given the ability of the region proximal to the heme to modulate enzyme spin equilibria, reactivity, and electronics,[14-25] we directed our attentions to analysis of the residues surrounding the NikQ thiolate ligand. Homology analysis, shown in Table 4.1, of P450s known to act on carrier protein-bound substrates revealed that residues at positions -6 and +1 relative to the cys-thiolate (set as position 0 for standardization of amino acid numbering) are typically glycine or leucine respectively. These positions in NikQ correspond to dual isoleucines at residues 338 and 345, highlighted in a homology model in Figure 4.2. We were only able to find one other instance of this unusual combination in our analysis, which exists in an ortholog with near-100% identity to NikQ that also acts on an NRPS-tethered histidine in another nikkomycin biosynthetic pathway.[8, 26] To determine whether these proximal sterics may contribute to the absence of mechanistic regulation by substrate in NikQ, we eliminated any side-chain bulk at these positions by mutating each of these two isoleucine to a glycine. Substrate and ligand-binding studies of the resulting I338G and I338GI345G NikQ variants were carried out via electron paramagnetic resonance (EPR) and electronic absorption spectroscopies alongside rapid-mix kinetics and equilibrium methodologies. Our results indicate that I338 may contribute to the lack of substrate-mediated influence on catalysis in WT-NikQ, as the I338G variant demonstrates stabilization of the dioxygen intermediate when bound to L-his-NikP1. Further, both I338 and I345 appear to play a critical role in preventing inhibitory ligation of the histidine substrate by the heme-iron, with the single and double mutants exhibiting some degree of nitrogen ligation when bound to L-his-NikP1. In the case of

I338GI345G, total ligation is suggested by the optical spectra and the inhibitory nature implied by an inability to form the 5-coordinate ferrous P450 and related difficulties in obtaining a dioxygen-bound form of this mutant.

Table 4.1. Sequence alignment of amino acids around the cysteine-derived thiolate ligand in P450 hydroxylases acting on carrier protein-tethered substrates. Unless otherwise specified via superscript, CYPs listed below β-hydroxylate the target substrate.

P450	Substrate	Carrier Protein	Position Relative to Thiolate-Cys										Ref.
			-7	-6	-5	-4	-3	-2	-1	0	+1	+2	
NikQ	L-his-PCP	NikP1	F	I	Q	G	N	H	Y	C	I	G	1
SanQ	L-his-PCP	SanO	F	I	Q	G	N	H	Y	C	I	G	26
AcmG8[a]	L-thr-PCP	$AcmG10_1$	F	G	H	G	V	H	F	C	L	G	27
Ecm12	L-trp-PCP	Ecm13	F	G	H	G	P	H	F	C	V	G	28
TrsB	L-trp-PCP	TrsR	F	G	H	G	P	H	F	C	V	G	29
TioI	L-trp-PCP	TioK	F	G	H	G	P	H	F	C	L	G	30
Swb13	L-trp-PCP	Swb11	F	G	H	G	P	H	F	C	V	G	30
Qui15	L-trp-PCP	Qui18	F	G	H	G	P	H	F	C	V	G	31
FmoC	L-trp-PCP	FmoA1	F	G	H	G	R	H	L	C	L	G	32
NovI	L-tyr-PCP	NovH	F	A	Y	G	S	H	Y	C	L	G	33
CloI	L-tyr-PCP	CloH	F	A	Y	G	S	H	Y	C	L	G	34
SimI[b]	L-tyr-PCP	SimH[c]	F	A	F	G	S	H	F	C	L	G	35
CouI[d]	L-tyr-PCP	CouH[e]	F	A	Y	G	S	H	Y	C	L	G	36
$OxyD_{Bal}$	L-tyr-PCP	BpsD	F	G	H	G	M	H	H	C	L	G	37
$P450_{Sky}$	L-leu-PCP L-phe-PCP OMe-tyr-PCP	$Sky31_{11}$ $Sky30_5$ $Sky30_7$	F	G	Y	G	P	H	F	C	L	G	38, 39
ZbmVIIc	L-val-PCP	ZbmVIIb	F	G	Y	G	P	H	Y	C	L	G	40
SalD	L-CHA[f]-PCP	SalB	F	G	H	G	P	H	Y	C	I	G	41
BioI[g]	Acyl-ACP	ACP	F	G	H	G	H	H	V	C	L	G	42
SamR0478[h]	Acyl-ACP	PKS	F	S	A	G	I	H	F	C	L	G	43, 44
SamR0479[i]	Acyl-ACP	PKS	F	S	A	G	P	H	F	C	L	G	43, 44
AufB[j]	Acyl-ACP	PKS	F	G	Y	G	S	H	T	C	F	G	45
CalO2[k]	orsellinyl-ACP	CalO5	F	G	A	G	M	R	Y	C	L	G	46

Chemistries other than β-hydroxylation: [a]γ-hydroxylation, [g]hydroxylation and C-C cleavage, [h]C28-hydroxylation, [i]C50-hydroxylation, [j]C2-hydroxylation, [k]hydroxylation
Alternative protein names: [b]SimD1, [c]SimD6, [d]CumD, [e]CumC
Substrate abbreviations: [f]CHA = 3-cyclohex-2'-enylalanine

4.3 Results and Discussion

4.3.1 Expression, purification, and verification of thiolate-ligand and substrate-binding

Both the I338G single mutant and the I338GI345G double mutant express in high yields (≥60 mg P450 per liter culture), though this is only achieved in the latter upon co-expression with chaperones to promote proper folding. These variants were deemed ~90% pure following a two-column purification, with $A_{419\ nm}/A_{280\ nm} \geq 1.60$. Multiple attempts were made to express the I345G single mutant with and without the heme-importer ChuA and various chaperone suites in conjunction with changes to induction temperatures, IPTG concentrations, and expression times. However, all resulting yields were extremely low (≤2 mg protein per liter culture) following Ni-NTA chromatography, and negligible after a necessary second column.

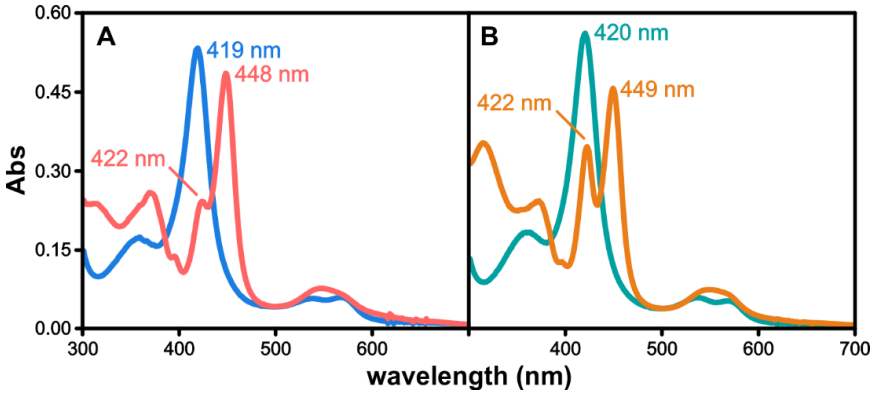

Figure 4.3. Verification of the proximal thiolate ligand in the NikQ mutants via CO-binding. Carbonmonoxy-ferrous spectra of NikQ-I338G (**A**, pink) and NikQ-I338GI345G (**B**, gold) confirm that the cysteine-derived thiolate ligand is intact following addition of chemical reductant to the anaerobic substrate-free enzyme (single mutant in light blue and double mutant in teal) in a sealed, CO-sparged cuvette.

UV-visible spectroscopy of the as-purified I338G and I338GI345G NikQ mutants showed spectra characteristic of low-spin, water-ligated, ferric cytochrome P450s. Thiolate ligation was verified for the I338G and I338GI345G variants of NikQ by optical analysis of the ferrous-carbonmonoxy adduct. Upon addition of reductant, shift of the Soret maxima to ~445-450 nm was observed for both mutants (Figure 4.3), signifying intact Cys-Fe proximal ligation through coordination of the ferrous cytochrome to CO at the distal position.

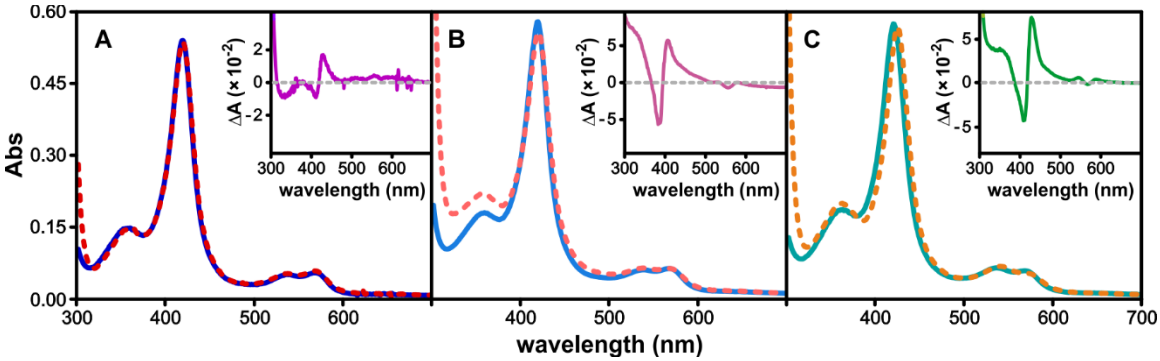

Figure 4.4. Electronic absorption spectra of the NikQ variants in the absence and presence of 10 equivalents of L-his-NikP1 substrate. NikQ-WT (**A**) exhibits a negligible change in optical properties upon the addition of substrate (dashed red spectrum) to the as-purified form (dark blue spectrum), with Soret maximum remaining at 418 nm. The I338G mutant (**B**) undergoes a slight type-II spectral change from the substrate-free form at 418 nm (light blue spectrum) to 421 nm upon incubation with L-his-NikP1 (dashed pink spectrum). NikQ-I338GI345G (**C**) also experiences a bathochromic Soret shift upon substrate-binding from an initial 420 nm (teal spectrum) to 424 nm (dashed gold spectrum). Spectra of the bound-P450s have been mathematically corrected for scattering (which derived from the NRPS protein). Difference spectra are shown in the insets.

The as-purified I338G variant, shown in Figure 4.4 B in light blue, was spectroscopically indistinguishable from NikQ-WT (dark blue spectrum in Figure 4.4 A), exhibiting Soret maximum at 419 nm and β and α Q-bands at ~535 and ~580 nm, with the latter α Q-band being slightly more pronounced than the β band. The Soret of the as-purified double mutant (Figure 4.4 C, teal spectrum) was centered at 420 nm, with Q-bands

at ~535 and ~580 nm, although the β Q-band of this variant is enhanced relative to the α band. This may indicate a small percent of the I338GI345G mutant remains imidazole-ligated from Ni-NTA column elution even after purification using another chromatographic method, as the red-shifted Soret and β Q-band enhancement is consistent with nitrogen-ligation in P450s.[51]

Upon addition of excess L-his-NikP1 substrate, both mutants exhibit type-II binding spectra consistent with some degree of nitrogen-ligation, likely to the imidazole moiety of the substrate histidine, featuring red-shifted Soret, reduced extinction relative to the resting state, and enhanced β Q-band intensity.[51] The single mutant (pink spectrum of Figure 4.4 B) appears to remain partially water-ligated, as with substrate-bound NikQ-WT shown in the red spectrum of Figure 4.4 A, with only a small fraction of this mutant coordinating the NikP1-tethered histidine to yield a 421 nm Soret. The double-mutant, however, appears to fully ligate the L-his R-group, with Soret at 424 nm. These changes should theoretically allow for determination of a dissociation constant via optical substrate-binding titration. Attempts at this have proven unsuccessful, however, due to the modest absorbance change (ie. a ~2 nm shift to a species with a subtle decrease in Soret extinction) in the single mutant and persistent scattering of the NRPS protein that interferes with the spectrum of both mutants.

Size exclusion chromatography was used to confirm the ability of the NikQ mutants to form a stable complex with L-his-NikP1, as has been observed in WT-NikQ (shown in Figure 4.5 A).[5] Figure 4.5 shows retention volumes of ~24-25 mL for each of the substrate-free variants (circles), with WT-NikQ (dark blue) in A, I338G (light blue) in B, and I338GI345G (teal) in C. Incubation with substrate leads to early elution at a retention

volume of ~13-14 mL, consistent with the formation of a stable NikQ•L-his-NikP1 complex also observed with the WT-P450.[5] The data for L-his-NikP1-bound NikQ-WT, I338G, and I338GI345G, represented in Figure 4.5 A, B, and C by red, pink, and gold triangles, respectively, demonstrates that substrate-binding capacity has been retained in the mutants.

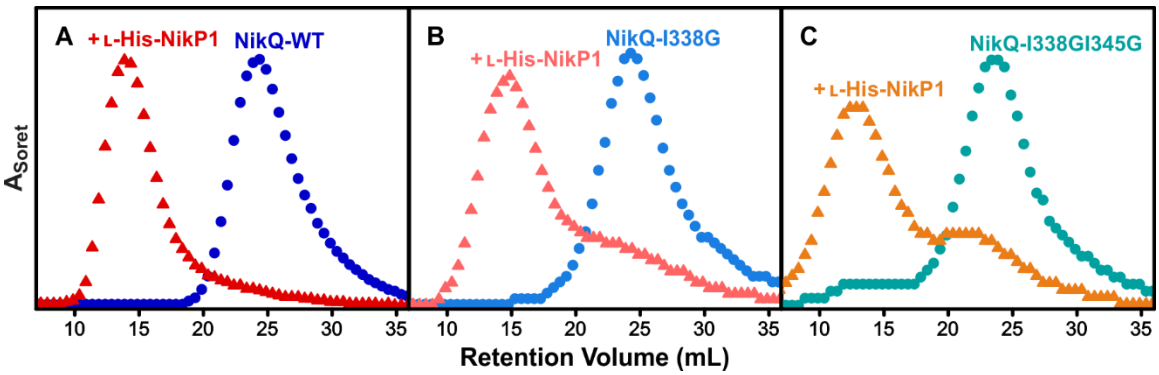

Figure 4.5. Size exclusion chromatography shows complex formation between the NikQ variants and L-his-NikP1. Substrate-free (circles) NikQ-WT (**A**, dark blue), I338G (**B**, light blue), and I338GI345G (**C**, teal) variants all feature retention times of ~24-25 mL. Addition of L-his-NikP1 results in earlier retention times of ~13-14 mL (triangles, with WT in red, I338G in pink, and I338GI345G in gold), indicative of stable binding between the P450 and its substrate.

4.3.2 The NikQ proximal mutants exhibit altered small molecule ligand affinities

WT-NikQ has been shown to have, at best, a very weak affinity for free L-histidine, demonstrating no optical change upon incubation with excess free L-his.[1, 5] However, since UV-visible spectra of the mutants imply nitrogen-ligation following substrate addition, binding of the mutants to free L-his was analyzed using absorbance spectroscopy. Figure 4.6 shows the spectra resulting from the incubation of I338G (A) and I338GI345G (B) with 10 equivalents of this amino acid. The single mutant Soret remains at 419 nm, after the addition of L-his, however, the double mutant Soret exhibits a 4 nm bathochromic shift and reduced absorbance, as well as enhancement of the β Q-band. This data confirms that the

I338GI345G variant possesses an increased affinity for L-histidine versus the single mutant and the WT P450. Of more catalytic significance, this also indicates that the double mutant is likely ligating an L-his-NikP1 nitrogen, which may form a substrate-inhibitor complex.

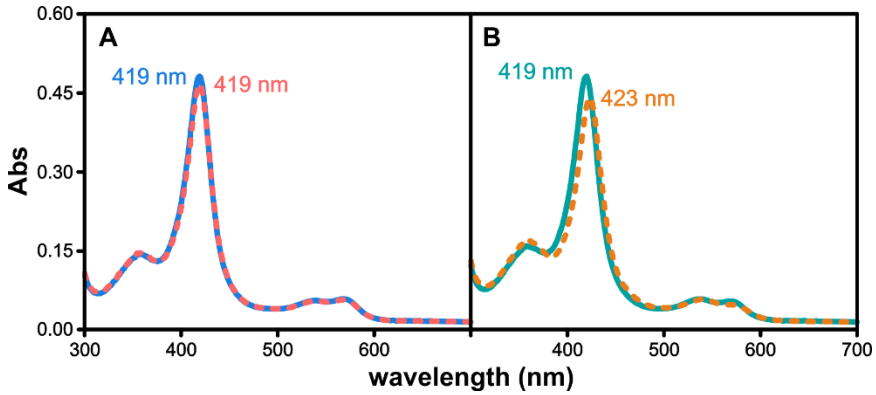

Figure 4.6. Optical monitoring of I338G (A) and I338GI345G (B) following the addition of 10 equivalents of free L-histidine. The L-his-supplemented spectrum of the single mutant (**A**, dashed pink spectrum) displays no shift in Soret maxima, significant change in absorbance, or alteration of the β:α Q-band intensities. In contrast, the addition of L-his to the double mutant (**B**, dashed gold spectrum) results in a 4 nm red-shift of the Soret, a decrease in Soret extinction, and an increase in the β:α Q-band ratio confirming that this variant has an enhanced affinity for this small molecule.

Quantitive comparison of L-his binding in the WT, single mutant, and double mutant NikQ variants necessitates ligand concentrations beyond the solubility of this amino acid, due to the low affinities of NikQ-WT and I338G for this small molecule. To circumvent the limited solubility of L-his while still allowing the opportunity for binding constant analysis, imidazole titrations were performed, as imidazole is structurally analogous to the L-his R-group but has significantly improved (~37-fold) solubility compared to free histidine. Results of these equilibrium binding titrations for the substrate-free WT, I338G, and I338GI345G NikQ variants are shown with representative spectra in Figure 4.7 (binding data and fits in the insets). WT and I338G NikQ showed extremely low

affinities for imidazole, with dissociation constants of 13.3 ± 0.6 mM and 5.3 ± 0.2 mM, respectively. For context, CYPs with imidazole K_D-values in the ~200 µM range are considered to be low affinity.[17, 52] The I338GI345G mutant exhibited a dramatic ~185-fold increase in affinity relative to the WT protein, with a K_D of 72 ± 1 µM. Attempts to meaure a substrate-bound imidazole binding constant were made for the WT and I338G P450s. Scattering from the NRPS substrate, however, becomes problematic at very high concentrations of imidazole, and no saturation of the protein with the small molecule ligand could be achieved. This was not carried out with substrate-bound I338GI345G, as the substrate-bound form of this variant is optically indistinguishable from the imidazole-ligated state.

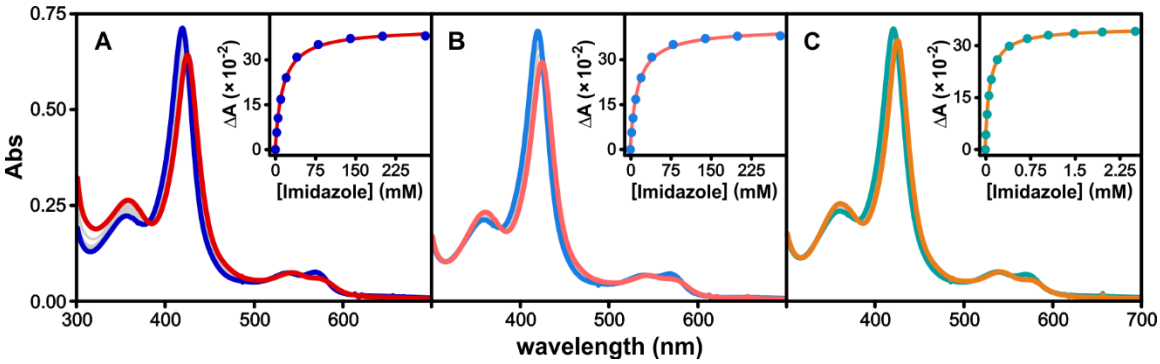

Figure 4.7. Equilibrium binding analysis of the NikQ variants to imidazole. Substrate-free NikQ-WT (**A**, dark blue), I338G (**B**, light blue), and I338GI345G (**C**, teal) were titrated with pH 7.5 imidazole until spectral stability was reached following increasing addition of the ligand. Imidazole-bound Soret peaks were at 424 nm for WT (red) and I338G (pink), and 425 nm for I338G (gold). The changes in absorbance were graphed as a function of imidazole concentration, and fit to a hyperbolic binding function to obtain imidazole dissociation constants. Measured dissociation constants were 13.3 ± 0.6 mM, 5.3 ± 0.2 mM, and 72 ± 1µM for NikQ-WT, I338G, and I338GI345G, respectively.

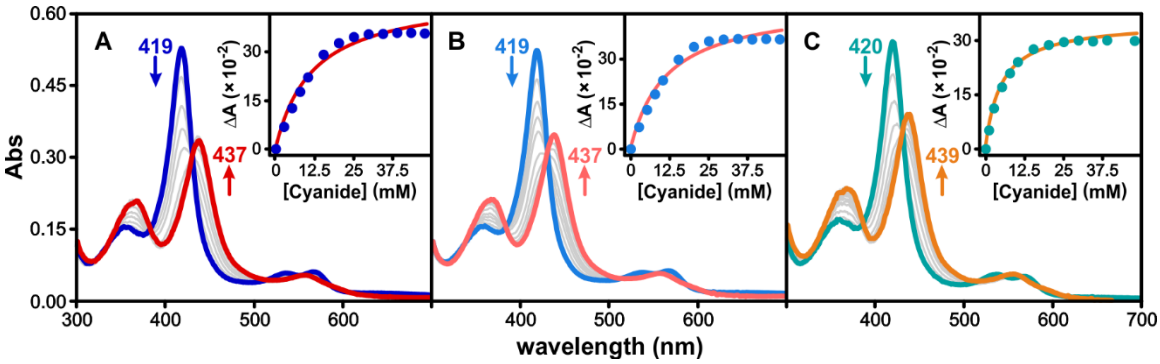

Figure 4.8. Equilibrium binding titration of aqueous sodium cyanide into each of the substrate-free NikQ variants show low affinities for this ligand. Cyanide-binding resulted in spectral shifts to 437 nm for WT (**A**) and I338G (**B**), and 439 nm for I338GI345G (**C**). Changes in absorbance were graphed as a function of cyanide concentration and fit to hyperbolic binding functions, as shown in the insets, to yield dissociation constants of the substrate-free P450 for cyanide. The change in absorbance was calculated from absolute value of the decrease in absorption at 437 nm.

The I338G and I338GI345G mutations proximal to the heme appear to modulate ligand binding on the distal side of the cofactor with uncharged nitrogenous ligands resembling the L-his-NikP1 substrate. To further investigate the impact of removing the sterics from the 338 and 345 positions, coordination of cyanide was analyzed. Cyanide binding analyses allow for investigation of a small anionic ligand that is often used as a mimic for O_2 in P450s.[53-55] Dioxygen only binds the ferrous enzyme to yield a typically short-lived and unstable intermediate state with a Soret shift of 0-to-10 nm. In contrast, cyanide ligates the ferric iron to form a stable complex with the cytochrome which undergoes a large optical change (~ 20 nm) at the Soret.[53-55] This spectral shift is distinct from that of nitrogen-ligation, affording the option of binding analysis using the substrate-bound form of the NikQ mutants despite coordination of the substrate L-histidine. Figure 4.8 shows the results of substrate-free cyanide binding titrations for NikQ-WT (A), I338G (B), and I338GI345G (C). In agreement with other reported P450-cyano complexes, cyanide-bound NikQ exhibits a Soret at ~437 nm (439 nm in the double mutant) with a

decreased extinction coefficient and merged Q-bands at ~565 nm.[53-55] All substrate-free NikQ variants exhibit low affinities for cyanide, with K_D values of 11 ± 3 mM, 11 ± 2 mM, and 5 ± 1 mM for WT, the single mutant, and the double mutant.

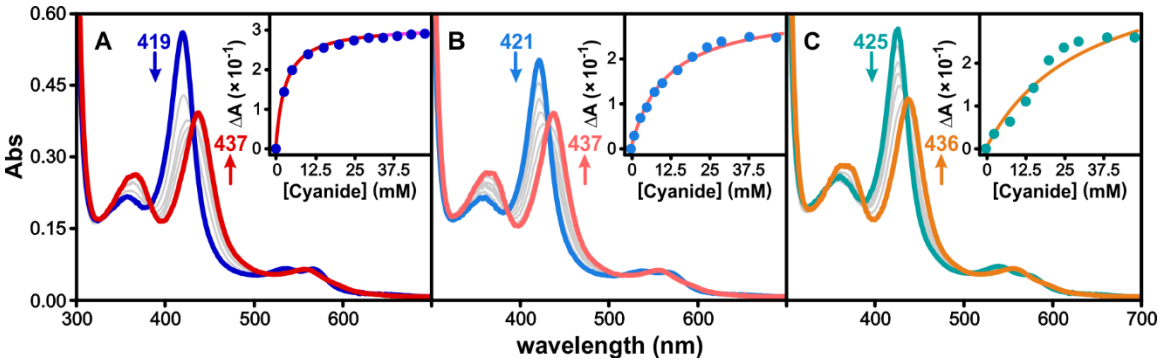

Figure 4.9. Equilibrium binding analysis of cyanide to the L-his-NikP1-bound NikQ variants reveal differences between the WT enzyme and the mutants. The final cyanide-ligated spectra for substrate-bound WT-NikQ (**A**, red), I338G (**B**, pink), and I338GI345G (**C**, gold) share similar spectral characteristics between them, as well as with the previously described cyanide-bound substrate-free states. However, the WT cyanide affinity has increased ~5-fold, while the I338G value is largely unchanged, and the I338GI345G binding constant is weakened by ~6-fold.

These titrations were also performed for the substrate-bound variants (Figure 4.9), with NikQ-WT demonstrating an increased affinity for cyanide of 2 ± 1 mM. This order-of-magnitude higher affinity in the presence of substrate is not atypical of substrate-bound P450s.[54] The two mutants, however, both exhibited weakened affinities (14 ± 3 mM for I338G and 32 ± 1 mM for I338GI345G) for the anionic small molecule when substrate-bound. This supports the observation that with each subsequent decrease in atypical proximal sterics (via I-to-G substitution), the affinity for nitrogen-ligands increases, resulting in partial ligation of the substrate in I338G and optical spectra indicative of full ligation of the substrate by I338GI345G. In the mutants, this ligation of a high-affinity substrate by the heme-iron essentially inhibits binding of cyanide to the metal until cyanide

concentrations are excessive enough to drive the equilibrium toward displacement of the ligated substrate nitrogen. This results in decreased cyanide affinities in the substrate-bound mutants, with K_D values for cyanide that are inversely proportional to the those of a variant for the substrate histidine. Due to the volatility of cyanide at neutral pH values, titrations were performed using NaCN at a pH of ~11.5, which resulted in a pH-dependent influence on the binding data which resembles a sigmoidal pH titration. This is not often observed in P450-cyanide titrations, as most CYPs have a more favorable dissociation constant for cyanide than the values reported here, and thus do not require such high cyanide concentrations for complete binding. Accordingly, the influence of this sigmoidal baseline becomes more pronounced with higher K_D values, as the protein solution becomes increasingly basic with the increased cyanide concentration required to acheive saturation of the binding curve (as in Figure 4.9 B). For measurements resulting in lower K_D values, this effect is minimized and the binding curve is the expected hyperbolic shape (as in Figure 4.9 A).

In order to assess whether the L-his-NikP1 substrate is able to displace a ligated cyanide in the NikQ variants, and as an additional means of verifying the strength of substrate-ligation relative to another ligand, 75 µM L-his-NikP1 was incubated with ~5 µM of NikQ-WT, I338G, and I338GI345G, each pre-bound to cyanide. Optical monitoring revealed notable spectral differences following addition of the protein substrate, as shown below in Figure 4.10. The wild-type enzyme (A) only undergoes a moderate blue shift from the 437 nm cyanide-bound Soret to 435 nm after addition of 15 equivalents of substrate. The I338 mutant exhibits a slightly larger blue shift upon substrate addition to 433 nm (data not shown). The double mutant, shown in Figure 4.10 B, features Soret at 427 nm, just 2

nm from the substrate-bound maximum for this variant, following addition of the same amount of L-his-NikP1. While the displacement of the anionic ligand by substrate due to ligation was expected in the double mutant, and to a lesser degree in the single mutant, the shift in absorbance maxima for wild-type is somewhat surprising. These results seem to indicate that some degree of displacement cyanide-displacement is occurring in the wild-type enzyme, even though there are no optically distinguishable signs of ligation.

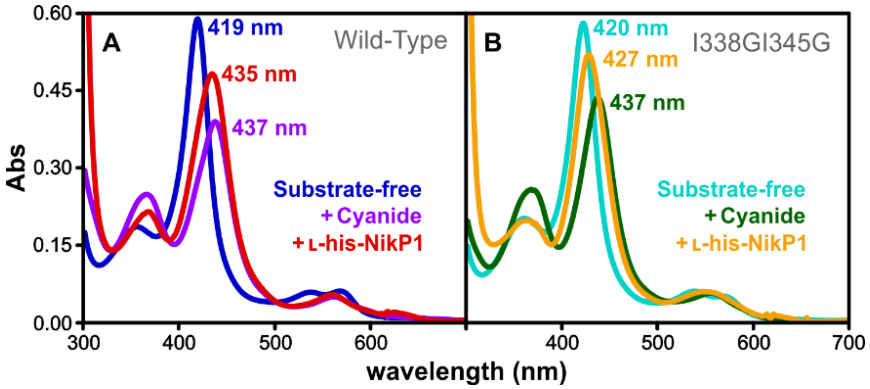

Figure 4.10. Attempted displacement of NikQ-bound cyanide via addition of the L-his-NikP1 substrate. 5 µM of cyanide-ligated NikQ (purple WT spectrum in **A** and green I338GI345G spectrum in **B**) was incubated with 75 µM substrate then analyzed using absorbance spectroscopy. Each variant displayed some degree of displacement, as determined by a blue-shifted Soret peak and increased absorbance. WT experienced the most minimal change, with final Soret maxima shifted to 435 nm (**A**, red) from an initial 437 nm. The I338GI345G mutant demonstrated the largest change to 427 nm (**B**, gold) from 437 nm so that the final Soret peak was within 2 nm of the substrate-bound form without cyanide.

4.3.3 Analysis of substrate and ligand-binding by electron paramagnetic resonance

Electron paramagnetic resonance (EPR) allows for sensitive investigation of changes in ferric mononuclear iron ligation states, with signals arising from the non-integer spins of the iron d-electrons. Following equilibrium binding analyses, EPR was performed to gain better insight into the geometrical and electronic changes occurring at the heme

across the three NikQ variants in the as-purified, substrate-bound, and small molecule-ligated forms. Figure 4.11 shows the results of EPR studies using 100 µM NikQ-WT (A), I338G (B), and I338G/I345G (C) in the substrate-free ferric resting state with aquo- sixth ligand (top row of spectra). The next two rows down display spectra following incubation with 500 µM L-his-NikP1 substrate and in the presence of 5 equivalents of L-histidine. The bottom row features spectra of the imidazole-ligated form of each variant.

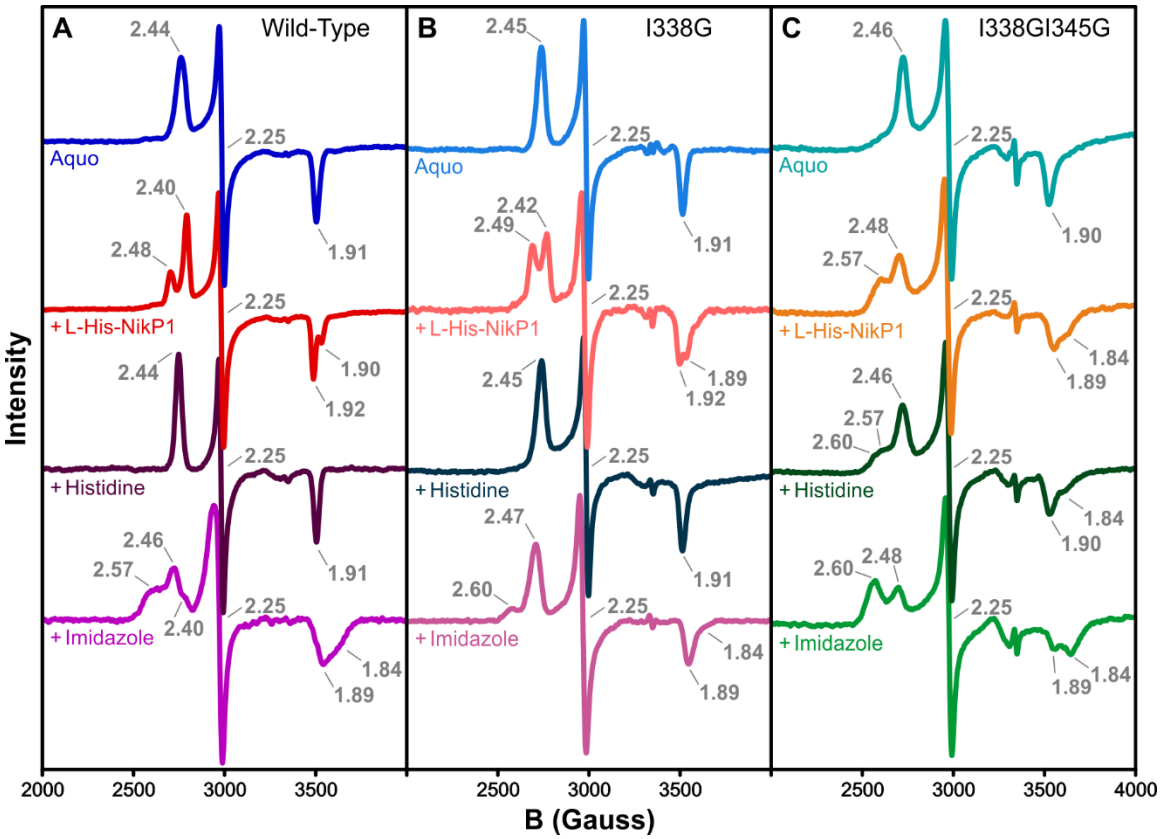

Figure 4.11. EPR spectra of 100 µM of the NikQ variants in the resting state, bound to substrate, and with potential nitrogen ligands similar to the protein-tethered substrate. NikQ WT (**A**), I338G (**B**), and I338GI345G (**C**) are shown in the substrate-free ferric-aquo state (top row - dark blue, light blue, and teal), after addition of 500 µM L-his-NikP1 substrate (second row down – red, pink, and gold), 5 equivalents of L-histidine (third row down – dark purple, navy blue, and dark green), or an excess of imidazole (bottom row – violet, mauve, and light green).

Table 4.2. EPR *g*-values and derived crystal field parameters for NikQ-WT, I338G, and I338GI345G in the resting and substrate-bound states, and with various ligands.

NikQ Variant	± Substrate	Ligand Added	*g*-values			Distortions		Rhombicity, |V/Δ|	ΔRhombicity (vs. Sub-Free)
			g_{Max}	g_{Mid}	g_{Min}	|Δ/λ|	|V/λ|		
WT	-	N/A	2.44	2.25	1.91	6.12	2.93	0.48	N/A
	+	N/A	2.48	2.25	1.90	5.88	3.21	0.54	0.07
			2.40	**2.25**	**1.92**	6.39	2.59	0.40	-0.07
	-	L-His	2.44	2.25	1.91	6.12	2.93	0.48	0.00
	-	Imidazole	2.57	2.25	1.84	5.06	3.19	0.63	0.15
			2.46	**2.25**	**1.89**	5.79	2.89	0.50	0.02
			2.40	2.25	1.84	5.33	1.84	0.34	-0.13
	-	Cyanide	2.54	2.29	1.84	4.84	2.37	0.49	0.01
	+	Cyanide	2.47	2.30	1.86	5.08	1.84	0.36	-0.12
I338G	-	N/A	2.45	2.25	1.91	6.09	3.04	0.50	N/A
	+	N/A	2.49	2.25	1.89	5.73	3.17	0.55	0.05
			2.42	**2.25**	**1.92**	6.33	2.83	0.45	-0.05
	-	L-His	2.45	2.25	1.91	6.09	3.04	0.50	0.00
	-	Imidazole	2.60	2.25	1.84	5.05	3.34	0.66	0.16
			2.47	**2.25**	**1.89**	5.77	2.98	0.52	0.02
	-	Cyanide	2.56	2.29	1.84	4.81	2.51	0.52	0.02
	+	Cyanide	2.56	2.30	1.84	4.76	2.37	0.50	0.00
			2.49	**2.30**	**1.85**	4.95	1.94	0.39	-0.11
I338G/I345G	-	N/A	2.46	2.25	1.90	5.93	3.01	0.51	N/A
	+	N/A	2.57	2.25	1.84	5.06	3.19	0.63	0.12
			2.48	**2.25**	**1.89**	5.75	3.08	0.53	0.03
	-	L-His	2.60	2.25	1.84	5.05	3.34	0.66	0.15
			2.57	2.25	1.84	5.06	3.19	0.63	0.12
			2.46	**2.25**	**1.90**	5.93	3.01	0.51	0.00
	-	Imidazole	**2.60**	**2.25**	**1.84**	5.05	3.34	0.66	0.15
			2.48	2.25	1.89	5.75	3.08	0.53	0.03
	-	Cyanide	2.57	2.30	1.83	4.66	2.36	0.51	0.00
	+	Cyanide	**2.57**	**2.30**	**1.83**	4.66	2.36	0.51	0.00
			2.46	2.25	1.89	5.79	2.89	0.50	-0.01

Bolded values represent the dominant set of *g*-values out of multiple species. Values in blue exhibited a deviation from the axis of maximal distortion observed in data shown in black.

All spectra exhibit rhombic line shapes characteristic of ferric thiolate-ligated heme-iron with hexacoordinate anisotropy.[2, 53, 54, 56-61] The data from these experiments is summarized in Table 4.2, with g_{max} corresponding to the highest magnitude *g*-value, g_{min} to the lowest magnitude value, and g_{mid} to the intermediate value.[58] Table 4.2 also features the derived values of tetragonal distortion (Δ/λ), orthorhombic distortion (V/λ), rhombicity

(|V/Δ|), and the change-in-rhombicity (Δrhombicity) for each spectrum relative to the resting state.[58]

Table 4.3. Assignment of NikQ EPR *g*-values to the correct z, x, and y coordinates and the resulting eigenstates A, B, and C.

NikQ Variant	± L-His-NikP1	Ligand Added	*g*-values			Eigenstates		
			g_z	g_y	g_x	A	B	C
WT	-	N/A	1.91	2.25	2.44	0.13	0.99	-0.03
	+	N/A	1.90	2.25	2.48	0.14	0.99	-0.03
			1.92	2.25	2.40	0.12	1.00	-0.02
	-	L-His	1.91	2.25	2.44	0.13	0.99	-0.03
	-	Imidazole	1.84	2.25	2.57	0.17	0.99	-0.05
			1.89	2.25	2.46	0.14	0.99	-0.03
			1.84	2.25	2.40	0.14	0.98	-0.02
	-	Cyanide	1.84	2.29	2.54	0.17	0.99	-0.04
	+	Cyanide	1.86	2.30	2.47	0.15	0.99	-0.02
I338G	-	N/A	1.91	2.25	2.45	0.13	0.99	-0.03
	+	N/A	1.89	2.25	2.49	0.14	0.99	-0.04
			1.92	2.25	2.42	0.13	1.00	-0.03
	-	L-His	1.91	2.25	2.45	0.13	0.99	-0.03
	-	Imidazole	-2.60	-1.84	2.25	0.81	0.08	-0.59
			1.89	2.25	2.47	0.14	0.99	-0.03
	-	Cyanide	1.84	2.29	2.56	0.17	0.99	-0.04
	+	Cyanide	1.84	2.30	2.56	0.17	0.99	-0.04
			1.85	2.30	2.49	0.16	0.99	-0.03
I338G/I345G	-	N/A	1.90	2.25	2.46	0.14	0.99	-0.03
	+	N/A	1.84	2.25	2.57	0.17	0.99	-0.05
			1.89	2.25	2.48	0.14	0.99	-0.03
	-	L-His	-2.60	-1.84	2.25	0.81	0.08	-0.59
			1.84	2.25	2.57	0.17	0.99	-0.05
			1.90	2.25	2.46	0.14	0.99	-0.03
	-	Imidazole	-2.60	-1.84	2.25	0.81	0.08	-0.59
			1.89	2.25	2.48	0.14	0.99	-0.03
	-	Cyanide	1.83	2.30	2.57	0.17	0.99	-0.04
	+	Cyanide	1.83	2.30	2.57	0.17	0.99	-0.04
			1.89	2.25	2.46	0.14	0.99	-0.03

Table 4.3 shows additional calculated values and the assignments necessary to compute the parameters shown in Table 4.2. Assignment of g_{Max}, g_{Mid}, and g_{Min} by default as g_z, g_y, and g_x can result in instances where rhombic distortion greatly exceeds axial

distortion, resulting in inappropriately elevated rhombicity values that exceed the theoretical upper limit of 2/3.[58, 59] In such cases, correct assignment of g_z, g_y, and g_x should be based on the computed parameters from six different allowable coordinate assignments, summarized in Table 4.4, that result in the lowest rhombicity value while yielding a positive orthorhombic distortion.[58] Each NikQ EPR spectrum possessed an axis of maximal distortion deviating from that in which the assignment of the highest *g*-value as *z* and the lowest as *x* is appropriate. This resulted in rhombicity values exceeding 0.67 and instead ranging from 0.70 to 1.12. The correct assignment of the coordinates yielded crystal field parameters within theoretical limits.

Table 4.4. Allowable assignments of g_{Max}, g_{Mid}, and g_{Min} to the z, y, and x coordinates.

Allowed Assignment	*g*-values		
	g_z	g_y	g_x
I	$-g_{Max}$	$-g_{Min}$	g_{Mid}
II	g_{Min}	g_{Mid}	g_{Max}
III	$-g_{Mid}$	$-g_{Min}$	g_{Max}
IV	$-g_{Max}$	g_{Mid}	$-g_{Min}$
V	g_{Min}	g_{Max}	g_{Mid}
VI	$-g_{Mid}$	g_{Max}	$-g_{Min}$

In the resting state with sixth aquo ligand, there appears to be only one species present for each variant, with g_{Max} at 2.44, 2.45, and 2.46 and g_{Min} at 1.91, 1.91, and 1.90 for WT, I338G, and I338GI345G, respectively. All spectra shown in Figure 4.9 featured g_{Mid} at ~2.25. The deviations in g_{Max} and g_{Min} values between the variants result in a progressive increase of rhombic character with mutation, as $|V/\Delta|$ calculations indicate values of 0.48 for WT, 0.50 for the single mutant, and 0.51 for the double mutant. This trend of increasingly rhombic character with decreasing sterics at the proximal site due to

mutation holds across the resting, substrate-bound, L-his supplemented, and imidazole-ligated states. Further, rhombicity increased with the likelihood of nitrogen-ligation (generally, it is expected that a P450 would have a increased affinity for imidazole versus L-his, and L-his versus a protein-tethered histidine).[52] This likely signifies an alteration to the geometry of the axial ligands and their bonds to the iron atom,[59] which would have to owe to changes near the thiolate ligand, as one mutated residue is adjacent to this cysteine and the other is in close proximity. The tetragonal field is decreased in the single mutant, and further so in the double mutant, which is consistent with diminished electron donation to the iron from the axial ligands.[59] It seems logical that this also derives from alterations at the thiolate ligand side of the iron, due to the locations of the mutated amino acids and the commonality of the ligands analyzed. This could implicate to an increasingly weakened S-Fe bond corresponding to the removal of each targeted isoleucine side chain.

It may be relevant to note that the imidazole-bound geometries exhibiting rhombicities of 0.66 for each of the mutants, along with one electronic species of L-histidine-coordinated double mutant with an equivalent value, showed a deviation from the axis of maximal distortion used for the other species on Table 4.2. In fact, these three display the highest rhombicity values from this series of EPR experiments, just below the theoretical limit of 0.67. The tetragonality is also low for a P450 with such high rhombicity, falling closer to the range of values expected of a low-spin hexacoordinate heme with axial histidine and oxygen ligands than those of a low-spin thiolate-ligated heme.[56, 59] This may indicate a significant alteration to the geometry of the bonded axial ligands in this conformer, and possibly even a change in ligand identity through the loss of the cysteine-derived thiolate bond to the iron.

Futher EPR analysis was performed on the cyanide complexes of NikQ-WT, I338G, and I338G/I345G in both the substrate-free and L-his-NikP1-bound forms. Resulting spectra are shown in Figure 4.12 for WT (A), I338G (B), and I338GI345G (C), with the substrate-free samples in shades of blue/teal and the NRPS-bound P450 in red/pink/gold. The *g*-values obtained from this data are shown in Table 4.2. The cyanide-bound, substrate-free variants feature *g*-values around 2.55, 2.30, and 1.84, which are shifted versus the cyanide-free resting enzyme, but are within the range of EPR values reported for some P450 cyanide complexes.[54] Upon addition of substrate, the g_{Max}- and g_{Min}-values of the WT enzyme exhibit (in red, A) increased intensity and peak-narrowing relative to the substrate-free form. This is likely indicative of a more homogeneous cyanide ligand geometry with fewer conforming species contributing to the averaged EPR signal. The single mutant (pink spectra in B) undergoes a splitting of the g_{Max}-value in the presence of substrate, signifying two different populations of the cyanide-ligated CYP in the presence of substrate, possibly owing to a perturbation of the coordinated ligand geometry due to steric restrictions or hydration changes within the distal pocket. There also appear to be two separate rhombic species in this spectrum (gold, C), indicated by the appearance of a second, less intense g_{mid} signal beneath the one at 2.30 corresponding to ligated cyanide. This minor species, with g = 2.46, 2.25, and 1.89 may derive from ligation of the substrate histidine, though the g_{max} more closely resembles the resting state of the enzyme. It is surprising that this variant does not appear to be fully cyanide-bound despite the extreme excess of cyanide in the sample, though this may owe to a difference in the affinities of the P450, as well as the heme-iron, for the NikP1-tethered L-histidine versus cyanide.

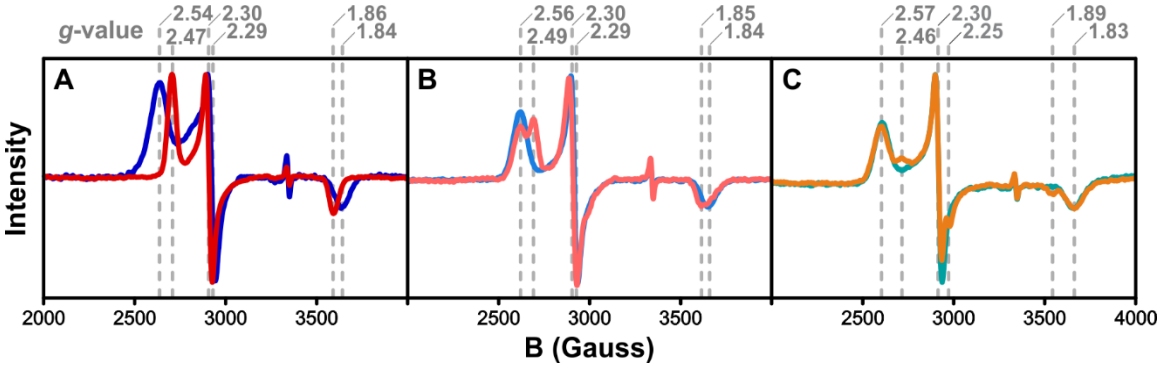

Figure 4.12. EPR of the cyanide-bound NikQ variants in the absence and presence of substrate. 100 µM WT-NikQ (**A**), I338G (**B**), and I338GI345G (**C**) were incubated with 500 mM cyanide to yield the samples shown in dark blue, light blue, and teal, respectively. The red, pink, and gold spectra resulted from samples in which 100 µM of each NikQ variant was incubated with 500 µM L-his-NikP1 prior to the addition of 500 mM cyanide.

With the negatively-charged cyanide ligand, the trend of increasingly rhombic character that was observed for neutral nitrogen ligation is disrupted. In the cyanide samples that do not contain NikP1, the I338G mutant displays the highest rhombicity, followed by I338GI345G, then WT. Upon addition of substrate, the predominant population of the double mutant undergoes minimal change, while the WT and one geometry of the single mutant see decreases in $|V/\Delta|$, with WT seemingly conforming to a more homogeneous state. These observations may owe to the relatively large differences in the affinities of each variant for cyanide presence of substrate, as determined from the previously discussed equilibrium binding analyses.

4.3.4 Mutants Proximal to the NikQ Heme Alter Oxy-Complex Stability

Anaerobic stopped-flow spectroscopy was utilized to collect spectra detailing the reaction of reduced NikQ I338G or I338GI345G with dioxygen, in both the absence and presence of excess L-his-NikP1. In the absence of substrate, initial spectra of both variants,

shown in Figure 4.13 with I338G in A and I338GI345G in C, featured the red-shifted Soret maxima and merged Q-bands (blue/teal spectra) consistent with a ferric-superoxide species, at ~ 426 nm and ~557 nm respectively. Autoxidation was complete within 2 seconds for I338G and 1 second for I338GI345G, with both mutants returning to the water-ligated ferric low-spin state with Soret at ~419 nm and α/β Q-bands at ~565/535 nm. Formation of the oxy-complex was complete within the 1 ms deadtime of the instrument for both variants, and thus could not be resolved under O_2-saturating conditions, which is consistent with what has observed for WT-NikQ under the same conditions.[5] Difference spectra revealed a maximal change in absorbance for autoxidation of 443 nm and corresponding single-wavelength data (insets) was fit to a single exponential function. The rate constants of autoxidation were found to be 3.7 ± 0.2 s^{-1} and 7.1 ± 0.1 s^{-1} for substrate-free NikQ-I338G and I338GI345G. Though these rates are slightly accelerated, this remains a rapid process on the same order of magnitude of the WT rate of 2.8 s^{-1},[5] and thus does not represent a significant kinetic deviation. In the substrate-free form, little has changed between the WT enzyme and the mutants with respect to oxy-complex stability, with all 3 variants being relatively unstable.

Intriguingly, autoxidation was considerably impaired in the substrate-bound I338G mutant, requiring data collection over the course of 60 seconds. Figure 4.13 B shows initial Soret maxima (navy blue spectrum) at ~414 nm with decreased extinction and merged Q-bands centered at ~550 nm, likely a mix of ferrous-P450 and ferric-superoxide species. The oxy-complex (light blue spectrum) of L-his-NikP1-bound I388G displayed the same spectral features described for the substrate-free form, and returned to the low-spin state previously described (pink spectrum). Fitting of single wavelength data at 443 nm (inset)

required a three-summed exponential function corresponding to a single oxy-intermediate formation phase with increasing absorbance, and a biphasic autoxidation of decreasing absorbance with respective rate constants of 44 ± 6 s^{-1}, 0.8 ± 0.1 s^{-1} and 0.08 ± 0.01 s^{-1}. The increased kinetic complexity of superoxide release may owe to different species of the substrate-bound P450 possessing varying degrees of oxy-complex stability due to differences in substrate positioning above the iron. Data derived from optical and EPR spectroscopies with this mutant reflect this possibility with a substrate-bound Soret maxima of 422 nm in the former, possibly owing to partial deprotonation of the iron-ligated water or a mixture of substrate L-histidine-ligated and unligated species. EPR of L-his-NikP1-bound NikQ shows a similar mixture of species with the same potential assignments, providing little distinction between the two.

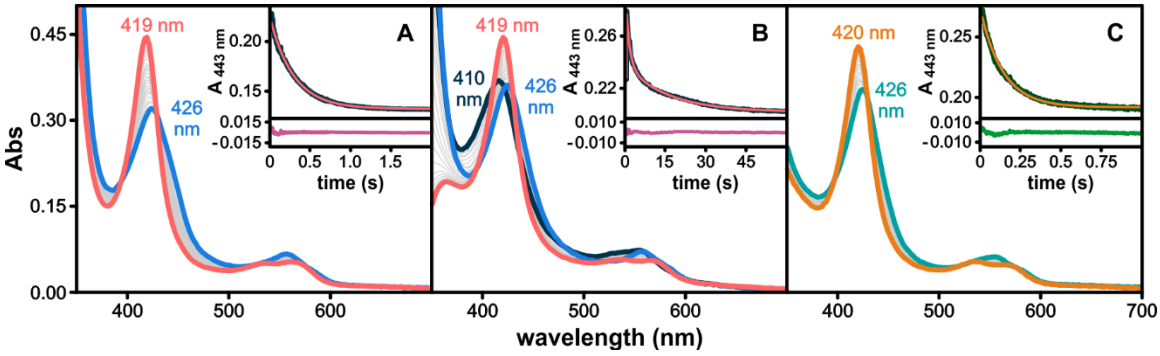

Figure 4.13. Autoxidation of substrate-free I338G (A), substrate-bound I338G (B), and substrate-free I338GI345G (C). Stopped-flow transient kinetics analysis was performed through rapid-mixing of 10 µM anaerobic, ferrous P450 (accompanied by 100 µM L-his-NikP1 for the single mutant in panel **B**) with O_2-saturated buffer at 4 °C. Autoxidation of the oxy-complex (**A** and **B**, light blue; **C**, teal) at 426 nm to the low-spin ferric resting state (pink in **A** and **B**, gold in **C**) was complete within 2 seconds for substrate-free I338G and within 1 second for substrate-free I338GI345G. Formation of the dioxygen adduct occurred within the deadtime of the instrument for the substrate-free mutants at post-mix O_2 concentrations above 0.4 mM. Initially, the substrate-bound mutant in **B** is still partially in the ferrous form, in navy with Soret maxima at 414 nm, and data collection for 60 seconds allowed for resolution of ferric-superoxide intermediate formation and bi-phasic autoxidation.

The optical and EPR data agree that the double mutant likely ligates the heme-iron, raising the possibility of inhibition of reduction and dioxygen ligation, which has been observed in some P450s.[52] Indeed, multiple reduction attempts were not successful in generating the expected 410 nm Soret in the substrate-bound form of this variant so subsequent O_2-binding and autoxidation could not occur. In light of the inability to reduce a substrate-ligated variant of the same protein, it seems likely that the substrate positioning in NikQ-I338G has yielded two populations in the substrate-bound low-spin form, with one altering the pK_a of the aquo-ligand. These different populations within the active site could have different stabilization effects on the dioxygen-adduct in the oxy-complex, leading to the two autoxidation phases. The ability to reduce the single mutant to the ferrous pentacoordinate P450 when substrate-bound seems to minimize the possibility of the second autoxidation phase deriving from a substrate-ligated species, especially in comparision with the double mutant.

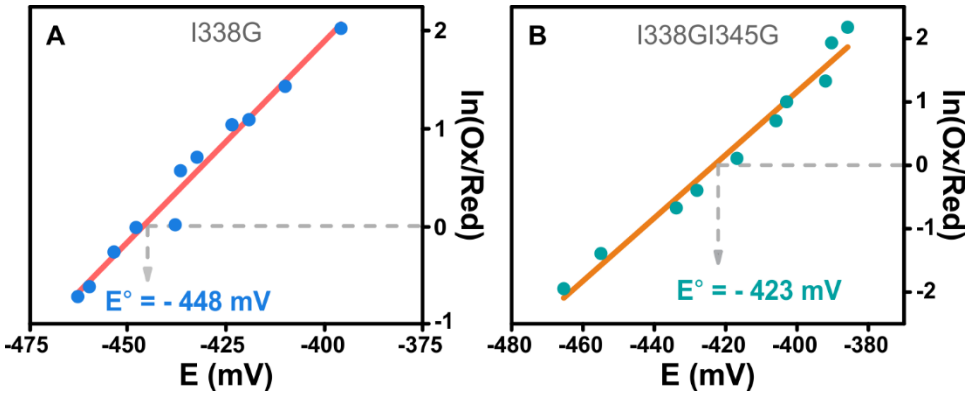

Figure 4.14. Measured redox potentials of the substrate-free NikQ mutants. The reduction potentials for the I338G (**A**) and I338GI345G (**B**) mutants were measured in the absence of L-his-NikP1 using methyl viologen, with E° = -446 mV, as an indicator dye. The potential for the single mutant was found to be -448 mV, with the double mutant potential poised at -423 mV, demonstrating that neither variant deviates significantly from the also unusually low -415 mV value measured for the WT enzyme.

The reduction potentials of the substrate-free NikQ mutants were determined through spectroelectrochemical titration using methyl viologen, with E° = -446 mV, as an indicator dye, to probe whether the proximal mutants had impacted the $3^{+}/2^{+}$ couple of the heme-iron. Results are shown in Figure 4.14, with a measured E° of -448 mV for I338G (A) and -423 mV for I338GI345G (B). Both of these values are similar to the measured value for WT-NikQ of -415 mV, with neither mutant presenting a significant change from this unusually low value.[5]

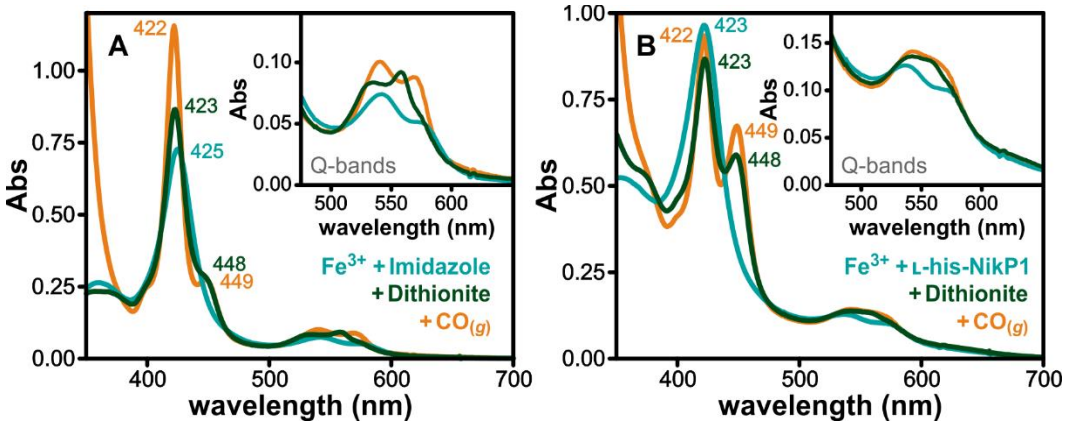

Figure 4.15. Attempts to reduce the I338GI345G imidazole complex (A) and substrate-bound enzyme (B). Reduction of the imidazole (**A**, teal) or substrate-bound I338GI345G (**B**, teal) complex yields at least two species (green) for both imidazole- and L-his-NikP1-bound enzyme. One species features Soret at 423 nm, and the other at 448 nm. Subsequent introduction of CO into the cuvette results in formation of either the carbonmonoxyf-errous cytochrome with Soret at 449 nm, or a species with increased extinction and Soret maxima at 422 nm typically indicative of injury to the thiolate ligand.

Reduction of the L-his-NikP1-bound I338GI345G mutant fails to yield the expected pentacoordinate reduced complex with Soret at 410 nm and merged Q-bands. With the majority of the data presented herein supporting inhibitory substrate-ligation by this mutant, attempts to form the ferrous cytochrome in the imidazole-ligated form were performed in parallel with the substrate-bound enzyme to explore the possibility of a

nitrogen-ligated hexacoordinate ferrous enzyme. These results are presented in Figure 4.15 with the double mutant bound to imidazole (A) or substrate (B) initially in the ferric state (teal). Chemical reduction yields the green spectra, which is comprised of a mixture of states, including a minor species with Soret at 448 nm and merged Q-bands, consistent with a ferrous hexacoordinate nitrogen-ligated complex[62] which accumulates to a higher degree in the presence of L-his-NikP1 versus imidazole. The main peak at 423 nm in the green spectra could be indicative of injury to the thiolate-ligand, unreduced ferric nitrogen-ligated enzyme, or an add-mix of the two. Following chemical reduction and data collection, the sealed cuvette was bubbled with $CO_{(g)}$ to assess the integrity of the thiolate ligand following reduction, and resulting spectra are presented in gold. In the instance of thiolate-ligand injury, a high extinction (relative to the ferric P450) centered around 422 nm is expected, instead of the Soret at ~450 nm that validates thiolate integrity. The CO-adduct of the imidazole-bound I338GI345G mutant results in a small amount of the ~450 nm species with a majority of the enzyme cofactor absorbing strongly at 422 nm. This may be indicative of a more labile Fe-S bond in this mutant, which would be consistent with the loss of electron-donating ligand character observed in the EPR studies. Curiously, the presence of substrate does appear to have a stabilizing effect on the thiolate compared to the structurally similar imidazole, with a higher $A_{450\ nm}/A_{422\ nm}$ ratio in the presence of L-his-NikP1. The majority of the enzyme, however, does appear to present predominantly with damaged thiolate coordination regardless of whether the nitrogen bound to the iron at the distal position derives from substrate or imidazole.

4.4 CONCLUSIONS

In summary, we present evidence supporting ligation of the L-his-NikP1 substrate by variants of cytochrome P450 NikQ, in which two atypically bulky isoleucine residues have been substituted by glycines to generate two mutants – I338G and I338GI345G. The double mutant possesses a higher affinity for imidazole and free L-his compared to the other mutants, and exhibits optical properties consistent with nitrogen ligation upon substrate binding. The single mutant also appears to ligate L-his-NikP1, though to a lesser degree. Both mutants demonstrate an increase in rhombicity with substrate or small molecule-derived nitrogen coordination in EPR studies relative to the WT protein, as well as a decrease in tetragonal distortion, supporting an alteration of ligand geometry and less electron donation to the iron from an axial ligand. Ligand binding studies using cyanide show an increase in K_D for the mutants in the presence of substrate, implicating that cyanide binding may be inhibited by the substrate. Attempts to produce the pentacoordinate ferrous substrate-bound double mutant have proven unsuccessful, and thus the oxy-complex of this variant cannot be analyzed. As a whole, this work demonstrates that removal of the sterics imparted to the NikQ proximal site by these isoleucine residues exerts a significant influence on interactions with the iron from the distal side of the heme cofactor, altering substrate-binding properties and resulting in a substrate-inhibitor complex. These unusually bulky proximal amino acids may serve the functional role of preventing inhibitory ligation of the NikP1-appended substrate L-histidine through modulation of structural details regarding heme-distortion and iron-coordination.

4.5 MATERIALS AND METHODS

4.5.1 Reagents and Chemicals

All microbiology reagents and media, as well as adenosine 5'-triphosphate, kanamycin (kan), ampicillin (amp), and DTT, were purchased from Research Products International. Glycerol, buffers, and chloramphenicol (CAM) were from VWR International. Tetracycline, methyl viologen, L-histidine, Tris-(2-carboxyethyl)-phosphine hydrochloride (TCEP), and sodium hydrosulfite (dithionite) were from Sigma Aldrich. Isopropyl-β-D-thiogalactopyranoside (IPTG) was from Gold Biotechnology. Hemin and δ-aminolevulinic acid were purchased from Carbosynth. The pChuA plasmid was a gift from Alan Jasanoff (Addgene plasmid # 42539).[63] The pG-Tf2 chaperone plasmid was from Takara Bio Inc. The vector for co-expression of the Sfp phosphopantetheinyl transferase out of *Bacillus subtilis* was generously provided by Professor Courtney Aldrich.

4.5.2 Molecular Biology, Heterologous Expression, and Protein Purification

NikQ-I338G and NikQ-I338G/I345G were generated by whole-plasmid mutagenesis, using the following semi-overlapping [64] primers.

I338G-F: 5'-CACCTGGGCTTCGGCCAGGGCAACCACTACTGCATCGGCTCCTCGCTC-3'

I338G-R: 5'-CTGGCCGAAGCCCAGGTGGCGGTTGGGTTCGCGCTCGATGTCGAA-3'

I345G-F: 5'-CTACTGCGGCGGCTCCTCGCTCGCCAAGCTCGAACTCACGGTG-3'

I345G-R: 5'-GGAGCCGCCGCAGTAGTGGTTGCCCTGGATGAAGCCCAGGTG-3'

I338GI345G-F: 5'-CTACTGCGGCGGCTCCTCGCTCGCCAAGCTCGAACTCACGGTG-3'

I338GI345G-R: 5'-GGAGCCGCCGCAGTAGTGGTTGCCCTGGCCGAAGCCC-3

Mutagenic PCR reactions utilized the previously described NikQ-WT construct[5] in pET28b (Kan^R) as template for the NikQ-I338G and NikQ-I345G single mutants, then the I338GI345G double mutant was amplified using the NikQ-I338G template. After

successful mutagenesis was confirmed by Sanger sequencing, NikQ-WT and the I338G variant were each expressed alongside the ChuA heme transporter protein [63, 65] in *E. coli* BL21(DE3) cells. The NikQ-I338GI345G plasmid was co-transformed with the ChuA plasmid (Amp^R) into BL21(DE3) cells also containing the pG-Tf2 (Cam^R) chaperone plasmid. Expression was carrier out in 2 L flasks containing 1 L of modified terrific broth media, comprised of the following: 24 $g \cdot L^{-1}$ yeast extract, 12 $g \cdot L^{-1}$ tryptone, 2 $g \cdot L^{-1}$ peptone, 2.31 $g \cdot L^{-1}$ monobasic potassium phosphate, 12.54 $g \cdot L^{-1}$ dibasic potassium phosphate, and 0.4% glycerol. Prior to inoculation with ~15 mL of saturated starter culture, media was supplemented with 50 $mg \cdot L^{-1}$ kanamycin, 100 $mg \cdot L^{-1}$ ampicillin, 30 $mg \cdot L^{-1}$ chloramphenicol (for I338GI345G growth containing the pG-Tf2 chaperone plasmid), 125 $mg \cdot L^{-1}$ thiamine-HCl, and a trace metals solution (50 µM $FeCl_3$, 20 µM $CaCl_2$, 10 µM $MnCl_2$, 10 µM $ZnCl_2$, 2 µM $CuCl_2$, 2 µM $CoCl_2$ and 2 µM $NiSO_4$). Cultures were incubated at 37 °C and 200 rpm until OD_{600} = ~1, when the temperature was decreased to 16 °C, and expression of chaperones was induced with 10 $\mu g \cdot L^{-1}$ tetracycline in the I338GI345G cultures. At OD_{600} = ~1.8, 5 $mg \cdot L^{-1}$ hemin was added and expression of the NikQ variants and ChuA was induced by the addition of 60 µM IPTG. Cells were harvested via centrifugation ~72 hours post-induction and stored at -70 °C until purification, which was completed according to established methods [5]. Expression and purification of holo-NikP1, as well as preparation of L-his-NikP1, were carried out using published protocols [5].

4.5.3 Equilibrium Binding Assessments

Spectroscopic shifts in NikQ upon substrate binding were investigated by the addition of 10-equivalent addition of L-His-NikP1 to NikQ with changes in absorbance spectra being monitored by an Agilent 8453 spectrophotometer. Size-exclusion

chromatography experiments were performed on NikQ mutants in accordance with the protocols established for NikQ with the use of a 405 nm filter as opposed to a 280 nm filter, thus eliminating the need for analysis of individual fractions using the spectrophotometer.[5] Small ligand binding titrations of cyanide and imidazole to the heme-iron were conducted via the incremental addition of ligand to a cuvette containing P450. For substrate bound NikQ the cuvette was held at ~15:1 L-His-NikP1:NikQ. Full UV-visible absorbance spectra were collected on the spectrophotometer following an incubation period to ensure complete equilibrium of the sample. Imidazole titrations were monitored for a Soret shift to 424 nm and cyanide to 437 nm. The binding signal, data derived from the change in absorbance at the wavelength of greatest change (ΔAbs) was graphed as a function of the ligand concentration, [L], and fit to the equilibrium binding function shown below in Equation 4.1 to determine the dissociation constant, K_D, where ΔAbs_{max} is the maximal change in absorbance observed at that wavelength.

Equation 4.1: $$\Delta Abs = \frac{\Delta Abs_{max} * [L]}{K_D + [L]}$$

4.5.4 Electron Paramagnetic Resonance Spectroscopy

EPR Samples containing 100 µM NikQ-I338G/I345G alone in 25 mM HEPES pH 7.5 with 500 mM NaCl, or in this buffer supplemented with 500 µM L-his-NikP1, 500 µM L-histidine, or 50 mM imidazole pH 7.5, were prepared in quartz EPR tubes at volumes of 225 µL before being frozen and stored in liquid nitrogen. EPR samples containing cyanide were prepared in quartz EPR tubes at 225 µL volumes containing 100 µM NikQ-WT, NikQ-I338G, or NikQ-I338G/I345G, each prepared in both the absence and presence of 500 µM L-his-NikP1, in 25 mM HEPES pH 7.5 with 500 mM NaCl supplemented to a final cyanide concentration of 500 mM. Cyanide was diluted from a 2.25 M stock with pH

adjusted to ~8.0, as the high pH of initially prepared sodium cyanide without the addition of acid caused enzyme precipitation. Samples were frozen and stored in liquid nitrogen. Data collection was carried out on a Bruker X-Band EMXplus EPR spectrometer equipped with an Oxford Instruments ESR900 X-Band Continuous Flow Liquid Helium Cryostat. Analysis was performed at temperatures between 10 and 15 K at a modulation amplitude of 10 Gauss and a microwave power of 2 mW. Resulting spectra were the average of ten 30 s scans from 340 to 6340 Gauss. Spectra were baselined using SpinCount software, then processed further using OriginPro and Corel Designer. Assignments of *g*-values to z, y, and x coordinates, calculation of eigenstates, and determination of tetragonal distortion, orthorhombic distortion, and rhombicity were carried out in the method described by Bohan.[58]

4.5.5 Stopped Flow Spectroscopy

Rapid-mix stopped-flow was performed on an Applied Photophysics SX-20 instrument equipped with an anaerobic accessory and a modified stop syringe allowing for a 1 ms deadtime. A photodiode array detector was used to collect 1,000 spectra in logarithmic time scales of 1 to 60 seconds, from ~265 to ~720 nm, at 4 °C. Instrument anaerobicity and sample preparation were achieved as previously described.[5] The buffer used for all samples consisted of 25 mM HEPES with 500 mM NaCl, at pH 7.5. O_2-saturated buffer was rapidly mixed at a 1:1 ratio with 10 µM of ferrous NikQ-variant, resulting in post-mix concentrations of ~1 mM O_2 and 5 µM P450. Fitting was performed using Pro-Data Viewer software from Applied Photophysics. Substrate-free traces at 443 nm were fit to a single exponential function shown below in Equation 4.2 according to Scheme 4.1, where the sequence in parenthesis is not resolvable within the instrument

deadtime under O_2-saturating conditions, $A_{t,\,obs}$ is the observable absorbance, k is the autoxidation rate constant (in s^{-1}), a is the amplitude, A_∞ is the final absorbance, and t is the time (in s).

Equation 4.2: $A_{t,obs} = A_\infty + ae^{-tk}$

Scheme 4.1: $\left(Fe^{2+} + O_2\right) \rightarrow Fe^{3+}\text{-}O_2^{\cdot-} \xrightarrow{k} Fe^{3+} + O_2^{\cdot-}$

Data collected in the presence of excess L-his-NikP1 substrate maintained the same concentrations of O_2 and NikQ-variant described for substrate-free experiments, but featured 100 µM substrate in the P450-containing sample, resulting in a post-mix concentration of 50 µM L-his-NikP1. Substrate-bound data for NikQ-I338G was fit at 441 nm to a 3-summed exponential function (Equation 4.3) according to Scheme 4.2. The single exponential formation phase of the oxy-intermediate with amplitude a_1 and observed dioxygen binding rate constant k_1 (s^{-1}). The more-complex double exponential decrease in absorbance has amplitudes a_2 and a_3, with rate constants k_2 and k_3 (both in s^{-1}) corresponding to two different autoxidation processes. $A_{t,\,obs}$ is the observable absorbance and A_∞ is the final absorbance.

Equation 4.3: $A_{t,obs} = A_\infty + a_1e^{-tk_1} + a_2e^{-tk_2} + a_3e^{-tk_3}$

Scheme 4.2: $Fe^{2+} + O_2 \xrightarrow{k_1} Fe^{3+}\text{-}O_2^{\cdot-} \xrightarrow{k_2,\,k_3} Fe^{3+} + O_2^{\cdot-}$

Fitting was not performed for substrate-bound NikQ-I338G/I345G, as the reduced state of the P450 was not achieved, and thus O_2-binding could not occur.

4.6 ACKNOWLEDGMENTS

I thank Gabriel D'Agostino for generation of both mutant constructs used in this work, as well as for his hard work expressing and purificating these proteins and for performing and processing the cyanide-binding titrations and assistance with the size exclusion chromatography experiments with these mutants. I also thank Prof. C. Aldrich for providing the plasmids for Sfp co- and over-expression. This work was supported by National Science Foundation CAREER grant 1555066 and an ASPIRE grant from the USC Vice President of Research to T.M.M..

4.7 REFERENCES

1. Chen, H.; Hubbard, B. K.; O'Connor, S. E.; Walsh, C. T., Formation of beta-hydroxy histidine in the biosynthesis of nikkomycin antibiotics. *Chem. Biol.* **2002,** *9* (1), 103-12.
2. Denisov, I. G.; Makris, T. M.; Sligar, S. G.; Schlichting, I., Structure and chemistry of cytochrome P450. *Chem Rev* **2005,** *105* (6), 2253-2277.
3. Luthra, A.; Denisov, I. G.; Sligar, S. G., Spectroscopic features of cytochrome P450 reaction intermediates. *Arch. Biochem. Biophys.* **2011,** *507* (1), 26-35.
4. Greule, A.; Stok, J. E.; De Voss, J. J.; Cryle, M. J., Unrivalled diversity: the many roles and reactions of bacterial cytochromes P450 in secondary metabolism. *Nat. Prod. Rep.* **2018,** *35* (8), 757-791.
5. Wise, C. E.; Makris, T. M., Recruitment and Regulation of the Non-ribosomal Peptide Synthetase Modifying Cytochrome P450 Involved in Nikkomycin Biosynthesis. *ACS Chem Biol* **2017,** *12* (5), 1316-1326.
6. Fischbach, M. A.; Walsh, C. T., Assembly-line enzymology for polyketide and nonribosomal Peptide antibiotics: logic, machinery, and mechanisms. *Chem Rev* **2006,** *106* (8), 3468-3496.
7. Sligar, S. G.; Gunsalus, I. C., A thermodynamic model of regulation: modulation of redox equilibria in camphor monoxygenase. *Proc Natl Acad Sci USA* **1976,** *73* (4), 1078-82.
8. Denisov, I. G.; Grinkova, Y. V.; Baas, B. J.; Sligar, S. G., The ferrous-dioxygen intermediate in human cytochrome P450 3A4. Substrate dependence of formation and decay kinetics. *J Biol Chem* **2006,** *281* (33), 23313-8.

9. Makris, T. M.; Davydov, R.; Denisov, I. G.; Hoffman, B. M.; Sligar, S. G., Mechanistic enzymology of oxygen activation by the cytochromes P450. *Drug Metab. Rev.* **2002,** *34* (4), 691-708.
10. Imai, Y.; Sato, R.; Iyanagi, T., Rate-limiting step in the reconstituted microsomal drug hydroxylase system. *J Biochem* **1977,** *82* (5), 1237-1246.
11. Lipscomb, J. D.; Sligar, S. G.; Namtvedt, M. J.; Gunsalus, I. C., Autooxidation and hydroxylation reactions of oxygenated cytochrome P-450cam. *J Biol Chem* **1976,** *251* (4), 1116-1124.
12. Eisenstein, L.; Debey, P.; Douzou, P., P450cam: oxygenated complexes stabilized at low temperature. *Biochem Biophys Res Commun* **1977,** *77* (4), 1377-1383.
13. Denisov, I. G.; Makris, T. M.; Sligar, S. G.; Schlichting, I., Structure and chemistry of cytochrome P450. *Chem Rev* **2005,** *105* (6), 2253-2277.
14. Tosha, T.; Yoshioka, S.; Ishimori, K.; Morishima, I., L358P mutation on cytochrome P450cam simulates structural changes upon putidaredoxin binding: the structural changes trigger electron transfer to oxy-P450cam from electron donors. *J Biol Chem* **2004,** *279* (41), 42836-43.
15. Yosca, T. H.; Rittle, J.; Krest, C. M.; Onderko, E. L.; Silakov, A.; Calixto, J. C.; Behan, R. K.; Green, M. T., Iron(IV)hydroxide pK(a) and the role of thiolate ligation in C-H bond activation by cytochrome P450. *Science* **2013,** *342* (6160), 825-9.
16. Olea, C.; Boon, E. M.; Pellicena, P.; Kuriyan, J.; Marletta, M. A., Probing the function of heme distortion in the H-NOX family. *ACS Chem Biol* **2008,** *3* (11), 703-10.

17. McLean, K. J.; Carroll, P.; Lewis, D. G.; Dunford, A. J.; Seward, H. E.; Neeli, R.; Cheesman, M. R.; Marsollier, L.; Douglas, P.; Smith, W. E.; Rosenkrands, I.; Cole, S. T.; Leys, D.; Parish, T.; Munro, A. W., Characterization of active site structure in CYP121. A cytochrome P450 essential for viability of Mycobacterium tuberculosis H37Rv. *J Biol Chem* **2008,** *283* (48), 33406-16.
18. Ost, T. W.; Clark, J.; Mowat, C. G.; Miles, C. S.; Walkinshaw, M. D.; Reid, G. A.; Chapman, S. K.; Daff, S., Oxygen activation and electron transfer in flavocytochrome P450 BM3. *J Am Chem Soc* **2003,** *125* (49), 15010-20.
19. Davydov, R.; Im, S.; Shanmugam, M.; Gunderson, W. A.; Pearl, N. M.; Hoffman, B. M.; Waskell, L., Role of the Proximal Cysteine Hydrogen Bonding Interaction in Cytochrome P450 2B4 Studied by Cryoreduction, Electron Paramagnetic Resonance, and Electron-Nuclear Double Resonance Spectroscopy. *Biochemistry* **2016,** *55* (6), 869-83.
20. Sheng, X.; Zhang, H.; Im, S. C.; Horner, J. H.; Waskell, L.; Hollenberg, P. F.; Newcomb, M., Kinetics of oxidation of benzphetamine by compounds I of cytochrome P450 2B4 and its mutants. *J Am Chem Soc* **2009,** *131* (8), 2971-6.
21. Ost, T. W.; Miles, C. S.; Munro, A. W.; Murdoch, J.; Reid, G. A.; Chapman, S. K., Phenylalanine 393 exerts thermodynamic control over the heme of flavocytochrome P450 BM3. *Biochemistry* **2001,** *40* (45), 13421-9.
22. Olea, C., Jr.; Kuriyan, J.; Marletta, M. A., Modulating heme redox potential through protein-induced porphyrin distortion. *J Am Chem Soc* **2010,** *132* (37), 12794-5.

23. Tosha, T.; Yoshioka, S.; Hori, H.; Takahashi, S.; Ishimori, K.; Morishima, I., Molecular mechanism of the electron transfer reaction in cytochrome P450(cam)--putidaredoxin: roles of glutamine 360 at the heme proximal site. *Biochemistry* **2002,** *41* (47), 13883-93.
24. Yoshioka, S.; Tosha, T.; Takahashi, S.; Ishimori, K.; Hori, H.; Morishima, I., Roles of the proximal hydrogen bonding network in cytochrome P450cam-catalyzed oxygenation. *J Am Chem Soc* **2002,** *124* (49), 14571-9.
25. Mak, P. J.; Yang, Y.; Im, S.; Waskell, L. A.; Kincaid, J. R., Experimental documentation of the structural consequences of hydrogen-bonding interactions to the proximal cysteine of a cytochrome P450. *Angew Chem Int Ed Engl* **2012,** *51* (41), 10403-7.
26. Zeng, H.; Tan, H.; Li, J., Cloning and function of sanQ: a gene involved in nikkomycin biosynthesis of Streptomyces ansochromogenes. *Curr Microbiol* **2002,** *45* (3), 175-9.
27. Wang, X.; Tabudravu, J.; Rateb, M. E.; Annand, K. J.; Qin, Z.; Jaspars, M.; Deng, Z.; Yu, Y.; Deng, H., Identification and characterization of the actinomycin G gene cluster in Streptomyces iakyrus. *Mol Biosyst* **2013,** *9* (6), 1286-9.
28. Koketsu, K.; Oguri, H.; Watanabe, K.; Oikawa, H., Identification and stereochemical assignment of the beta-hydroxytryptophan intermediate in the echinomycin biosynthetic pathway. *Org Lett* **2006,** *8* (21), 4719-22.
29. Praseuth, A. P.; Wang, C. C.; Watanabe, K.; Hotta, K.; Oguri, H.; Oikawa, H., Complete sequence of biosynthetic gene cluster responsible for producing triostin A and evaluation of quinomycin-type antibiotics from Streptomyces triostinicus. *Biotechnol Prog* **2008,** *24* (6), 1226-31.

30. Hirose, Y.; Watanabe, K.; Minami, A.; Nakamura, T.; Oguri, H.; Oikawa, H., Involvement of common intermediate 3-hydroxy-L-kynurenine in chromophore biosynthesis of quinomycin family antibiotics. *J Antibiot (Tokyo)* **2011,** *64* (1), 117-22.
31. Zhang, C.; Kong, L.; Liu, Q.; Lei, X.; Zhu, T.; Yin, J.; Lin, B.; Deng, Z.; You, D., In vitro characterization of echinomycin biosynthesis: formation and hydroxylation of L-tryptophanyl-S-enzyme and oxidation of (2S,3S) beta-hydroxytryptophan. *PLoS One* **2013,** *8* (2), e56772.
32. Muliandi, A.; Katsuyama, Y.; Sone, K.; Izumikawa, M.; Moriya, T.; Hashimoto, J.; Kozone, I.; Takagi, M.; Shin-ya, K.; Ohnishi, Y., Biosynthesis of the 4-methyloxazoline-containing nonribosomal peptides, JBIR-34 and -35, in Streptomyces sp. Sp080513GE-23. *Chem Biol* **2014,** *21* (8), 923-34.
33. Chen, H.; Walsh, C. T., Coumarin formation in novobiocin biosynthesis: beta-hydroxylation of the aminoacyl enzyme tyrosyl-S-NovH by a cytochrome P450 NovI. *Chem Biol* **2001,** *8* (4), 301-12.
34. Pojer, F.; Li, S. M.; Heide, L., Molecular cloning and sequence analysis of the clorobiocin biosynthetic gene cluster: new insights into the biosynthesis of aminocoumarin antibiotics. *Microbiology* **2002,** *148* (Pt 12), 3901-11.
35. Galm, U.; Schimana, J.; Fiedler, H. P.; Schmidt, J.; Li, S. M.; Heide, L., Cloning and analysis of the simocyclinone biosynthetic gene cluster of Streptomyces antibioticus Tu 6040. *Arch Microbiol* **2002,** *178* (2), 102-14.
36. Wang, Z. X.; Li, S. M.; Heide, L., Identification of the coumermycin A(1) biosynthetic gene cluster of Streptomyces rishiriensis DSM 40489. *Antimicrob Agents Chemother* **2000,** *44* (11), 3040-8.

37. Cryle, M. J.; Meinhart, A.; Schlichting, I., Structural characterization of OxyD, a cytochrome P450 involved in beta-hydroxytyrosine formation in vancomycin biosynthesis. *J Biol Chem* **2010,** *285* (32), 24562-24574.
38. Uhlmann, S.; Sussmuth, R. D.; Cryle, M. J., Cytochrome p450sky interacts directly with the nonribosomal peptide synthetase to generate three amino acid precursors in skyllamycin biosynthesis. *ACS Chem Biol* **2013,** *8* (11), 2586-2596.
39. Haslinger, K.; Brieke, C.; Uhlmann, S.; Sieverling, L.; Sussmuth, R. D.; Cryle, M. J., The structure of a transient complex of a nonribosomal peptide synthetase and a cytochrome P450 monooxygenase. *Angew Chem Int Ed Engl* **2014,** *53* (32), 8518-8522.
40. Galm, U.; Wendt-Pienkowski, E.; Wang, L.; George, N. P.; Oh, T. J.; Yi, F.; Tao, M.; Coughlin, J. M.; Shen, B., The biosynthetic gene cluster of zorbamycin, a member of the bleomycin family of antitumor antibiotics, from Streptomyces flavoviridis ATCC 21892. *Mol Biosyst* **2009,** *5* (1), 77-90.
41. McGlinchey, R. P.; Nett, M.; Eustaquio, A. S.; Asolkar, R. N.; Fenical, W.; Moore, B. S., Engineered biosynthesis of antiprotealide and other unnatural salinosporamide proteasome inhibitors. *J Am Chem Soc* **2008,** *130* (25), 7822-3.
42. Cryle, M. J.; Schlichting, I., Structural insights from a P450 Carrier Protein complex reveal how specificity is achieved in the P450(BioI) ACP complex. *Proc Natl Acad Sci U S A* **2008,** *105* (41), 15696-701.

43. Laureti, L.; Song, L.; Huang, S.; Corre, C.; Leblond, P.; Challis, G. L.; Aigle, B., Identification of a bioactive 51-membered macrolide complex by activation of a silent polyketide synthase in Streptomyces ambofaciens. *Proc Natl Acad Sci U S A* **2011,** *108* (15), 6258-63.
44. Song, L.; Laureti, L.; Corre, C.; Leblond, P.; Aigle, B.; Challis, G. L., Cytochrome P450-mediated hydroxylation is required for polyketide macrolactonization in stambomycin biosynthesis. *J Antibiot (Tokyo)* **2014,** *67* (1), 71-6.
45. Frank, B.; Wenzel, S. C.; Bode, H. B.; Scharfe, M.; Blocker, H.; Muller, R., From genetic diversity to metabolic unity: studies on the biosynthesis of aurafurones and aurafuron-like structures in myxobacteria and streptomycetes. *J Mol Biol* **2007,** *374* (1), 24-38.
46. McCoy, J. G.; Johnson, H. D.; Singh, S.; Bingman, C. A.; Lei, I. K.; Thorson, J. S.; Phillips, G. N., Jr., Structural characterization of CalO2: a putative orsellinic acid P450 oxidase in the calicheamicin biosynthetic pathway. *Proteins* **2009,** *74* (1), 50-60.
47. Guex, N.; Peitsch, M. C.; Schwede, T., Automated comparative protein structure modeling with SWISS-MODEL and Swiss-PdbViewer: a historical perspective. *Electrophoresis* **2009,** *30 Suppl 1*, S162-73.
48. Bienert, S.; Waterhouse, A.; de Beer, T. A.; Tauriello, G.; Studer, G.; Bordoli, L.; Schwede, T., The SWISS-MODEL Repository-new features and functionality. *Nucleic Acids Res* **2017,** *45* (D1), D313-D319.

49. Waterhouse, A.; Bertoni, M.; Bienert, S.; Studer, G.; Tauriello, G.; Gumienny, R.; Heer, F. T.; de Beer, T. A. P.; Rempfer, C.; Bordoli, L.; Lepore, R.; Schwede, T., SWISS-MODEL: homology modelling of protein structures and complexes. *Nucleic Acids Res* **2018,** *46* (W1), W296-W303.
50. Haslinger, K.; Brieke, C.; Uhlmann, S.; Sieverling, L.; Sussmuth, R. D.; Cryle, M. J., The structure of a transient complex of a nonribosomal peptide synthetase and a cytochrome P450 monooxygenase. *Angew Chem Int Ed Engl* **2014,** *53* (32), 8518-22.
51. Dawson, J. H.; Andersson, L. A.; Sono, M., Spectroscopic investigations of ferric cytochrome P-450-CAM ligand complexes. Identification of the ligand trans to cysteinate in the native enzyme. *J Biol Chem* **1982,** *257* (7), 3606-17.
52. Bui, S. H.; McLean, K. J.; Cheesman, M. R.; Bradley, J. M.; Rigby, S. E.; Levy, C. W.; Leys, D.; Munro, A. W., Unusual spectroscopic and ligand binding properties of the cytochrome P450-flavodoxin fusion enzyme XplA. *J Biol Chem* **2012,** *287* (23), 19699-714.
53. Sono, M.; Dawson, J. H., Formation of low spin complexes of ferric cytochrome P-450-CAM with anionic ligands. Spin state and ligand affinity comparison to myoglobin. *J Biol Chem* **1982,** *257* (10), 5496-502.
54. Fielding, A. J.; Dornevil, K.; Ma, L.; Davis, I.; Liu, A., Probing Ligand Exchange in the P450 Enzyme CYP121 from Mycobacterium tuberculosis: Dynamic Equilibrium of the Distal Heme Ligand as a Function of pH and Temperature. *J Am Chem Soc* **2017,** *139* (48), 17484-17499.
55. Denisov, I. G.; Grinkova, Y. V.; McLean, M. A.; Sligar, S. G., The one-electron autoxidation of human cytochrome P450 3A4. *J Biol Chem* **2007,** *282* (37), 26865-73.

56. Palmer, G., Electron Paramagnetic Reasonance of Hemoproteins. In *Iron Porphyrins, Part 2,* Lever, A. B. P.; Gray, H. B., Eds. Addison-Wesley: Reading, MA, 1983; pp 55-64.

57. Lipscomb, J. D., Electron paramagnetic resonance detectable states of cytochrome P-450cam. *Biochemistry* **1980,** *19* (15), 3590-9.

58. Bohan, T. L., Analysis of low-spin ESR spectra of ferric-heme proteins: A reexamination. *J Magn Reson* **1977,** *26* (1), 109-118.

59. Peisach, J., EPR of Metalloproteins; Truth Tables Revisited. In *Foundations of Modern EPR*, Eaton, G. R.; Eaton, S. S.; Salikhov, K. M., Eds. World Scientific Publishing Company: Singapore, 1998; pp 346-360.

60. Dawson, J. H.; Andersson, L. A.; Sono, M., Spectroscopic investigations of ferric cytochrome P-450-CAM ligand complexes. Identification of the ligand trans to cysteinate in the native enzyme. *J Biol Chem* **1982,** *257* (7), 3606-17.

61. Lockart, M. M.; Rodriguez, C. A.; Atkins, W. M.; Bowman, M. K., CW EPR parameters reveal cytochrome P450 ligand binding modes. *J Inorg Biochem* **2018,** *183*, 157-164.

62. Dawson, J. H.; Andersson, L. A.; Sono, M., The diverse spectroscopic properties of ferrous cytochrome P-450-CAM ligand complexes. *J Biol Chem* **1983,** *258* (22), 13637-45.

63. Lelyveld, V. S.; Brustad, E.; Arnold, F. H.; Jasanoff, A., Metal-substituted protein MRI contrast agents engineered for enhanced relaxivity and ligand sensitivity. *J Am Chem Soc* **2011,** *133* (4), 649-51.

64. Liu, H.; Naismith, J. H., An efficient one-step site-directed deletion, insertion, single and multiple-site plasmid mutagenesis protocol. *BMC Biotechnol.* **2008,** *8,* 91.

65. Varnado, C. L.; Goodwin, D. C., System for the expression of recombinant hemoproteins in Escherichia coli. *Protein Expr. Purif.* **2004,** *35* (1), 76-83.

APPENDIX A

Copyright Clearance Permissions for Chapters 2 and 3

Title: Dioxygen Activation by the Biofuel-Generating Cytochrome P450 OleT
Author: Courtney E. Wise, Chun H. Hsieh, Nathan L. Poplin, et al
Publication: ACS Catalysis
Publisher: American Chemical Society
Date: October 1, 2018

PERMISSION/LICENSE IS GRANTED FOR YOUR ORDER AT NO CHARGE

This type of permission/license, instead of the standard Terms & Conditions, is sent to you because no fee is being charged for your order. Please note the following:

- Permission is granted for your request in both print and electronic formats, and translations.
- If figures and/or tables were requested, they may be adapted or used in part.
- Please print this page for your records and send a copy of it to your publisher/graduate school.
- Appropriate credit for the requested material should be given as follows:
  "Reprinted (adapted) with permission from (COMPLETE REFERENCE CITATION). Copyright (YEAR) American Chemical Society."
  Insert appropriate information in place of the capitalized words.
- One-time permission is granted only for the use specified in your request. No additional uses are granted (such as derivative works or other editions). For any other uses, please submit a new request.
-